Spring 2023

Low Current Electrospray Ionization Mass Spectrometry for Environmental Contaminants and Proteins

Taoqing Wang
University of New Hampshire, Durham

Low Current Electrospray Ionization Mass Spectrometry for Environmental Contaminants and Proteins

By

Taoqing Wang

A DISSERTATION

Submitted to the University of New Hampshire

In Partial Fullfillment of the Requirements for the Degree of

Doctor of Philosophy

Department of Chemistry

Durham, New Hampshire

May 2023

The dissertation has been examined and approved in partial fulfillment of the requirements for the degree of Ph.D. in Chemistry by:

Dissertation Direction, Dr. Anyin Li

Professor of Chemistry, University of New Hampshire

Dr. W. Rudolf Seitz

Professor of Chemistry, University of New Hampshire

Dr. Glen Miller

Professor of Chemistry, University of New Hampshire

Dr. Christopher Bauer

Professor of Chemistry, University of New Hampshire

Dr. Nivedita Gupta

Professor of Chemical Engineering, University of New Hampshire

May, 2023

Dedicated to my husband and my son.

ACKNOWLEDGEMENTS

I would like to express my deepest gratitude to my husband Yujian Wu and my son Ethan Wu, for their unwavering support throughout my PhD journey. Drawing courage from them, I was able to overcome the obstacles. I am grateful to my parents, Aiping Zhang and Anmin Wang, my older brother TaoTao Wang, my mother-in-law JianHua Ma, my father-in-law Weihua Wu, for all the support they provided.

I am indebted to my research advisor, Anyin Li, for his consistent effort in making me a better analytical scientist. His advice and guidance during my academic pursuits have been instrumental in my success. I also extend my sincere thanks to professors Rudi Seitz, Sterling Tomellini, and other professors for their dedication to imparting knowledge and shaping me into a well-rounded scholar.

Special thanks to Prof. Sterling Tomellini for his help with electronics fabrication and water samples provided for the PFOS project, and to Dr. Ran Qiu for his assistance with electrooxidation of dihydroethidium. I am also grateful to Dr. Mengtian Li for her support in the developing piezoelectric inkjet printer device. I would like to thank Xing Xu, Shan Chen, Huishan Li, Nick Allen, Ian Ferraro, and others who worked with me on several projects.

Lastly, I would also like to express my deep gratitude to Chemistry Dept. manager Cindi Rohwer and Chair Dr. Erik Berda, and graduate coordinator Dr. Margaret Greenslade, who have always been there to help me through every stage of my PhD program. I am also grateful to my committee members Dr. Glen Miller, Dr. Christopher Bauer, and Dr. Nivedita Gupta for their insightful feedback and guidance they have provided throughout this process.

ABSTRACT

The introduction of electrospray ionization (ESI) in the 1980s has had a significant impact on the field of liquid chromatography-mass spectrometry (LC-MS), enabling the qualitative and quantitative analysis of small molecules in complex biological and environmental samples. NanoESI, developed in 1993, further improved sensitivity and reduced sample consumption. However, the detection limits for some environmental contaminants, such as perfluorooctanoate sulfonate (PFOS), require ppt-level detection, which necessitates preconcentration. Solid-phase microextraction (SPME) is a commonly used technique, and liquid-liquid extraction has shown promising results for water samples. Recently, the Li group has discovered femtoampere and picoampere ionization modes of ESI, which have shown practical benefits such as improved microsample utilization and reduced contamination.

In the first part, the ESI characteristics of a non-polar solvent were investigated using femtoampere and picoampere modes. Direct ESI-MS was used to rapidly analyze perfluorinated sulfonic acid (PFS) analytes in drinking water samples. By using femtoampere and picoampere modes in ESI, detection limits of 0.38-5.1 ppt and a quantitation range of 5-400 ppt were achieved for perfluorinated sulfonic compounds in drinking water samples.

The second part of the study focused on the charge state distribution of model protein ions in femtoampere ESI under different pH conditions. The study found that signal intensities of proteins were 4 orders of magnitude lower in femtoampere mode than the nanoampere mode, and the average charge state was about 1-2 charge states lower. The addition of 0.1% formic acid into the solution in femtoampere mode increased the average charge state of proteins to the same level as that in nanoampere mode. The study proposed that the less acidic environment protein

experienced in femtoampere mode may be attributed to fewer fission events compared to nanoampere mode.

TABLE OF CONTENTS

LIST OF TABLES

LIST OF FIGURES

LIST OF SCHEMES

LIST OF ABBREVIATIONS, UNITS, AND SYMBOLS

AC	alternating current
ACN	acetonitrile
ACS	average charge state
AGC	automatic gain control
˚C	degree Celsius
CE	capillary electrophoresis
CEM	chain ejection model
CID	collision-induced dissociation
CRM	charge residue model
Da	atomic mass unit
DC	direct current
DCF	dichlorofluorescein
DHE	dihydroethidium
E^+	ethidium cation
EIC	extracted ion chronogram
ESA	ethane-1,2-disulfonic acid
ESI	electrospray ionization
fA	Femto-ampere
FA	Formic acid
GND	ground (in an electric circuit)
HEPES	4-(2-hydroxyethyl-)-1-piperazineethanesulfonic acid
HPLC	high performance liquid chromatography
HSA	1-heptanesulfonic acid sodium
I.D.	inner diameter

IEM	ion evaporation model
ILD	instrumental detection limits
IS	internal standard
ITO	Indium-Tin-Oxide
I-V	current-voltage
LC	liquid chromatography
LODs	Limits of detection
Met	methionine
MeOH	methanol
$[M+H]^+$	singly charged protonated analyte
$[M+2H]^{2+}$	Doubly charged protonated analyte
MS	mass spectrometry
MS/MS	tandem mass spectrometry
nA	Nano-ampere
nanoESI	Nano electrospray ionization
nF	Nano-Farad
NHE	normal hydrogen electrode
nL	Nano-Liter
O.D.	Outer diameter
pA	Pico-ampere
PFDS	perfluoro-1-decane sulfonic acid
PFDoS	perfluoro-1-nonane sulfonic acid
PFHpS	perfluoro-1-hepane sulfonic acid
PFHxS	Perfluoro-1-hexane sulfonic acid
PFNS	perfluoro-1-nonane sulfonic acid
PFOA	perfluorooctanoic acid
PFOS	perfluorooctane sulfonate

PFS	perfluorinated sulfonic acid
RF	Radio frequency
ROS	reactive oxygen species
RSD	relative standard deviation
SCE	saturated calomel electrode
SNR	signal to noise ratio
SPME	solid phase microextraction
Th	Mass-to-charge ratio unit
TIC	total ion current
2D	two-dimensional
2-OH-E^+	2-hydroxyethidium cation

1 Introduction

Electrospray ionization (ESI) is a soft ionization technique that enables the ionization of both non-volatile small molecules and large biomolecules. As noted by John Fenn, the Nobel Prize Winner in 2002, this technique gives wings to elephant molecules.[1] Its compatibility with liquid chromatography (LC) and capillary electrophoresis (CE) separation[2] make it a widely used technique coupled with mass spectrometry for protein research.[3] The Ambient ESI developed by R. Graham Cooks group at Purdue University in 2004, allows for direct analysis[4] in the field of clinical and forensics[5] with minimal sample preparation required.

1.1 Electrospray ionization

Electrospray ionization (ESI) is a technique that involves the use of a capillary emitter, typically composed of fused silica or stainless steel, to contain an analyte dissolved in polar solvents such as water-methanol, methanol, acetonitrile, and acetonitrile-water. The concentration is between 10^{-7}~10^{-3} mol/L. The flow rate is typically maintained between 1-100 μL/min. The capillary emitter, with an outer diameter of about 0.2 mm, is placed 1-3 cm away from the mass inlet, and a high voltage of 2-6 kV is applied. The high electric field (~10^6 volts per meter [a]) at the emitter tip induces the polarization of the solvent and accumulation of charges near the meniscus of the liquid, resulting in the cone formation, termed as Taylor cone.[6,7] When the applied field exceeds the surface tension of the liquid,[b] a fine jet composed of highly charged droplets emerges from the cone tip. The initial droplet has a diameter of ~1.5 μm and carries 50,000 elementary charges[8]. When the droplets have charging levels between 70% or 80% of the Rayleigh limit,[c]

[a] $E=\frac{2V}{rln(4d/r)}$, where v is the applied voltage, r is the capillary outer radius, and d is the distance between emitter and MS inlet.

[b] Therefore, the onset voltage is dependent on the surface tension of solvent.

[c] $q^2 = 8\pi^2\varepsilon\gamma D^3$, where q is charge, ε is permittivity of environment, γ is surface tension, and D is diameter of droplet.

repulsive force overcomes the surface tension, leading to production of smaller droplets, which is termed Coulomb fission.[9] After each fission event, the initial droplet loses ~20% charges and 2% mass. Then the droplet continues to shrink by solvent evaporation until the surface charge density increases approaching the Rayleigh limit and undergoes another fission event. To explain the formation of gas phase ions from the charged droplets, Iribarne and Thomson proposed the Ion Evaporation Model (IEM) that the electric field at the droplet surface provides the work required to lift the analyte ion from the droplet surface, by overcoming the charged species' adhesion force to the surface.[10] On the basis of the IEM model, the signal intensities of analytes are found to depend on factors such as the solvation energy of analytes, [11,12] pKa[13], hydrophobicity,[14] and solvent compositions.[14]

Alternatively, Dole proposed the Charge Residue Model (CRM)[15] that assumes the charged droplet contain a single analyte ion which is released when the solvent evaporates. The model is widely accepted for the large globular species in the gas phase. For the unfolded proteins, the CEM (chain ejection model)[16] is proposed that the unfolded protein migrates to the droplet surface and bind the excess charge, similar to IEM.

The pumping out of the positive charges (when the voltage is positive) must be accompanied by the introduction of an equivalent number of negative charges in the circuit. This process occurs via electrooxidation of species, including the analyte, solvent, and electrode, [17] with oxidation potential far below 1 V (vs. saturated calomel electrode SCE), [18-19] thus rendering ESI a current-driven electrochemical half-cell.[20-22] As the ESI pioneer, John Fenn also noted that "electrochemical reactions might be taking place in an ES source… was too obvious to mention." in the discussion of mechanism of ESI.[23] The actual oxidation reactions depend on the electrical potential present at given locations of the metal-liquid interface [24-25] and on the electrochemical

oxidation potential for the given reactions. [26] The electrochemical reaction in ESI has also been leveraged to ionize less polar analytes that are challenging to protonate or deprotonate, [21, 27] enabling absolute quantitative analysis.[28]

The electrochemical processes have not significantly impacted the majority of ESI mass spectrometry (MS) analyses, although a few peptides, such as hemoglobin oxidation, methionine oxidation in the peptide Aβ, have been observed in a typical electrospray ionization (ESI) setup (with a spray voltage of +2 kV and flow rate of 10 µL/min) [29-30] To mitigate the electrochemical oxidation of proteins, an alternating current (AC) high voltage-induced ESI [31-33] and sacrificing redox buffer coated on electrode [34] have been shown to be effective

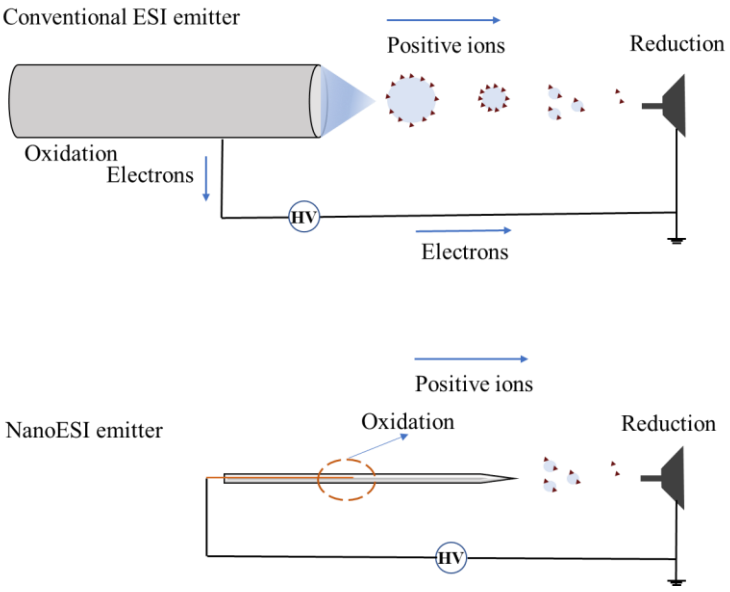

Scheme 1-1. Comparison of the conventional ESI and nanoESI schemes. In Conventional ESI, a sheath gas (e.g., dry nitrogen) flows around a capillary (outer diameter 0.1 mm) to improve nebulization and guide the spray plume into the mass spectrometer. The flow rate is typically maintained at 1-10 µL/min. In positive ion mode, oxidation occurs at the electrode/solvent interface. Products occur in both positive and negative ion modes. NanoESI, on the other hand, does not use a sheath gas or pump, and instead employs an emitter tip with a diameter of 1-3 µm. The flow rate is typically around 20 nL/min. [35]

In the interest of using a small volume of analyte, Wilm and Mann developed nanoESI, [35] [36] which utilizes an emitter with a micrometer-sized tip (1~3μm) and operates without external pumping. The flow rate in nanoESI is enforced by the electrostatic force and is typically measured at ~20 nL/min. As a result, the charge-to-volume ratio in nanoESI is higher than in conventional ESI, with a lower spray current of 250 nanoampere compared to 1 μA, and a lower flow rate of 20 nL/min compared to 10 μL/min. In the context of nanoESI application, it has been observed that this technique offers superior ionization efficiency compared to conventional ESI. Additionally, it has been found that ion suppression is practically absent when the flow rate is below 20 nL/min. [37] It should be noted that ion suppression is a practical concern in conventional ESI-MS analysis. [38]

The small initial droplets (~200 nm vs. 1.5 μm in conventional ESI) generated in the nanoESI not only account for the ionization efficiency improvement, but the electrooxidation behaviors also changed. The nanoESI setup has been modified for a soft-landing technique, which refers to deposit ions with low kinetic energy (<100 eV) on the desired surfaces, to generate nanoparticles through the oxidation of electrode (e.g., Ag and Cu) [39] and screen photoreactions. [40] Meanwhile, to avoid the electrochemical reaction in the nanoESI, the relay electrospray ionization technique is used,[41] in which the electrically floated sample solution is charged by depositing primary ions. This completely avoids electrochemical reactions in the sample solution.[42]

1.2 Research Objectives

Most mass spectrometers are capable of detecting femtoampere-level signals, with a detector noise of less than 4 counts/sec. This translates to a concentration as low as 10^{-8} M at a flow rate of 1 μL/min. Assuming complete ionization of the analyte and an ion transmission efficiency of approximately 0.001%, it is estimated that only one charge is detected for every 100,000 charges

leaving the emitter tip, without accounting for ionization efficiency. In contrast, the ion current generated by nanoESI is around 100 nA, which is above the minimum detector current required for femtoampere-level detection in modern mass spectrometer. Investigating low current ESI from picoampere to femtoampere is the focus of my research, with the aim of extending the application of ESI in various fields.

Chapter two focuses on the development of a cost-effective device that uses a piezoelectric inkjet printing to generate pico-liter droplets. The device can produce droplets with a volume of 9.5 ± 2 pL with an ejection rate of 2 m/s, making it suitable for applications requiring the precise delivery of small amounts of solvents into an ESI setup, such as nanoESI emitter and paper spray. This method is easy-to-construct and is ideal for many chemical and biological research applications.

Chapter three evaluates a novel scan function developed by Thermo Scientific in a hybrid LTQ mass spectrometer to improve the precision of quantitative analyses. The results showed that the precision was significantly enhanced in both the continuous ion source and the pulsed ion source. The study highlights the importance of utilizing isotopically labeled internal standards and the potential benefits of the novel scan function in improving quantitative analysis using mass spectrometry.

Chapter four describes the development of a novel preconcentration strategy for ambient electrospray ionization mass spectrometry (ESI-MS) analysis. While ESI-MS has gained significant attention for its ability to ionize samples in the open air with minimal sample preparation, it faces challenges in analyzing complex biological samples and trace analytes at ppt levels. To address this issue, this study introduces a new approach using a filamented glass capillary, commonly used as capillary emitter in nanoESI analysis, while here as a nanoliter

sampling device for preconcentration treatment. The annealed subchannels facilitate fluid flow via capillary action and accumulation at the tapered region, enabling the construction of a preconcentration setup. The approach offers a disposable, simple, and low-cost platform as a generic enrichment method that can reduce sample size and avoid clogging issues. The effectiveness of the method was confirmed using both direct optical visualization and ESI-MS analysis.

Chapter five investigates the oxidation behavior of DHE, a commonly used fluorescence probe for detecting superoxide in biological systems, during electrospray and provides guidance for analyzing DHE using ESI-based mass spectrometry methods. NanoESI-MS was used to screen DHE oxidation products when the total analyze time was less than 0.2 min, while tandem mass analysis was used to provide insights into modification sites on DHE, However, detailed structural information was limited due to the stability of the conjugated π system of DHE.

Chapter six investigated the electrospray ionization (ESI) characteristics of a non-polar solvent in both femtoampere and picoampere modes. Chloroform extraction solutions were analyzed using direct ESI-MS, allowing for rapid analysis of perfluorinated sulfonic acid (PFS) in drinking water. Ionization currents were measured with femtoampere sensitivity by ramping the spray voltage from 0 to -5000 V using micrometer emitter tips. The effects of spray voltage and inlet temperature were also studied. Methanol was used to compare the characteristics of spraying chloroform. The ionization onset of the chloroform solution was found to be 41 ± 17 fA at 300 V, and the ionization current gradually increased with voltage, remaining below 100 pA even at -5000 V. The detection limit for PFOS was improved to 25 ppt in chloroform. A liquid-liquid extraction workflow was developed to analyze perfluorinated sulfonic compounds in 1 mL drinking water samples using an ion trap mass spectrometer. By using the femtoampere and

picoampere modes in ESI, detection limits of 0.38-5.1 ppt and a quantitation range of 5-400 ppt were achieved for perfluorinated sulfonic compounds in drinking water samples. The study demonstrates that femtoampere and picoampere modes expand the solvent compatibility range of electrospray ionization, enabling quantitative analysis in ppt concentrations.

Chapter seven discussed the charge state distributions of model protein ions in femtoampere electrospray mode under different pH solutions. It was found that the signal intensities of proteins were 4 orders of magnitude lower in femtoampere mode compared to nanoampere mode, and the average charge state was about 1-2 charge states less. The addition of 0.1% formic acid into solution in femtoampere mode increased charge state distributions of proteins to the same pattern as that in nanoampere mode. The perception of more acidic environment by proteins in nanoampere mode could be explained with the charge residue model (CRM), which predicted fewer fission events in femtoampere mode.

1.3 References

1. Fenn, J. B., Electrospray Wings for Molecular Elephants (Nobel Lecture). *Angewandte Chemie International Edition* **2003,** *42* (33), 3871-3894.

2. Smith, R. D.; Loo, J. A.; Edmonds, C. G.; Barinaga, C. J.; Udseth, H. R., New developments in biochemical mass spectrometry: electrospray ionization. *Analytical Chemistry* **1990,** *62* (9), 882-899.

3. Domon, B.; Aebersold, R., Mass Spectrometry and Protein Analysis. *Science* **2006,** *312* (5771), 212-217.

4. Haddad, R.; Sparrapan, R.; Kotiaho, T.; Eberlin, M. N., Easy Ambient Sonic-Spray Ionization-Membrane Interface Mass Spectrometry for Direct Analysis of Solution Constituents. *Analytical Chemistry* **2008,** *80* (3), 898-903.

5. Green, F. M.; Salter, T. L.; Stokes, P.; Gilmore, I. S.; O'Connor, G., Ambient mass spectrometry: advances and applications in forensics. *Surface and Interface Analysis* **2010,** *42* (5), 347-357.

6. Kebarle, P.; Verkerk, U. H., Electrospray: From ions in solution to ions in the gas phase, what we know now. *Mass Spectrometry Reviews* **2009,** *28* (6), 898-917.

7. Banerjee, S.; Mazumdar, S., Electrospray ionization mass spectrometry: a technique to access the information beyond the molecular weight of the analyte. *International journal of analytical chemistry* **2012,** *2012*, 282574.

8. De Hoffmann, E.; Stroobant, V., *Mass spectrometry: principles and applications*. John Wiley & Sons: 2007.

9. Gomez, A.; Tang, K., Charge and fission of droplets in electrostatic sprays. *Physics of Fluids* **1994,** *6* (1), 404-414.

10. Iribarne, J. V., On the evaporation of small ions from charged droplets. *The Journal of Chemical Physics* **1976,** *64* (6), 2287.

11. Fenn, J. B., Ion formation from charged droplets: Roles of geometry, energy, and time. *Journal of the American Society for Mass Spectrometry* **1993,** *4* (7), 524-535.

12. Null, A. P.; Nepomuceno, A. I.; Muddiman, D. C., Implications of Hydrophobicity and Free Energy of Solvation for Characterization of Nucleic Acids by Electrospray Ionization Mass Spectrometry. *Analytical Chemistry* **2003,** *75* (6), 1331-1339.

13. Liigand, P.; Kaupmees, K.; Haav, K.; Liigand, J.; Leito, I.; Girod, M.; Antoine, R.; Kruve, A., Think Negative: Finding the Best Electrospray Ionization/MS Mode for Your Analyte. *Analytical Chemistry* **2017,** *89* (11), 5665-5668.

14. Kageyama Kaneshima, A.; Motoyama, A.; Takayama, M., Influence of Solvent Composition and Surface Tension on the Signal Intensity of Amino Acids in Electrospray Ionization Mass Spectrometry. *Mass spectrometry (Tokyo, Japan)* **2019,** *8* (1), A0077.

15. Dole, M.; Mack, L. L.; Hines, R. L.; Mobley, R. C.; Ferguson, L. D.; Alice, M. B., Molecular Beams of Macroions. *The Journal of Chemical Physics* **1968,** *49* (5), 2240-2249.

16. Konermann, L.; Rodriguez, A. D.; Liu, J., On the Formation of Highly Charged Gaseous Ions from Unfolded Proteins by Electrospray Ionization. *Analytical Chemistry* **2012,** *84* (15), 6798-6804.

17. Blades, A. T.; Ikonomou, M. G.; Kebarle, P., Mechanism of electrospray mass spectrometry. Electrospray as an electrolysis cell. *Analytical Chemistry* **1991,** *63* (19), 2109-2114.

18. Van Berkel, G. J.; Zhou, F., Characterization of an electrospray ion source as a controlled-current electrolytic cell. *Analytical Chemistry* **1995,** *67* (17), 2916-2923.

19. Van Berkel, G. J.; Zhou, F., Electrospray as a Controlled-Current Electrolytic Cell: Electrochemical Ionization of Neutral Analytes for Detection by Electrospray Mass Spectrometry. *Analytical Chemistry* **1995,** *67* (21), 3958-3964.

20. Blades, A. T.; Ikonomou, M. G.; Kebarle, P., Mechanism of Electrospray Mass-Spectrometry - Electrospray as an Electrolysis Cell. *Anal. Chem.* **1991,** *63* (19), 2109-2114.

21. Van Berkel, G. J.; McLuckey, S. A.; Glish, G. L., Electrospray ionization of porphyrins using a quadrupole ion trap for mass analysis. *Analytical Chemistry* **1991,** *63* (11), 1098-1109.

22. Van Berkel, G. J.; Asano, K. G.; Schnier, P. D., Electrochemical processes in a wire-in-a-capillary bulk-loaded, nano-electrospray emitter. *J. Am. Soc. Mass. Spectrom.* **2001,** *12* (7), 853-862.

23. Mora, J. F. d. l.; Van Berkel, G. J.; Enke, C. G.; Cole, R. B.; Martinez-Sanchez, M.; Fenn, J. B., Electrochemical processes in electrospray ionization mass spectrometry. *Journal of Mass Spectrometry* **2000,** *35* (8), 939-952.

24. Li, Y.; Pozniak, B. P.; Cole, R. B., Mapping of Potential Gradients within the Electrospray Emitter. *Anal. Chem.* **2003,** *75* (24), 6987-6994.

25. Pozniak, B. P.; Cole, R. B., Current measurements within the electrospray emitter. *J. Am. Soc. Mass. Spectrom.* **2007,** *18* (4), 737-748.

26. Van Berkel, G. J.; Kertesz, V., Using the electrochemistry of the electrospray ion source. *Analytical chemistry* **2007,** *79* (15).

27. Xu, X. M.; Lu, W. Z.; Cole, R. B., On-line probe for fast electrochemistry/electrospray mass spectrometry. Investigation of polycyclic aromatic hydrocarbons. *Anal. Chem.* **1996,** *68* (23), 4244-4253.

28. Ai, Y.; Zhao, P.; Fnu, P. I. J.; Chen, H., Absolute Quantitation of Tryptophan-Containing Peptides and Amyloid β-Peptide Fragments by Coulometric Mass Spectrometry. *Journal of the American Society for Mass Spectrometry* **2021,** *32* (7), 1771-1779.

29. Boys, B. L.; Kuprowski, M. C.; Noël, J. J.; Konermann, L., Protein Oxidative Modifications During Electrospray Ionization: Solution Phase Electrochemistry or Corona Discharge-Induced Radical Attack? *Analytical Chemistry* **2009,** *81* (10), 4027-4034.

30. Chen, M.; Cook, K. D., Oxidation Artifacts in the Electrospray Mass Spectrometry of Aβ Peptide. *Analytical Chemistry* **2007,** *79* (5), 2031-2036.

31. Stark, A. K.; Schilling, M.; Janasek, D.; Franzke, J., Characterization of dielectric barrier electrospray ionization for mass spectrometric detection. *Anal Bioanal Chem* **2010,** *397* (5), 1767-1772.

32. Huang, G. M.; Li, G. T.; Ducan, J.; Ouyang, Z.; Cooks, R. G., Synchronized Inductive Desorption Electrospray Ionization Mass Spectrometry. *Angewandte Chemie-International Edition* **2011,** *50* (11), 2503-2506.

33. Pei, J. Y.; Zhou, X.; Wang, X. Q.; Huang, G. M., Alleviation of Electrochemical Oxidation for Peptides and Proteins in Electrospray Ionization: Obtaining More Accurate Mass Spectra with Induced High Voltage. *Anal. Chem.* **2015,** *87* (5), 2727-2733.

34. Peintler-Krivan, E.; Van Berkel, G. J.; Kertesz, V., Minimizing analyte electrolysis in electrospray ionization mass spectrometry using a redox buffer coated emitter electrode. *Rapid Communications in Mass Spectrometry* **2010,** *24* (9), 1327-1334.

35. Wilm, M.; Mann, M., Analytical Properties of the Nanoelectrospray Ion Source. *Analytical Chemistry* **1996,** *68* (1), 1-8.

36. Wilm, M. S.; Mann, M., Electrospray and Taylor-Cone theory, Dole's beam of macromolecules at last? *International Journal of Mass Spectrometry and Ion Processes* **1994,** *136* (2), 167-180.

37. Schmidt, A.; Karas, M.; Dülcks, T., Effect of different solution flow rates on analyte ion signals in nano-ESI MS, or: when does ESI turn into nano-ESI? *Journal of the American Society for Mass Spectrometry* **2003,** *14* (5), 492-500.

38. Annesley, T. M., Ion Suppression in Mass Spectrometry. *Clinical Chemistry* **2003,** *49* (7), 1041-1044.

39. Li, A.; Luo, Q.; Park, S. J.; Cooks, R. G., Synthesis and catalytic reactions of nanoparticles formed by electrospray ionization of coinage metals. *Angew Chem Int Ed Engl* **2014,** *53* (12), 3147-50.

40. Chen, S.; Wan, Q.; Badu-Tawiah, A. K., Picomole-Scale Real-Time Photoreaction Screening: Discovery of the Visible-Light-Promoted Dehydrogenation of Tetrahydroquinolines under Ambient Conditions. *Angewandte Chemie (International ed. in English)* **2016,** *55* (32), 9345-9.

41. Li, A.; Hollerbach, A.; Luo, Q.; Cooks, R. G., On-Demand Ambient Ionization of Picoliter Samples Using Charge Pulses. *Angew. Chem. Int. Ed.* **2015,** *54* (23), 6893-6895.

42. Qiu, R.; Zhang, X.; Luo, H.; Shao, Y., Mass spectrometric snapshots for electrochemical reactions. *Chemical Science* **2016,** *7* (11), 6684-6688.

43. Page, J. S.; Kelly, R. T.; Tang, K.; Smith, R. D., Ionization and Transmission Efficiency in an Electrospray Ionization–Mass Spectrometry Interface. *Journal of the American Society for Mass Spectrometry* **2007,** *18* (9), 1582-1590.

2 Generate Pico-liter Droplets Using Piezoelectric Inkjet

2.1 Introduction

In recent years, there has been a growing interest in the use of acoustic droplet ejection mass spectrometry (ADE-MS) for high-throughput analysis.[1–3] This technique involves generating droplets on the surface of a liquid by applying a pulse of ultrasound.[4] This method has drawn attention from the mass spectrometric community, particularly with the launch of ADEMS developed by SCIEX in 2020. Piezoelectric inkjet is another technique that can be used to generate droplets by expelling fluid from a jet nozzle one droplet at a time, using piezoelectric material to change the nozzle shape after applying voltages at specific waveform and generate a pressure pulse, pushing a droplet of ink out of the nozzle.[5] Luo et al. was the first group to adopt inkjet printer to generate pico-liter droplets for ESI-MS analysis. [6] In addition to their coupling with mass spectrometer, both ADE and piezoelectric inkjet have the potential applications in various fields such as immunoassay at the nanoliter level [7] and chemical reactions in droplets.[2] In this study, we have used commercially available materials to build up a device that can produce pico-liter droplets.

2.2 Experimental

2.2.1 Chemicals and Materials

An inkjet printer cartridge (model DMP-2831) was purchased from FuJIFILM Dimatix (Tokyo, Japan); The material is compatible with organic solvent methanol. The dual channel arbitrary waveform function generator JDS6600 DDS was purchased from Amazon (Seattle, WA); TS250 waveform amplifier was purchased from Accel Instruments (Irvine, CA). HPLC grade water and methanol were from Sigma-Aldrich (St. Louis, MO). The RIGOL DS1054Z oscilloscope was purchased from Amazon (Seattle, WA). The KEYSIGHT U12411B handled

digital multimeter was purchased from Amazon (Seattle, WA). A green laser pointer used to observe the jetting droplet was purchased from Amazon (Seattle, WA). The analytical balance was purchased from OHAUS (Parsippany, NJ).

2.2.2 Waveform optimization

The optimization of jetting waveform for the desired ink was carried out on Dimatix Materials Printer DMP-2831 (FuJIFILM, Tokyo, Japan) equipped with a camera that can directly observe the jetting nozzles. The increment of voltage was 1 volt. The cartridge temperature was set to room temperature 25 °C. The frequency used was 1 kHz, and the meniscus was 0 inches H_2O, meaning that no pressure was applied on the nozzles. A delay time was set to 100 μs, which refers to the time needed to see the droplet after applying the pulse to the desired nozzle.

2.3 Results

2.3.1 Theory of picoliter droplet generation using piezoelectric inkjet

A typical inkjet printer uses a piezoelectric material to push out tiny droplets of ink. A pulse of voltage is applied to the material, causing a shape change that forces a droplet out of the nozzle by overcoming its surface tension. However, not all fluids can be printed using this technique. For example, pure methanol with a low viscosity of 0.58 mPa·s is unable to be held in the nozzle without dripping. The printability of fluids has been characterized by Jang et al. in terms of the inverse (Z) of the Ohnesorge number that is related to the viscosity, surface tension and density of fluid. [8] The study found that droplets can be stably pulled into and pushed out of the nozzle chamber as long as Z value falls between 4 and 14. **Equation 2-1** shows the calculation of the Z value, where α is the diameter of the printing nozzle; ρ, γ, and η are the density, surface tension, and the viscosity of fluid.

$$Z = \frac{(\alpha\rho\gamma)^{1/2}}{\eta}$$

Equation 2-1

Accordingly, we used 50% methanol/water as ink for the offline device, as it is compatible with electrospray ionization. The Z value was calculated using Equation 1 with α (the diameter of current inkjet nozzle is 21.5 μm) and other parameters (density 0.926 kg/L, viscosity 1.62 mPa·s, surface tension 27.25 dynes/cm). The result was a Z value of 14.4, which almost satisfies the requirement for printable inks.

2.3.2 Waveform optimization for 50% MeOH/Water(v/v)

The inkjet waveform for 50% methanol/water was optimized using a commercial material printer that can monitor the trajectory of droplets with a high-speed camera. The parameters of the waveform applied to the piezoelectric actuator have a profound effect on ink ejection. As seen in **Figure 2-1c**, two deflected droplets are injected simultaneously by applying waveform with a steep slew rate that bends and releases the membrane quickly. By slowing the slew rate (**Figure 2-1a**), one droplet is injected straight down upon each pulse. So, the waveform with a pulse width at 43 μs and a driving voltage at 20 volts was adopted to design the droplet generation device, which was recorded with a digital oscilloscope.

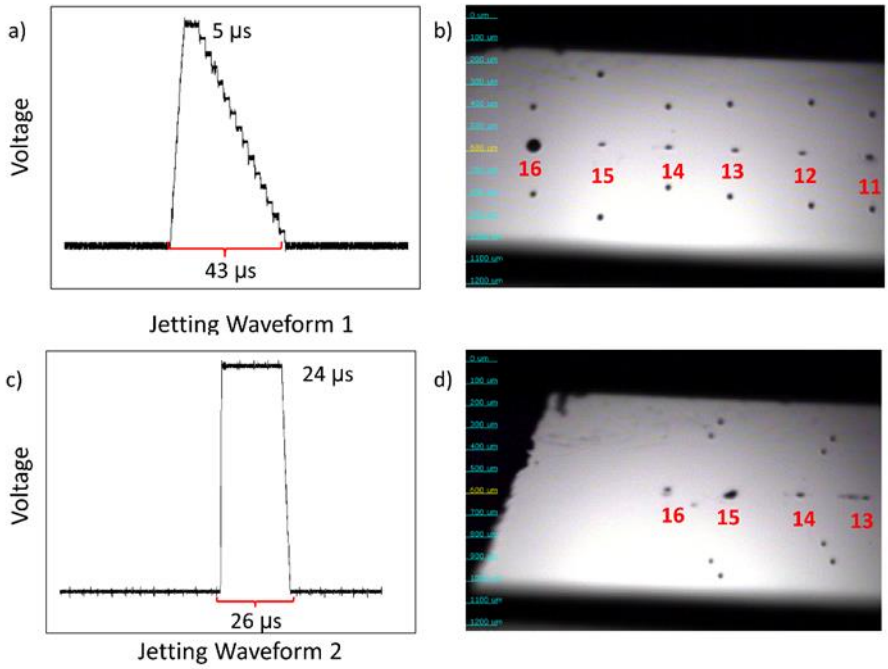

Figure 2-1. a) Jetting waveform 1 with raising time 3 µs, dwell time 5 µs and falling time 35 µs b) trajectory of single droplet in silicon nozzle 11-16 by applying waveform, in which the ejection rate of droplet is 2 m/sec 1; c) Jetting waveform 2 with raising time 1 µs, dwell time 24 µs and falling time 1 µs; d) trajectory of single droplet in silicon nozzle 13-16 by applying waveform 2, , in which the ejection rate of droplet is 2 m/sec.

2.3.3 Build a device.

To build a device, an appropriate waveform is a requisite. We used a function generator to create the desired waveform (**Table 2-1** and **Figure 2-2**). The maximum amplitude of the signal generator used in this study was only 5 volts, which is not sufficient to trigger the droplet jetting of the ink 50% methanol/water. Therefore, a waveform amplifier was connected into the circuit to give a gain of 10. In addition to the waveform, a commercial piezoelectric inkjet cartridge containing 24 pins and 16 silicon nozzles was utilized to generate pico-liter droplets **(Figure 2-3**). To figure out the right pins to use as ground (GND) in the circuit, a multimeter was used to measure the capacitance between pins. This is because the piezoelectric material, which is a class of high resistance dielectric material, has some capacitance when sandwiched by two conductive pins.

Table 2-1 The Wave function needed for one pulse.[4]

X/time (μs)	X/Dots	Y/voltage(volts)	Y/Amplitude
0	0	0	0
3	6.1	20	1
8	16.3	20	1
43	89.7	0	0
1000	2048	0	0

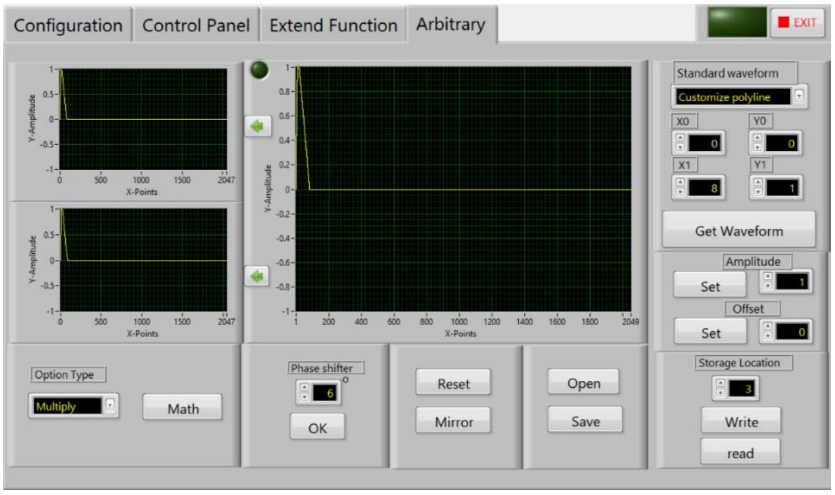

Figure 2-2. Create the waveform using JDS 6600 control panel. Firstly, connect function generator (JDS6600) to the laptop installed software JDS 6600 and configure the generator by choosing appropriate port and model. Create the waveform according to Table 2-1 and click the write icon to load the function to the generator for further use.

[4] A waveform of time against voltage is converted to a plot of dots versus amplitude. As the frequency of waveform is 1 kHz, the time interval is 1000 μs. The total number of dots is 2048 for each function in the generator used in this study.

It was found that the capacitance between pin 4 to pin 5 was 0.4 nF, and same capacitance readings were obtained by connecting pin 4 to pin 6, 7, and through up to 20, respectively (**Figure 2-3**). While the capacitance between pin 1 to pin 2, 3, and 4 was 0 nF, and the capacitance between pin 4 and pin 21 could not be measured as it exceeded the limit of multimeter. These measurements indicated that pin 4 was the ground of the circuit, and pin 5, 6, 7, 8, and pin 20 were connected to the piezoelectric nozzles. Additionally, pin 21 was also connected to the ground of the circuit as same capacitance readings were obtained between pin 21 to pin 5, 6, 7, up to 20.

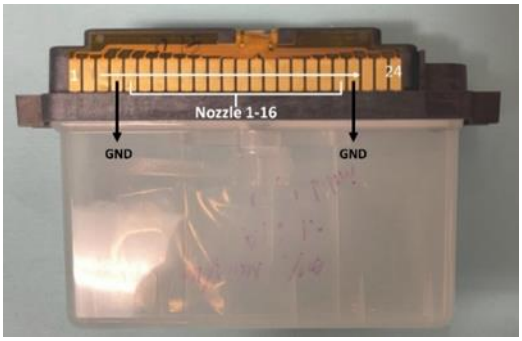

Figure 2-3. The cartridges (Dimatix DMC11610, 10 pico-liter nozzles) are composed of an ink reservoir and piezo-driven jetting head. From left to right, the pins are named as pin 1, pin 2, until pin 24. pin 4 and pin 21 are connected to the ground in the circuit, and pin 5 to pin 20 control the 16 nozzles by connecting to GND.

Therefore, the droplets can be ejected by connecting one wire from the output of waveform amplifier to the ground, which is either pin 4 or pin 21, and the other wire to any pin between 5 to 20. To test the setup, we employed cameras to monitor the formation of droplets, as shown in **Figure 2-4**, droplets were ejected continuously upon connecting pin 4 to pin 12. We also noticed that the trajectory of droplet is not strange as expected. This could be due to the slight differences resulting from the amplification of the waveform function or the air flow in the ambient environment.

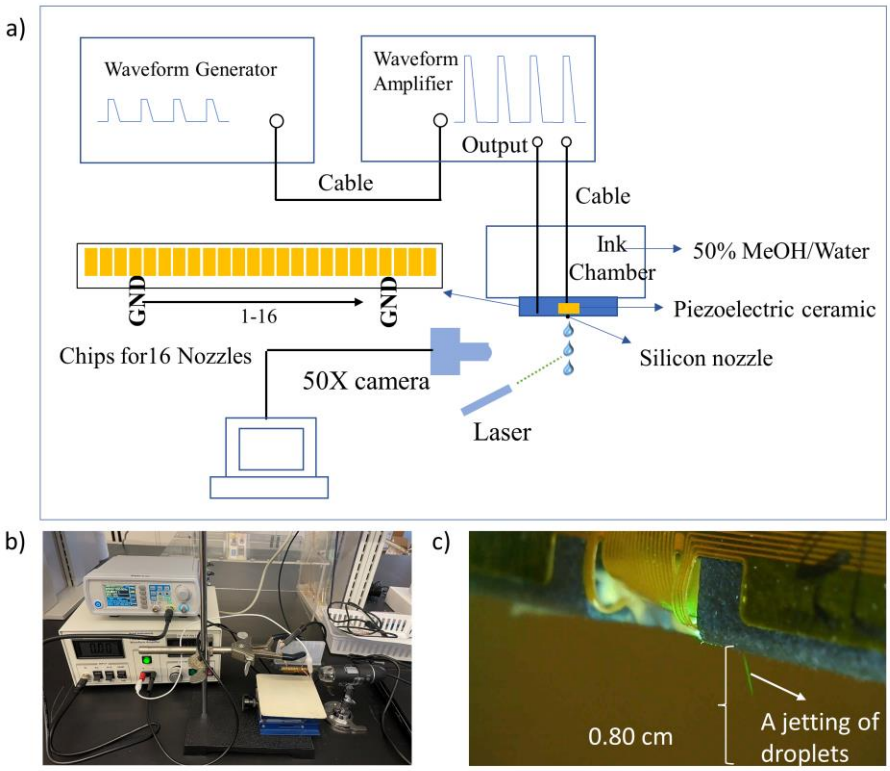

Figure 2-4 a) schematic of setup to generate pico-liter droplet. The cartridge is placed vertically down to the substrate. The volume of ink should be between 0.2 ml and 1.5 ml. The droplets were squeezed out by applying jetting waveform on the piezoelectric nozzle at a frequency of 1 kHz and amplitude 5.3 v. The waveform was designed by signal generator and amplified by TS250 waveform amplifier with a gain of 10. The jetting of droplet was captured by camera.

2.3.4 Characterization of droplets

The volume of droplet was measured by weighing the mass of fluid after a certain period. The volume of droplet was found to be 9.5 ± 2 pL, shown in **Table 2-2**. Additionally, the volume of droplet was estimated by measuring the diameter of droplet based on the scale bar on the **Figure 2-1b**, a spherical droplet of 28 μm is 11 pL, which is in line with the mass method. The diameter of the droplet ejection for 20 second deposited on the substrate was around 2 mm, shown in **Figure 2-5**.

Table 2-2 The mass of fluid measured by balance after 20-second injection, the readability of the balance is 0.01 mg. The volume is obtained by dividing the mass to density (50% methanol/water: 0.93 ng/μL). The frequency is set to 1 kHz.

	Trial 1	Trial 2	Trial 3	Trial 4	Trial 5
Mass/mg	0.22	0.23	0.16	0.14	0.15
Volume/nL	237	247	172	151	161
Volume per droplet	10	13	8.6	7.2	7.7

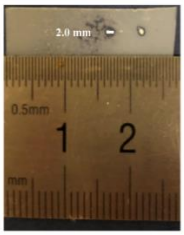

Figure 2-5 Deposited drops after 20-second ejection. The diameter of the droplet is 2.0 mm.

Furthermore, a high-speed camera with a delay time 100 μs to capture the jetting was used to measure the speed rate of droplet. A representative photo is shown in **Figure 2-1b**, the speed was calculated by dividing the distance between droplet and nozzle by the delay time of 100 μs. Therefore, the droplet speed is approximately 2 m/s.

2.4 Conclusions

In conclusion, we have developed a device for generating droplets using piezoelectric inkjet printing. The device is capable of producing droplets with a volume of 9.5 ± 2 pL and an ejection rate of 2 m/s. This makes it well-suited for applications such as delivering precise amounts of solvent for paper spray. Additionally, the slower ejection rate of the droplets generated by our device, compared to the velocity of ESI droplets (~20 m/s), allows for better monitoring droplet reactions. Overall, our device is an easy-to-construct and cost-effective method for generating droplets with a small droplet size, which is ideal for many applications in chemical and biological research.

2.5 References

(1) Zhang, H.; Liu, C.; Hua, W.; Ghislain, L. P.; Liu, J.; Aschenbrenner, L.; Noell, S.; Dirico, K. J.; Lanyon, L. F.; Steppan, C. M.; West, M.; Arnold, D. W.; Covey, T. R.; Datwani, S. S.; Troutman, M. D. Acoustic Ejection Mass Spectrometry for High-Throughput Analysis. *Anal. Chem.* **2021**, *93* (31), 10850–10861. https://doi.org/10.1021/acs.analchem.1c01137.

(2) Wang, Y.; Shaabani, S.; Ahmadianmoghaddam, M.; Gao, L.; Xu, R.; Kurpiewska, K.; Kalinowska-Tluscik, J.; Olechno, J.; Ellson, R.; Kossenjans, M.; Helan, V.; Groves, M.; Dömling, A. Acoustic Droplet Ejection Enabled Automated Reaction Scouting. *ACS Cent. Sci.* **2019**, *5* (3), 451–457. https://doi.org/10.1021/acscentsci.8b00782.

(3) Häbe, T. T.; Liu, C.; Covey, T. R.; Simon, R. P.; Reindl, W.; Büttner, F. H.; Winter, M.; Bischoff, D.; Luippold, A. H.; Runge, F. Ultrahigh-Throughput ESI-MS: Sampling Pushed to Six Samples per Second by Acoustic Ejection Mass Spectrometry. *Anal. Chem.* **2020**, *92* (18), 12242–12249. https://doi.org/10.1021/acs.analchem.0c01632.

(4) Ellson, R.; Mutz, M.; Browning, B.; Lee, L.; Miller, M. F.; Papen, R. Transfer of Low Nanoliter Volumes between Microplates Using Focused Acoustics—Automation Considerations. *JALA: Journal of the Association for Laboratory Automation* **2003**, *8* (5), 29–34. https://doi.org/10.1016/S1535-5535-03-00011-X.

(5) Shin, P.; Sung, J.; Lee, M. H. Control of Droplet Formation for Low Viscosity Fluid by Double Waveforms Applied to a Piezoelectric Inkjet Nozzle. *Microelectronics Reliability* **2011**, *51* (4), 797–804. https://doi.org/10.1016/j.microrel.2010.11.017.

(6) Luo, C.; Ma, Y.; Li, H.; Chen, F.; Uchiyama, K.; Lin, J.-M. Generation of Picoliter Droplets of Liquid for Electrospray Ionization with Piezoelectric Inkjet. *Journal of Mass Spectrometry* **2013**, *48* (3), 321–328. https://doi.org/10.1002/jms.3159.

(7) Yang, J.; Zeng, H.; Xue, S.; Chen, F.; Nakajima, H.; Uchiyama, K. Quantitative-Nanoliter Immunoassay in Capillary Immune Microreactor Adopted Inkjet Technology. *Analytical Methods* **2014**, *6* (9), 2832–2836. https://doi.org/10.1039/C4AY00216D.

(8) Jang, D.; Kim, D.; Moon, J. Influence of Fluid Physical Properties on Ink-Jet Printability. *Langmuir* **2009**, *25* (5), 2629–2635. https://doi.org/10.1021/la900059m.

3 Evaluation of Novel Scan Function in Improving the Precision of Quantitative Analysis for Linear Ion Trap Mass Spectrometry

3.1 Introduction

Quantitative analysis using mass spectrometry involves measuring the *m/z* and intensity of ions in a sample. The intensity of a specific ion directly reflects the amount of analyte present in the sample.[1] However, the intensity of ions in electrospray ionization (ESI) mass spectra can be influenced by various factors such as the properties of the analytes (pKa, polarity),[2] the spray solvent composition, and the ESI sources.[3] To address the issue, the use of an isotopically labeled internal standard has become a common practice in quantitative analysis based on mass spectrometry. This method helps to correct for variations in the electrospray ionization (ESI) process and allows for the development of a calibration curve based on the ratio of the peak area or intensity of the analyte and internal standard.[4,5] Two commonly used scan modes are MS and MS/MS scans. In MS scans, the mass analyzer is scanned from the first to the last mass without interruption to produce a full mass spectrum of the parent ions. In MS/MS scans, which can improve the S/N ratio compared to MS scan,[6] the selected precursor ions are fragmented into product ions, which are then sequentially scanned out of the mass analyzer to produce a full product ion mass spectrum.

Since the development of ambient ESI mass spectrometric analysis by Cooks group[7], many researchers have attempted to directly ionize analytes from various substrates, such as paper,[8] wooden tip,[9] and leaves[10]. However, this method is associated with significant scan-to-scan variations due to the inherent variability in the porous substrates. Therefore, the variance can distort the ratio of the two consecutive scans for analyte and IS respectively, deteriorating the quantitative performance of the cutting-edge techniques.

To have the analyte and its internal standard (IS) scanned at the same time is not a new thing. Based on the idea of concurrently isolation multiple discrete ion populations with isolation waveforms that have multiple frequency notches were developed in mid-1980s by Marshall,[11] a method known as SWIFT. In 2002, Schwatz Jae C reported a linear two-dimensional (2D) quadrupole ion trap, where resonance excitation was utilized for ions isolation.[12] In 2014, the Gygi group used isolation waveforms with multiple frequency notches to co-isolate and co-fragment multiple MS/MS fragment ions, which yielded high-quality quantitative measurements.[13] In addition, Cooks group has taken advantage of the dual resonance frequencies to co-isolate targeted ions.[14] In 2018, a novel method for precise quantitative analysis for linear ion trap tandem mass spectrometry has been developed by Li et al.[15] Compared to existing conventional methods that require the analyte and corresponding internal standard ions to be injected and analyzed using two successive mass analysis scans, the precursor ions of the analyte and internal standard are simultaneously isolated from the background using a dual-notch (2 amu q=0.86) waveform, each with its own ion injection event, the new methodology allows the linear ion trap mass spectrometer to perform tandem mass analyses of the analyte and the internal standard, but utilizes one ion injection event. This minimizes the quantitation inaccuracies introduced by ionization fluctuations and leads to significant improvements in the precision of quantitative analyses. In this study, we evaluated the novel scan in improving the quantitative precision of linear ion trap mass spectrometric analysis using pulsed ion source, which has a significant scan-to-scan variation.

3.2 Experimental

3.2.1 Novel scan function

The novel scan function was achieved by replacing several files in the control directory (C:/Thermo/Instruments/LTQ/system/itcl) provided by Thermo Fisher, followed by resetting the

power panel. In collaboration with Thermo Scientific, we tested the scan function codes provided by Dr. Linfan Li and found that one version of the codes worked well on our instrumentation. Therefore, the version was used and evaluated in this study. The parameters for the new scan function were set in the define scan dialog box in the LTQ tune window, shown in **Figure 3-1**. To set the parameters, type .01 after the targeted first ion's *m/z* value in the Parent Mass (*m/z*) box and enter the *m/z* difference between the first and second precursors in the Max. Inject time (ms) box. For example, if the first m/z is 413 and the second is 421, we should input 413.01 into the Parent Mass (*m/z*) box and 100.08 in the Max. Inject time (ms) box, which refers to a max. injection time of 100 ms and a m/z difference of 8 Da. This allows for simultaneous fragmentation and scanning of two precursors (*m/z* 413 and *m/z* 421) in one scan event.

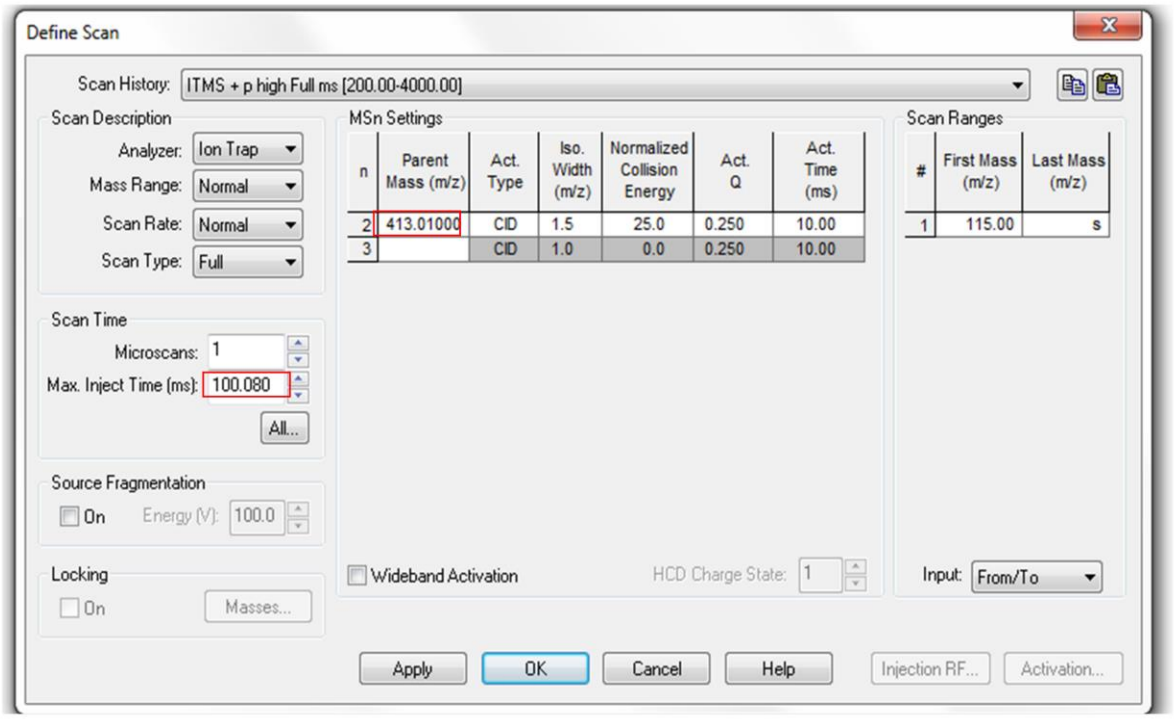

Figure 3-1 Define the novel scan in the define scan dialog box. Type 413.01 (not 413) in Parent Mass (m/z) for first m/z of 413, 100.08 in Max. Inject time (ms) for second m/z of 421 and m/z difference of 8 with default max. injection time of 100 ms.

3.2.2 Measure mass analyzer rf/waveform voltages at different scan mode

The PCB (printed circuit board) to control the mass analyzer rf/waveform voltages was reached by removing the top cover after disconnecting electrical cables with the help of our collaborator Dr. Linfan Li. The rf voltages were measured by connecting the components with code DET to the oscilloscope, as shown in **Figure 3-2**.

Figure 3-2 Overview of LTQ mass spectrometry after removing the cover, the left side was the vacuum manifold that enclosed ion optics, mass analyzer, and ion detection system. The PCB for mass analyzer rf voltage was next to the vacuum manifold. Photographs of measuring rf voltages 2) disconnected the electronic cables, 3) found the transformer components with code "TED" on the PCB, and 3) connected with the oscilloscope.

3.2.3 Chemicals and Materials

Borosilicate glasses with and without filament (ID 0.86mm) were sourced from Sutter Instrument (Novato, CA, USA). The glasses were drawn into circular cone emitters, 4.75 ± 0.30 cm in length, using a Model P-1000 Micropipette Puller from Sutter Instrument. The emitter tip size was determined to be 3.9 ± 0.3 µm. The DC power supply and signal generator were acquired from Amazon (Seattle, WA, USA).

LC-MS grade water and methanol were purchased from Sigma-Aldrich (St. Louis, MO, USA). Perfluorooctanoic acid (PFOA) analytical standard was purchased from AccuStandards Co. Ltd. (NewHaven, CT, USA). $^{13}C_8$-PFOA was purchased from Cambridge Isotope Laboratories, lnc. (Tewksbury, MA, USA). PFOA powder was carefully weighed and dissolved in methanol to obtain 1mg/mL stock solution. The stock was further diluted in methanol and stored. at 4 °C prior to analysis. Pierce LTQ ESI positive ion calibration solution purchased from Thermo was used to test the novel scan function.

3.2.4 Sample Preparation

All the working solutions were prepared by serial dilution with methanol. Seven perfluorooctanoic acid (PFOA) solutions, ranging from 0.02 to 0.8µM, were prepared in MeOH with spiked internal standard (0.12 µM, $^{13}C_8$PFOA) in all the standards.

3.2.5 Continuous ionization sources

Continuous ion source was a typical nanoESI source, in which a platinum wire was inserted into the glass emitter containing sample solution, the tip of which was placed pointing to the MS inlet with a distance of 0.5 cm. By applying 1.5 kV spray voltage on the platinum wire, the analytes in the sample were continuously ionized, shown in **scheme 3-1a**.

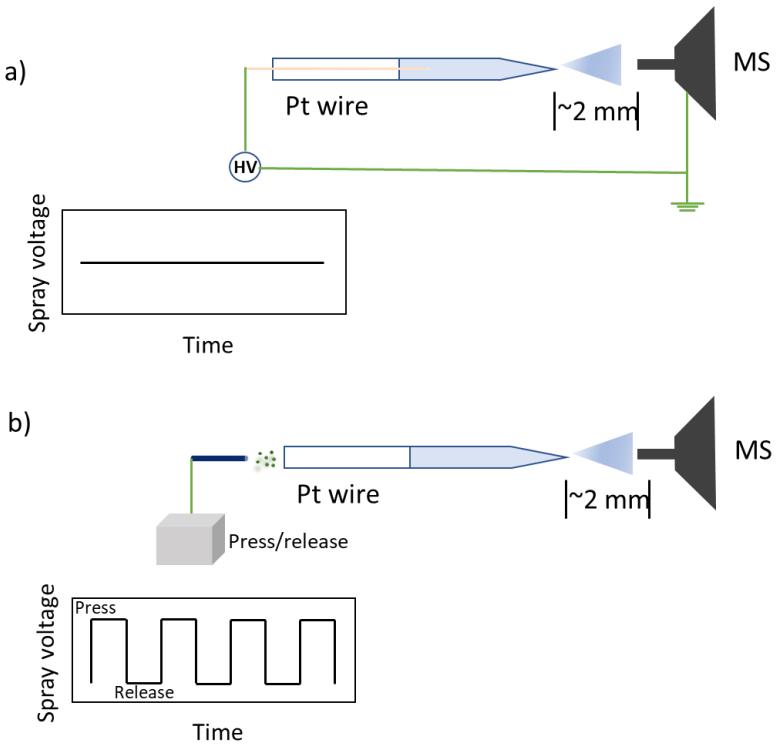

Scheme 3-1. a) Schematic of continuous ion source; b) schematic of pulsed ion source.

3.2.6 Pulsed ionization sources

Pulsed ion source was achieved by the relay plasma, onto which a square voltage waveform with a frequency of 0.5 Hz and a voltage of 10.0 volts were applied. Continuously pressing and releasing of the piezoelectric materials via a homemade robot arm produced positive and negative charges, respectively (**Figure 3-3, the device was constructed by Dr. Anyin Li**). The analytes were ionized by depositing the primary ions onto the glass emitter from a distance of 2 mm behind the needle that contained the sample solution. This triggered the ionization process, shown in **scheme 3-1b.**

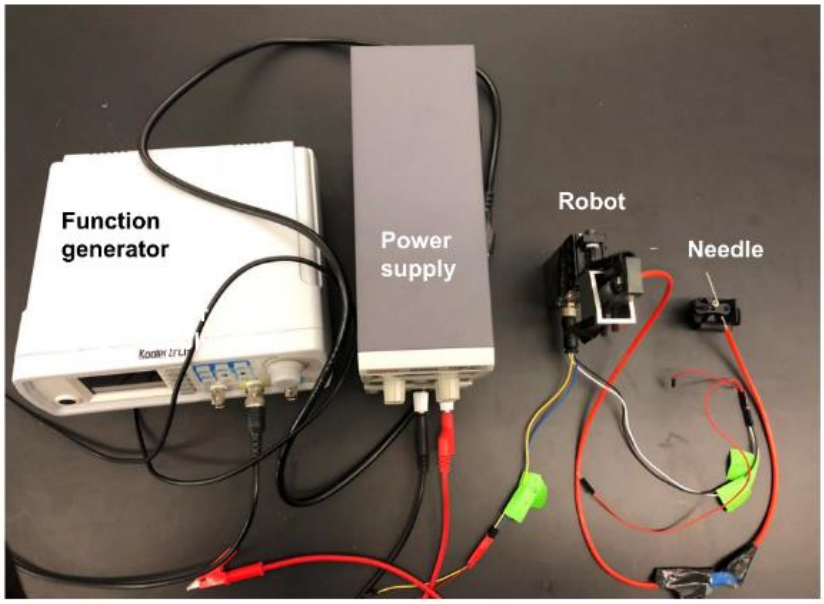

Figure 3-3.A device to generate piezoelectric plasma. The function generator is used to produce waveform function. A square waveform at a frequency of 0.5 Hz and 10 volts provided by DC power supply are applied on the home-made robot arm that connects to a stainless needle to trigger the generation of plasma by pressing and releasing the piezoelectric material.

3.2.7 Mass Analysis

A modified Thermo Scientific™ LTQ-Orbitrap Velos mass spectrometer (Thermos fisher, San Jose, CA, USA) was used in this study. The parameters were set as follows: capillary temp: 150.0 ºC, S-lens RF levels: 60.0, all the gas flow rates: 0. Max. injection time: 100 ms. Microscans: 1. For both MS/MS scan and the novel scan mode, the activation Q was 0.25, and the activation time was 25 ms, unless otherwise stated. All the samples were analyzed using both a conventional continuous nanoESI and a home-built pulsed nanoESI source.

3.2.8 Data process

Data were collected using the same samples for comparison. All the experimental data acquisition was processed with Xcalibur 4.0 software (Thermos Scientific, San Jose, CA, USA); Data analysis was carried out by using Microsoft Excel. The intensities of the selected peaks were used to calculate the relative intensity ratios of analyte/IS.

3.3 Results and discussions

3.3.1 Novel scan function on a hybrid linear ion trap/orbitrap mass spectrometer

The novel scan function developed by Li et al. has been evaluated on a mass spectrometer with a single linear ion trap mass analyzer. However, applying it to a hybrid LTQ Orbitrap, which has two independent detectors, requires significant effort. To provide a better understanding of the novel scan function, a brief description of the conventional MS/MS scan process in an LTQ is included. As illustrated in **Scheme 3-2**, ions produced in the ionization source are transferred to and accumulated in the ion trap mass analyzer. The targeted ions are then isolated by applying a multi-frequency waveform to remove unwanted ions for milliseconds. As the voltage increases, the q-value of the ion increases until reaching its stability limit. The ion is then ejected and scanned.

Finally, the ions are activated with helium gas and fragmented by increasing the RF voltage, generating a mass spectrum.

Scheme 3-2. S1: ions produced in electrospray ionization injected into ion trap, S2: isolation of desired ion in the ion trap, CID: collision-induced dissociation, A: mass analysis by scanning out of ions in the ion trap.

In this study, caffeine's protonated ion at *m/z* 195 and sodiated ion at *m/z* 217 with a mass difference of 22 are used to evaluate a new function. This function allows for the isolation of two precursor ions in a single scan event, **Figure 3-4**. The corresponding RF voltage waveform was shown in **Figure 3-5**. The cycle time for this scan is the same as for conventional MS/MS scan, in which the analyte and IS are scanned out in separate scan events. The novel scan mode also includes AGC (automatic gain control) scan time, ion injection time, parent ion isolation and activation time, and mass analysis time. AGC is a pre-scan to limit ions in the mass analyzer and reduce the space charge effect which could impact resolution and mass accuracy. The cycle time remains constant when the rate of ions being scanned out is kept equal to a conventional scan mode.

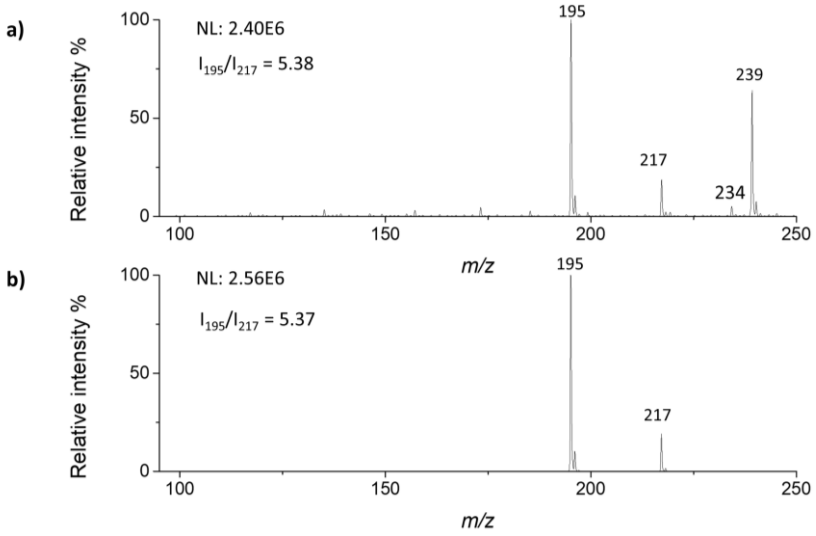

Figure 3-4**.** Comparison of relative signal intensity of $[M+H]^+$ at *m/z* 195 and $[M+Na]^+$ at *m/z* 217 in two scan mode a) full MS scan mode and b) novel scan mode. An average of 40 scans

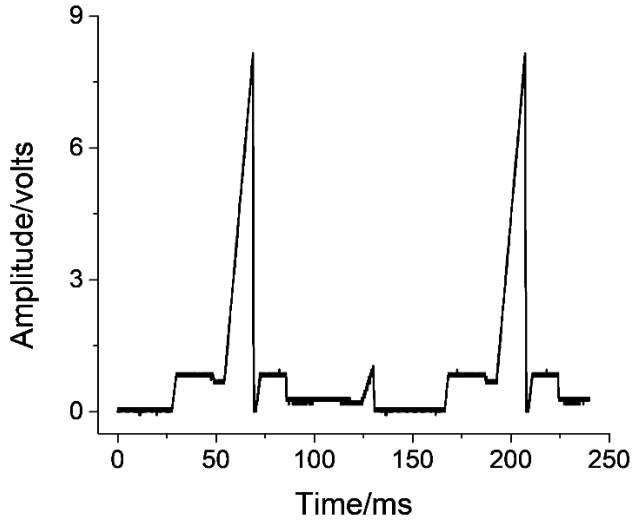

Figure 3-5. The novel scan function was measured with AGC enabled. The parameters used were 195.01 for the m/z value and 4 for the isolation width, with ion trap time of 100 ms.

The isolation width effect on the relative intensity of two precursors in the novel scan mode was investigated using 20 mg/L caffeine in 94% acetonitrile/water in the novel scan mode. As shown in **Figure 3-6**, the signal of the ion at *m/z* 195 remained stable as the isolation width decreased, while the signal of the ion at *m/z* 217 decreased when the isolation width was reduced to 3 and disappeared when it was reduced to 1. This demonstrated an isolation bias in the mass analyzer, leading to the use of a wider isolation width of 4 in this new scan function. The results confirmed that both precursor ions were isolated into the mass analyzer equally with a wider isolation window as the signal ratio between the two precursors was almost identical in both the novel and full scan modes.

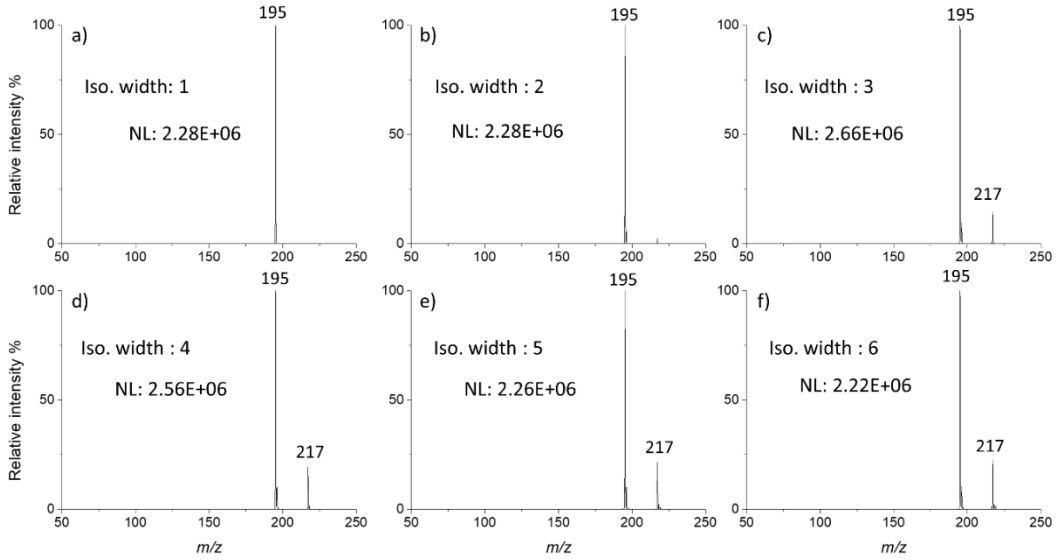

Figure 3-6 Influence of the isolation widths on the signal intensity of the 1st precursor at *m/z* 195 and 2nd precursor at m/z 217. The ESI positive calibrant solution (containing 20 mg/L caffeine) was electrosprayed by inserting Pt wire into the glass capillary. 1.5 kV spray voltage was applied. The mass spectrum was an average of 40 scans.

In addition, the fragmentation of two precursors in both conventional scan mode and novel scan mode was investigated. The first precursor ion at *m/z* 195 yields a product ion at *m/z* 138 by losing 57 Da corresponding to the group $(CH_2)N(CO)$. It is apparent that the fragmentation pattern in $[M+Na]^+$ is distinct from that of $[M+H]^+$ ions. Similar observations have been obtained in the fragmentation behaviors of $[M+H]^+$ and $[M+Na]^+$ of neutral peptides.[16] The different product ions can prevent overlap of peaks with the same *m/z* value, enabling the evaluation of the novel scan function. **Figure 3-7** shows that the signal ratio of the major product ion *m/z* 138 to *m/z* 155 in the novel scan mode is 1.71, which is 62% lower than that obtained in the conventional scan mode. This implies a bias in the fragmentation of protonated ion and sodium adduct. To verify that the bias was not caused by variations in gas phase structures (protonated versus sodiated), an isotopically labeled compound was employed to reassess the performance of the novel scan mode. A mixture of 0.1 µM PFOA and 0.12 µM $^{13}C_8$-PFOA was analyzed in both modes. The peak of *m/z* 369 corresponding to a neutral loss of CO_2 from $[M-H]^-$was detected in the MS/MS spectra. The relative intensity ratio of ion at *m/z* 369 to *m/z* 376 in the novel scan mode is 1.4, which is only 16% higher than the ratio in the conventional MS/MS scan mode, **Figure 3-8**. This outcome suggests that the fragmentation bias observed in the novel scan mode might be attributed to the differing gas phase structures, which can potentially be reduced with isotopically labeled internal standards in future investigations.

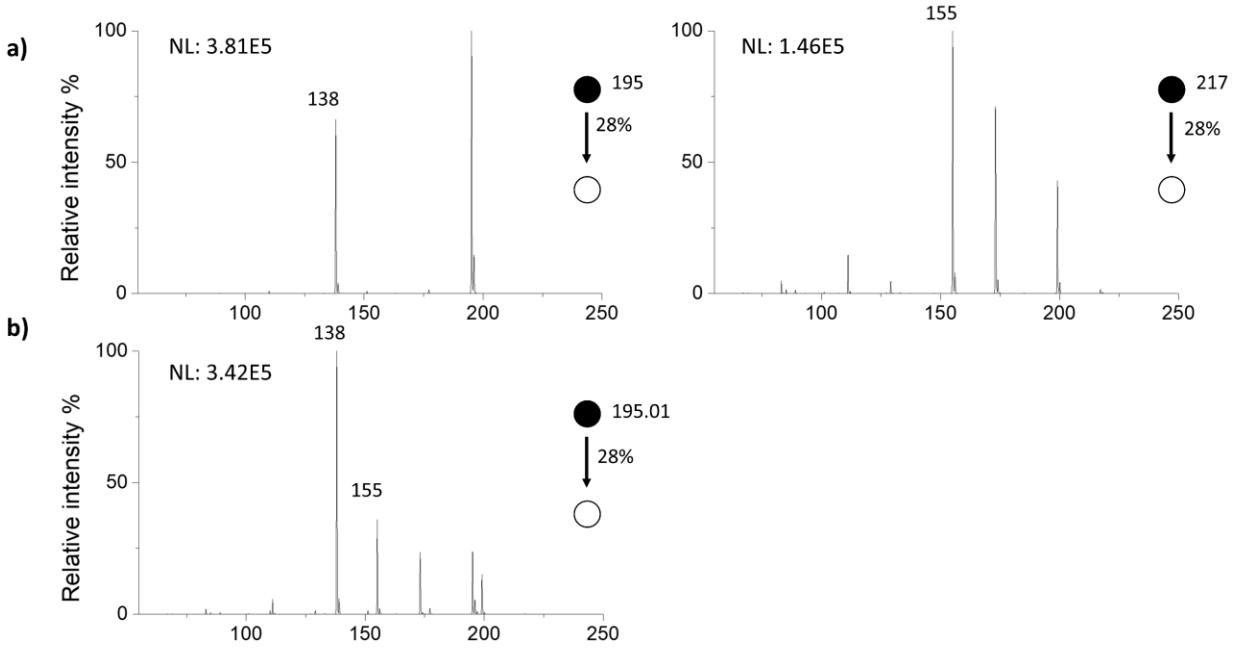

Figure 3-7. Comparison of relative intensity of product ion *m/z* 138 from precursor *m/z* 195 to another product ion at m/z 155 from 2nd precursor ion at *m/z* 217 in two scan modes a) novel scan mode and b) conventional MS/MS scan mode. The collision energy was 28%.

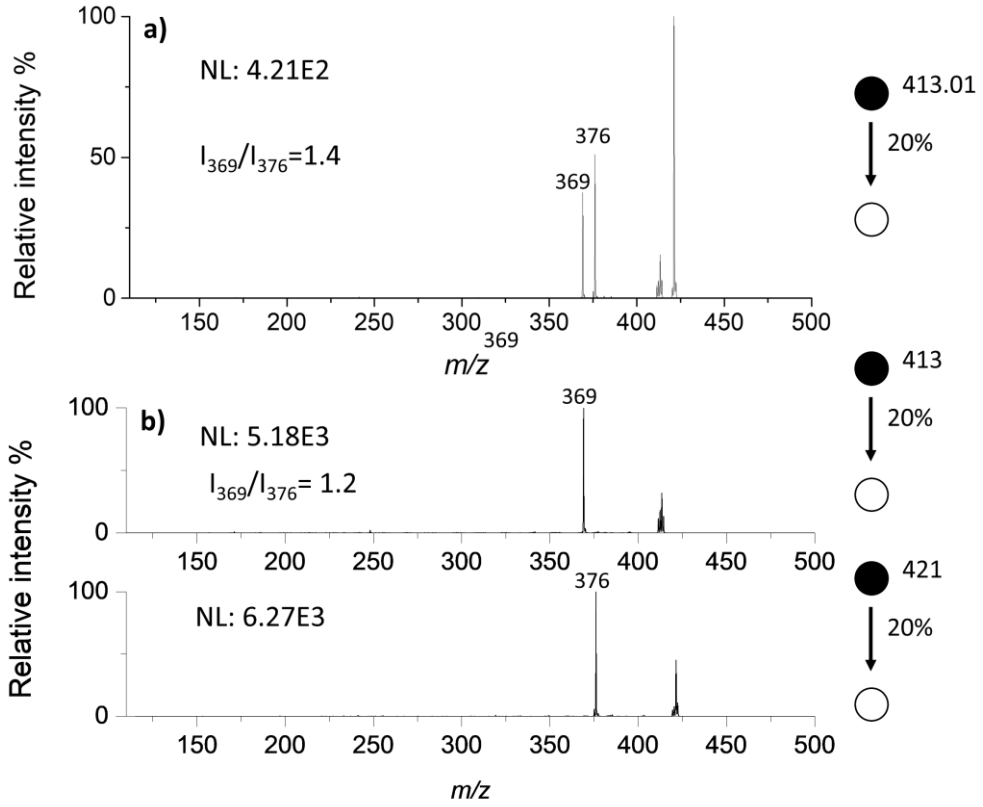

Figure 3-8. Comparison of relative intensity of product ion *m/z* 369 from PFOA to *m/z* 376 from $^{13}C_8$-PFOA in two scan modes a) novel scan mode and b) conventional MS/MS scan mode. The collision energy was 20%.

3.3.2 The evaluations of the novel scan using continuous ion source

To assess the accuracy of the novel scan mode for quantitative analysis, perfluorooctanoic acid (PFOA) was used as the model compound, along with an isotopically labeled internal standard, to create quantitative calibration curves. The concentration range spanned from 0.02 μM to 0.8 μM and the signal ratio between the analyte and internal standard was monitored. The setup is shown in **Scheme 3-1a**, which features a typical home-built nano-electrospray ion source powered by direct current (DC). During the quantitative analysis, transitions of 413->369 and 421->376 are used for PFOA and its IS (**Figure 3-8**), respectively, when the ions were analyzed by the ion trap. A 5-ppm (part per million) mass window was used in the peak selection when the ions were analyzed by the orbitrap. The intensities of the selected product ions' peaks were used to calculate the relative intensity ratios of analyte/IS. The results of ten consecutive scans were recorded and used to calculate the relative standard deviation (RSD), as a measure of the precision comparison. As shown in **Figure 3-9**, the calibration curves were linear with similar R^2 larger than 0.98. However, a nearly 3-fold decrease in RSD (7%) was observed when using the novel scan mode as compared to those (24%) obtained using conventional ion trap MS/MS scan. Meanwhile, there was no significant difference between the full scan using Orbitrap mass analyzer and the novel scan function (11% vs. 7%), as expected since both analyte and IS are scanned in one event under the two scan modes. Therefore, the novel scan mode can significantly improve precision compared to conventional MS/MS scan mode, in which the analyte and IS are scanned out separately in two consecutive events.

1)

# scan	Scan type		
	Full Scan (Orbitrap)	Novel scan	Conventional scan
1	0.81	0.67	0.88
2	0.81	0.67	0.65
3	0.81	0.70	0.65
4	0.82	0.70	0.86
5	0.67	0.57	1.02
6	0.76	0.70	0.64
7	0.73	0.62	1.11
8	0.68	0.67	0.73
9	0.83	0.63	0.68
10	0.96	0.71	1.15
Mean	0.79	0.66	0.84
Std	0.08	0.05	0.20
RSD	11%	7%	24%

2)

Scan Mode		Concentration of PFOA (μM)						
		0.02	0.04	0.1	0.2	0.40	0.8	1.0
Full Scan	RSD	15%	12%	11%	13%	13%	10%	7%
Novel scan		12%	11%	7%	11%	9%	15%	13%
Conventional scan		17%	48%	24%	12%	24%	32%	24%

3)

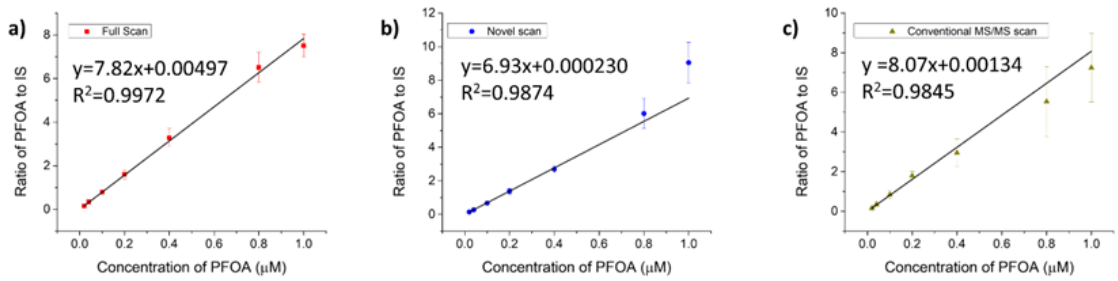

Figure 3-9. 1) The results for 10 consecutive scans of 0.1 μM PFOA (IS: 0.12 μM) with 3 different scan modes, obtained by each of the three scan methods. The theoretical ratio of PFOA to IS was 0.83. 2) Evaluation of precision of three scan modes at five concentration points of PFOA with the relative standard deviation (RSD)**.** 3). Calibration curves of PFOA in concentration range of 0.02 to 1.0 μM with three scan mode: a) full scan, b) novel scan and c) conventional MS/MS scan.

3.3.3 The evaluation of the novel scan using pulsed ion source

The improvement in quantitative precision becomes much more apparent when a pulsed ion source is utilized. The setup was depicted in **Scheme 3-1b**, where the spray voltage rapidly alternates between positive and negative at a set duty cycle. Both the novel scan and the conventional scan were performed on the analysis of 50 μg/L PFOA and $^{13}C_8$ PFOA, shown in **Figure 3-10**. The variation of total ion current (TIC) in pulsed ion source was 178%, which is 90-fold higher compared to that in the continuous ion source (7.9%). The scan-to-scan intensity ratio between analyte and IS has improved from 88% for the conventional scan to 23% for the novel scan.

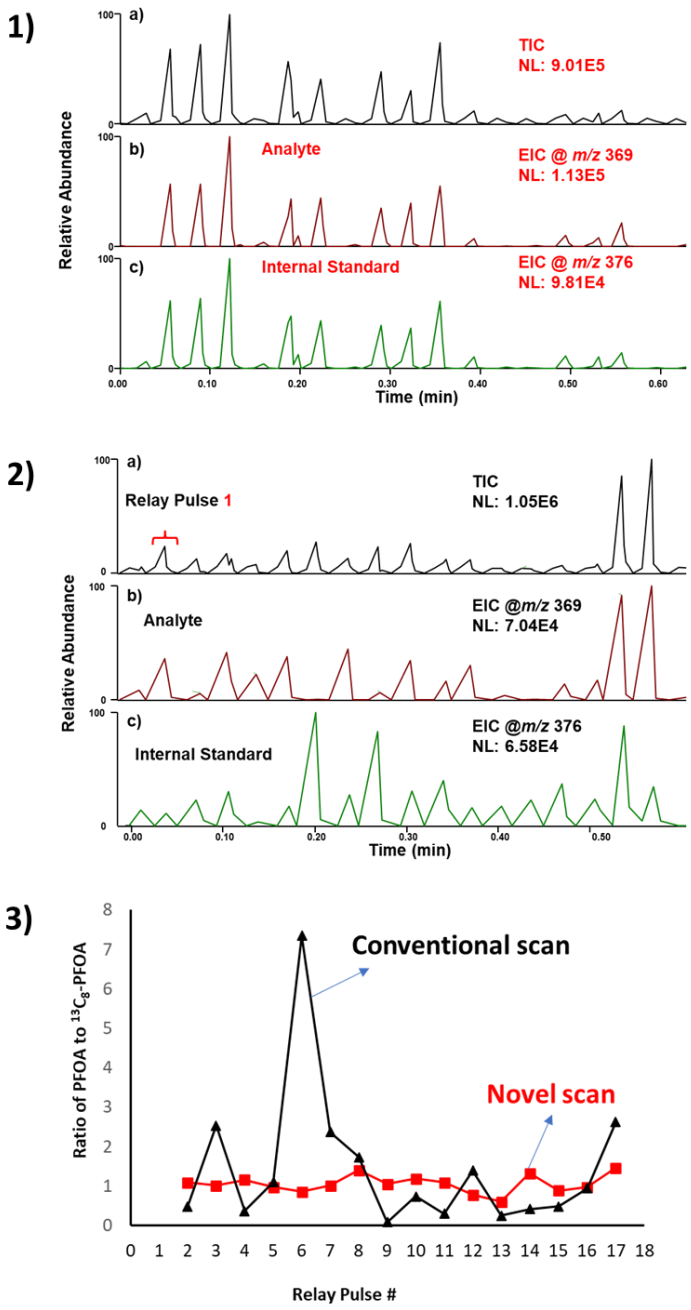

Figure 3-10. 1) . Novel scan mode MS analysis of 50 µg/L PFOA and $^{13}C_8$ PFOA (1:1) in MeOH with (pulsed) Relay ESI; Quantifier ions of *m/z* 369 and *m/z* 376 were used for PFOA and $^{13}C_8$ PFOA respectively. a) Total ion chromatograph, b) EIC of m/z 369, c) EIC of m/z 376; 2). Conventional MS/MS analysis of 50 µg/L PFOA and $^{13}C_8$ PFOA (1:1) in MeOH with (pulsed) Relay ESI; Quantifier ions of *m/z* 369 and *m/z* 376 were used for PFOA and $^{13}C_8$ PFOA respectively. a) Total ion chromatograph, b) Extracted ion chromatograph of *m/z* 369, c) Extracted ion chromatograph of *m/z* 376**.** 3) Comparison of the novel scan and conventional scan (n=16) when analyzing 50 µg/L PFOA and $^{13}C_8$ PFOA with pulsed ion source. The theoretical ratio of Analyte/IS was 1.0. The measured ratios were obtained by calculating the intensities of selected peaks; herein quantitative transitions of 413->369 and 421->376 were used for PFOA and its IS, respectively.

3.4 Conclusions

In conclusion, the novel scan function developed and patented by Thermo Scientific [15,17] was evaluated in a hybrid LTQ mass spectrometer. The rf scan cycle in the novel scan was same as the conventional scan, suggesting a better utilization of ions generated in ESI. It was found that the novel scan mode required a wider isolation width compared to the conventional MS/MS scan mode, which was set at 4 in future study. In the quantitative study involving the use of the novel scan, it is recommended to utilize isotopically labeled IS due to the observation of biased fragmentation in protonated and sodiated caffeine ions. The precision was significantly enhanced in both the continuous ion source and the pulsed ion source. However, the measured value using the novel scan function was found to be slightly lower than the true value, which requires further investigations.

3.5 References

(1) Tang, Liang.; Kebarle, Paul. Dependence of Ion Intensity in Electrospray Mass Spectrometry on the Concentration of the Analytes in the Electrosprayed Solution. *Anal. Chem.* **1993**, *65* (24), 3654–3668. https://doi.org/10.1021/ac00072a020.

(2) Oss, M.; Kruve, A.; Herodes, K.; Leito, I. Electrospray Ionization Efficiency Scale of Organic Compounds. *Anal. Chem.* **2010**, *82* (7), 2865–2872. https://doi.org/10.1021/ac902856t.

(3) Kiontke, A.; Oliveira-Birkmeier, A.; Opitz, A.; Birkemeyer, C. Electrospray Ionization Efficiency Is Dependent on Different Molecular Descriptors with Respect to Solvent PH and Instrumental Configuration. *PLoS One* **2016**, *11* (12), e0167502. https://doi.org/10.1371/journal.pone.0167502.

(4) Hewavitharana, A. K. Matrix Matching in Liquid Chromatography–Mass Spectrometry with Stable Isotope Labelled Internal Standards—Is It Necessary? *Journal of Chromatography A* **2011**, *1218* (2), 359–361. https://doi.org/10.1016/j.chroma.2010.11.047.

(5) Wu, J.; Wiegand, R.; LoRusso, P.; Li, J. A Stable Isotope-Labeled Internal Standard Is Essential for Correcting for the Interindividual Variability in the Recovery of Lapatinib from Cancer Patient Plasma in Quantitative LC-MS/MS Analysis. *J Chromatogr B Analyt Technol Biomed Life Sci* **2013**, *941*, 100–108. https://doi.org/10.1016/j.jchromb.2013.10.011.

(6) Del Mar Gómez-Ramos, M.; Rajski, Ł.; Heinzen, H.; Fernández-Alba, A. R. Liquid Chromatography Orbitrap Mass Spectrometry with Simultaneous Full Scan and Tandem MS/MS for Highly Selective Pesticide Residue Analysis. *Anal Bioanal Chem* **2015**, *407* (21), 6317–6326. https://doi.org/10.1007/s00216-015-8709-z.

(7) Takáts, Z.; Wiseman, J. M.; Gologan, B.; Cooks, R. G. Mass Spectrometry Sampling Under Ambient Conditions with Desorption Electrospray Ionization. *Science* **2004**, *306* (5695), 471–473. https://doi.org/10.1126/science.1104404.

(8) Kim, D.; Yim, U. H.; Kim, B.; Cha, S.; Kim, S. Paper Spray Chemical Ionization: Highly Sensitive Ambient Ionization Method for Low- and Nonpolar Aromatic Compounds. *Anal. Chem.* **2017**, *89* (17), 9056–9061. https://doi.org/10.1021/acs.analchem.7b01733.

(9) Hu, B.; Yao, Z.-P. Electrospray Ionization Mass Spectrometry with Wooden Tips: A Review. *Analytica Chimica Acta* **2022**, *1209*, 339136. https://doi.org/10.1016/j.aca.2021.339136.

(10) Zhang, J. I.; Li, X.; Ouyang, Z.; Cooks, R. G. Direct Analysis of Steviol Glycosides from Stevia Leaves by Ambient Ionization Mass Spectrometry Performed on Whole Leaves. *Analyst* **2012**, *137* (13), 3091–3098. https://doi.org/10.1039/C2AN16263F.

(11) Marshall, A. G.; Wang, T. C. L.; Ricca, T. L. Tailored Excitation for Fourier Transform Ion Cyclotron Mass Spectrometry. *J. Am. Chem. Soc.* **1985**, *107* (26), 7893–7897. https://doi.org/10.1021/ja00312a015.

(12) Schwartz, J. C.; Senko, M. W.; Syka, J. E. P. A Two-Dimensional Quadrupole Ion Trap Mass Spectrometer. *Journal of the American Society for Mass Spectrometry* **2002**, *13* (6), 659–669. https://doi.org/10.1016/S1044-0305(02)00384-7.

(13) McAlister, G. C.; Nusinow, D. P.; Jedrychowski, M. P.; Wühr, M.; Huttlin, E. L.; Erickson, B. K.; Rad, R.; Haas, W.; Gygi, S. P. MultiNotch MS3 Enables Accurate, Sensitive, and Multiplexed Detection of Differential Expression across Cancer Cell Line Proteomes. *Anal. Chem.* **2014**, *86* (14), 7150–7158. https://doi.org/10.1021/ac502040v.

(14) Snyder, D. T.; Cooks, R. G. Ion Isolation in a Linear Ion Trap Using Dual Resonance Frequencies. *J. Am. Soc. Mass Spectrom.* **2016**, *27* (12), 1906–1913. https://doi.org/10.1007/s13361-016-1494-x.

(15) Li, L. Methods and Systems for Quantitative Mass Analysis. US9911588B1, March 6, 2018. https://patents.google.com/patent/US9911588B1/en (accessed 2023-02-10).

(16) Sabareesh, V.; Balaram, P. Tandem Electrospray Mass Spectrometric Studies of Proton and Sodium Ion Adducts of Neutral Peptides with Modified N- and C-Termini: Synthetic Model Peptides and Microheterogeneous Peptaibol Antibiotics. *Rapid Commun Mass Spectrom* **2006**, *20* (4), 618–628. https://doi.org/10.1002/rcm.2349.

(17) Li, L.; BAILEY, D. J. Methods and Systems for Quantitative Mass Analysis. US9911587B1, March 6, 2018. https://patents.google.com/patent/US9911587B1/en (accessed 2023-02-10)

4 Evaporation Induced Preconcentration of analytes in the NanoESI Analysis

4.1 Introduction

Ambient electrospray ionization (ESI) techniques have gained significant attention since their introduction in 2004 by Cooks group, as they allow ionization of samples in the open air with minimum sample preparation.[1] These techniques have shown promising results in various fields such as environmental[1], food[2], and biomolecule analysis[3,4], and forensic investigations[5]. Therefore, the direct mass spectrometry (MS) analysis, which only consumes a few microliters of sample with simple operation, exhibits great potential in the point-of-care diagnosis areas to replace traditional complex laboratory procedures. However, direct MS analysis techniques face challenges to analyze complex biological samples and trace analytes at ppt levels.

To address this challenge, researchers have developed various strategies to improve sensitivity and enable the analysis of ultra-small complex biological samples. One such approach involves utilizing the slug-flow microextraction inside the capillary emitter of 0.8 mm I.D. and 5 cm length for analyzing hydrophobic and hydrophilic compounds in biofluid samples.[6,7] This approach involves the sequential injection of extraction solvent and a portion of the sample solution into a pulled borosilicate glass capillary, followed by a simple action of tilting the capillary up and down to create slug-flow extraction. The overall sensitivity of the method is significantly improved by this process. Another approach involves coating the inner surface of a glass emitter (i.d. 0.8 mm) with an organic polymer (poly (acrylamide-ethylene glycol dimethacrylate) to enrich analytes from sample plugs transferred into the glass emitter. [8]

In addition to the microextraction strategies, researchers have attempted to decrease the matrix effect by manipulating the voltages applied to the capillary emitters, such as pulsed DC

voltage[9,10] and step-voltage [11]. Wang et al. have developed analyte migration electrospray ionization using capillary with 20 μm tip orifice for matrix removal.[12] Furthermore, heterogeneous ion transportation in the glass capillary (i.d. 0.7 mm) with nanoscale tip dimensions, which is contributed to the high electric field and concentration polarization phenomenon [13], has also been demonstrated.

In this study, we report a novel evaporation-induced preconcentration strategy to broaden the application of ESI-MS. Our inspiration came from Walker and Beebe's studies. In which they developed a device with a single straight channel that measures 2 cm in length, 200 μm in width, and 140 μm in height, and has one inlet (I.D. 2 mm) and one outlet port (I.D. 2 mm). The concentration takes place as the liquid is passively evaporated from the outlet of the prefilled channel. As the liquid evaporated, the liquid sample flowed from the inlet port toward the outlet port, accumulating the target analyte at the outlet port.[14] We discovered that the filamented glass capillary commonly used in the nanoESI analysis has a sub-channel regime around the filament that can store fluid at microliter scales,[15] making it a natural device for enriching analytes through evaporation.

4.2 Experimental

4.2.1 Materials and chemicals

Borosilicate glasses with filament and without filament (ID 0.86 mm) were purchased from Sutter Instrument (Novato, CA, USA). The borosilicate glasses were pulled into two tapered capillaries with a length of 4.75 ± 0.30 cm using a Model P-1000 micropipette puller (Sutter Instrument, CA, USA). The tip size of glass emitter was 3.9 ± 0.3 μm.

LC/MS grade water and methanol were from Sigma-Aldrich (Missouri, USA). HPLC grade methanol and ethyl acetate were purchased from Fisher Scientific (Pittsburgh, PA, USA); Methyl

red was purchased from Fisher Scientific (Pittsburgh, PA, USA); 2,7-Dichlorofluorescein (DCF) was purchased from Kodak (Rochester, NY, USA). Naphthol blue black (CAS: 1064-48-8) was purchased from Sigma (Missouri, USA).

The OHAUS analytical balance (Parsippany, NJ, U.S.A) was used to measure the mass of solution at Temperature 21 ºC with a humidity 65%. The data was processed with Excel.

4.2.2 Preconcentration procedures

A solution of 100 ng/L dichlorofluorescein (DCF) in acetyl acetate (10 µL) was loaded into the glass emitters with a micropipettor. The glass emitter was then placed horizontally on the sample holder device (Shown **Figure 4-1**) at room temperature to allow for solvent evaporation. Once the solvent dried, the bottom of the glass emitter was quickly dipped into the 1.5-mL centrifuge vial containing 100 µL methanol to backfill the solvent into the tip of the glass emitter through capillary action. The enrichment effect was evaluated by comparing the fluorescence intensity with IX73 Olympus fluorescence microscope (Palatine, IL, USA).

The emitter tip, which was filled with DCF solution, was placed on the objective stage of fluoresence microscope. To compare the intensity of two images, a fixed scaling (minimum value 150 and maximum value 3759) with GFP mode (excitation bands: 451-485 nm, 541-565 nm; emission bands: 500-523 nm, 584-675 nm) was applied. The excitation of DCF fluoresence occurred at 498 nm with emission at 522 nm (from Sigma Aldrich). Light from the mercury light source passed through the same objective and was filtered by a bandpass filter prior to being captured with the camera.

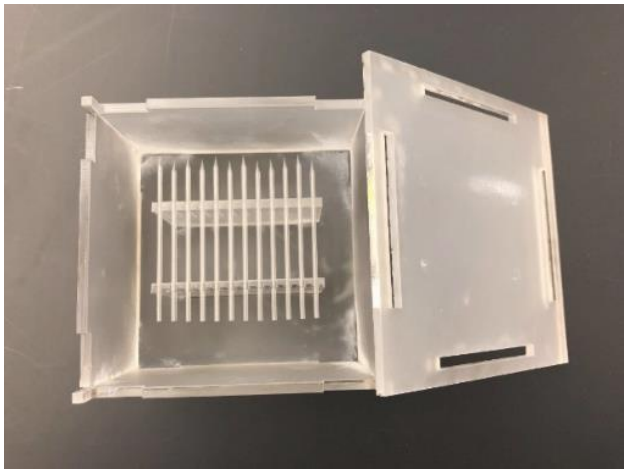

Figure 4-1 The photograph of the sample holder

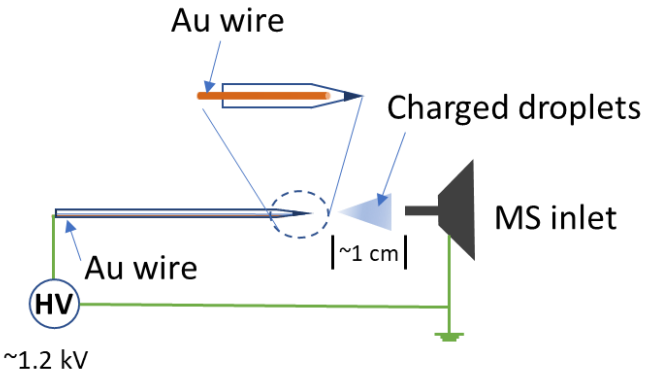

Scheme 4-1. The ionization method

4.2.3 ESI-MS analysis

The gold wire was positioned approximately 2 mm away from the sample meniscus for ionization (**Scheme4-1**). The spray voltage was 1.2 kV in the negative ion mode. The MS analysis of naphthol blue black (**Figure 4-2**) was performed on Thermo LTQ XL, with MS parameters: capillary temperature at 150°C, capillary voltage -36 V, Tube lens voltage: -57 V. The scan range was set from 100 to1000.

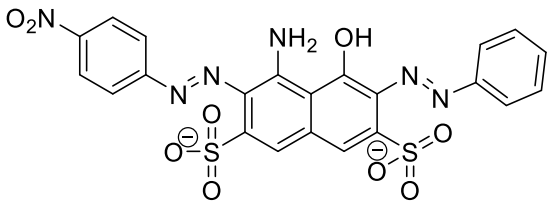

Figure 4-2. Structure of naphthol blue black

4.3 Results and discussions

The glass filament, with an outer diameter of approximately 160 μm, was annealed to the inner wall of a larger glass capillary with an inner diameter of 0.86 mm (O.D. 1.5 mm) [16]. The larger capillary was then molded into two grooved subchannels. After heat-pulling the capillary into two tapered shapes, fluid could flow through the subchannels via capillary action and accumulate at the tapered region. The grooved subchannels were visualized under fluoresence microscopy by backfilling the tapered glass emitter with a solution of 1 mg/L DCF dissolved in methanol, **Figure 4-3**. The volumes of fluid stored in the subchannels were estimated by subtracting the volume accumulated at the tip from the total volume of fluid. To determine the volume of fluid accumulated at the tip, we used the cone volume formula (**Figure 4-4**), which relies on measurements of the length (h) and diameter (d) of the cone. We obtained these measurements using microscopy. Meanwhile, the total volume of fluid was estimated using the mass obtained from the balance and divided it by the density of fluid. The estimated volume of the subchannel, as shown in **Table 4-1**, was 152 ± 42 nL. This result is consistent with the findings of our previous work, in which we demonstrated that the subchannel fluid could be sprayed for almost 5 hours at a flow rate of 0.4 nL/min, corresponding to a total volume of 120 nL.[15]

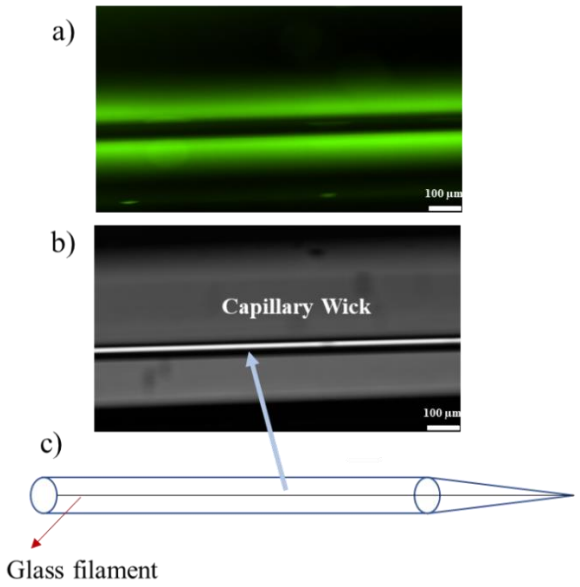

Figure 4-3. Photographs of the filamented glass emitter. a) the fluoresence image of 1 mL DCF in methanol, and its corresponding bright-field image is shown in b). The GFP mode with (exciter filter with dual band transmission: 451-485 nm and 541-565 nm) was used. Auto-exposure time was used.

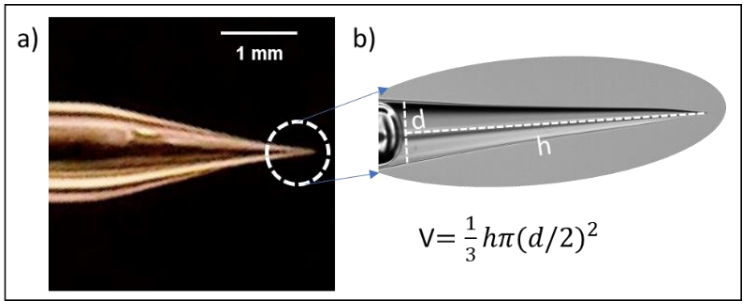

Figure 4-4 a) The photograph of emitter tip. The fluid at the tip b) was enlarged. The volume accumulated was estimated with the cone volume formula, where the length of the tangent line to the meniscus plane was supposed to be diameter d of the circular base, and the height h was distance between the tip to meniscus plane.

Table 4-1 The total volumes of fluid in the emitter and the volumes at the tips. The backfilling process was initiated with the inkjet printer, jetting for 30 seconds at 1 kHz. It should be noted that the transferring droplets into the subchannels requires careful alignment with the filament inside of the emitter, which can be challenging to control manually. The success rate was 4 out of 7 attempts. In order to obtain a more accurate estimate of the volume, it is important to ensure that the observable drops cling to the bottom of the emitter tips.

Trial #	**1**	**2**	**3**	**4**	**5**
Total V/nL	227	237	165	144	155
V_{tip}/nL	43	28	53	21	23
$V_{subchannel}$/nL	184	209	112	123	132

Additionally, the volume accumulated at the tip was found to be influenced by the way the emitter was positioned during the back filling. Specifically, when the emitter was positioned horizontally, the cone-shaped region of the emitter tip was almost filled with fluid. However, when the emitter was positioned vertically, only a small portion of fluid accumulated at the tip, **Figure 4-5**. It makes sense that when the emitter is placed horizontally, the capillary flow does not have to overcome the force of gravity, thus facilitating the accumulation of fluid. This finding suggests that the way to place the glass emitter is placed during back-filling should be carefully selected based on the desired volume of fluid at the tip. Meanwhile, there is a slight dependence on the length of emitter, which should also be taken into consideration in the practical applications.

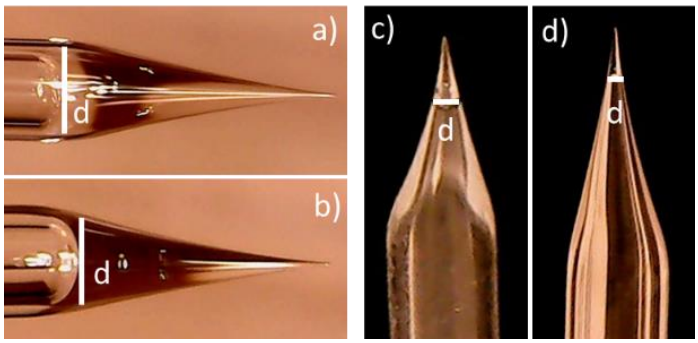

Figure 4-5 Effect of emitter placement on the tip volumes. Emitters a) and b) were placed horizontally with lengths of 37.2 mm and 38.0 mm, respectively. Emitters c) and d) were placed vertically with lengths of 67.6 mm and 38.2 mm, respectively. The emitters were placed into the 1.5-mL centrifuge vial containing 100 µL methanol for several quick dipping until the volumes at the tip does not increase, at which point the photos were taken.

A smaller volume is preferred in the preconcentration method; therefore, the backfilling process is always performed by vertically placing the emitters. As the case shown in **Figure 4-6**, at 1.3 min, the loading volume of methanol reached a maximum of 80 nL and did not change over time. Therefore, the average loading rate was estimated to be 970 pL/sec. The emitter with filament can be considered a highly efficient nanoliter sampling tool, as it eliminates the need for external pumps to drive fluid flow. Furthermore, the dip and go method employed with the emitter can prevent carryover and has great potential to automate the sample loading process, thereby replacing manual operations.[17] This approach can play a crucial role in enhancing the efficiency and reliability of various applications.

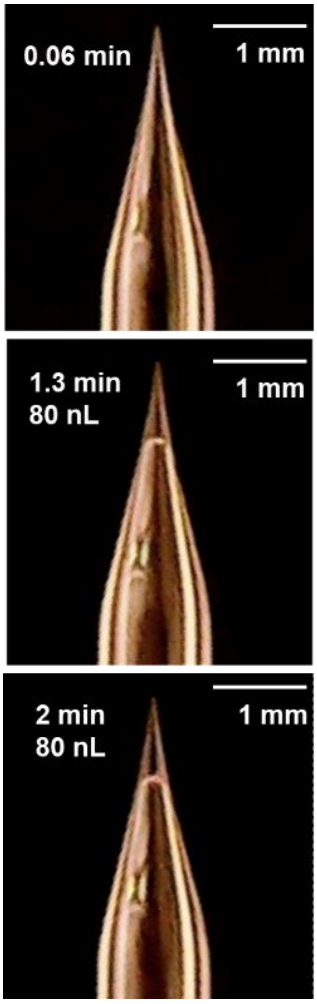

Figure 4-6. The backing filling of methanol in the filamented glass emitter via capillary action. The emitters were vertically placed.

The grooved subchannels in the filamented capillary, in addition to functions as a nanoliter sampling device through capillary action, have potentials to undergo an evaporation-induced outflow when the fluid volume exceeds the maximum volume that the capillary action can bring in. The evaporation-induced outflow behavior of fluids in the filamented glass emitter was investigated using ethyl acetate as the test fluid, with glass emitter without filament as the control. As illustrated in **Figure 4-7**, the ethyl acetate evaporation rate in the glass emitter with filament was found to be 0.17 µL/min, while the rate was significantly lower, estimated at 0.0022 µL/min, in the glass emitter without filament. This observation indicates that the subchannels allow outward fluid flow towards the proximal end of the emitter, driven by a higher evaporation rate at the end than the inner side.

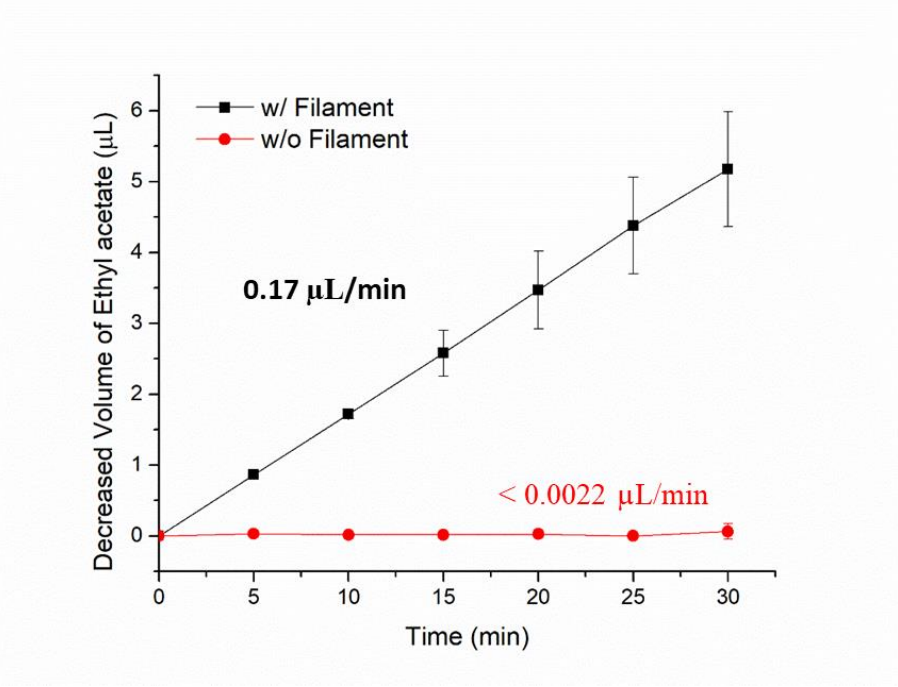

Figure 4-7. Comparison of evaporation rates of ethyl acetate in glass emitter w/ filament and w/o filament; the evaporation rate equals to the slope of the linear regression line; each data point is the average of three independent experiments and error bars represent the standard deviation. Each data point was obtained by measuring the weight of solvent every 5 minutes at 21 ºC.

This phenomenon is analogous to the coffee-ring effect, where a capillary flow induced by differential evaporation rates across a drop generates a ring-like pattern. In a similar manner, solute particles can be transported towards the edge of the drop by the fluid's outward flow. [18] To confirm this assumption, we loaded 10 μL light purple dye solution into the glass emitter and observed deep purple stains at the end of the glass emitter after the solvent dried (**Figure 4-8 a and b**). In fact, the coffee-ring deposition has been viewed as a robust preconcentration method for nonvolatile compounds, such as the so-called drop coating deposition Raman (DCDR) technique, which can preconcentrate protein solution and small molecules for Raman analysis.[19–21]

Furthermore, it is worth noting that when the loading volume exceeds a few microliters, the evaporation-induced outward flow becomes dominant. The capillary action to accumulate nanoliter solvents at the tip allows for the construction of a preconcentration device that can decrease the solvent volume from microliter to nanoliter level, as shown in **Figure 4-8c,** where the color of the solution deepens after the last step back filling, in which the upward flowing solvent extracts the solutes deposited at the bottom end of emitter and enriches them at the tip. Further evidence of the tapered glass emitter's role as a preconcentration device is provided by another case study using DCF, as illustrated in **Figure 4-9**, by extracting the deposited solutes into the nanoliter spray solvent, the 1 μg/L DCF (**Figure 4-9a**), which is below the detection limit of fluorescence microscopy, was preconcentrated to the extent that the bright green fluorescence was observed as the sample size was reduced from microliter to nanoliter (**Figure 4-9 b and d**).

Evaporation is a reliable and robust way to concentrate samples (**Scheme 4-2**). However, its performance relies on the ambient environment, such as humidity and room temperature. We observed that the solutes deposited at the end of the glass emitter (**Figure 4-10**) during the dip-

and-go backfilling method may inevitably diffuse into the extraction solvent reservoir, which can ultimately lessen the preconcentration effect.

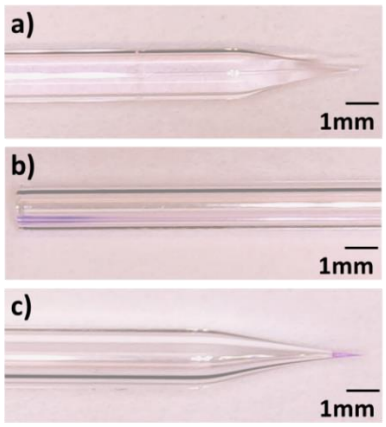

Figure 4-8. a) glass emitter loaded with 10 µL of colorless dye solution; b) Formation of deep purple stains at the end of the glass emitter after evaporation of solvents; c) Preconcentrated purple solution observed at the tip of the glass emitter.

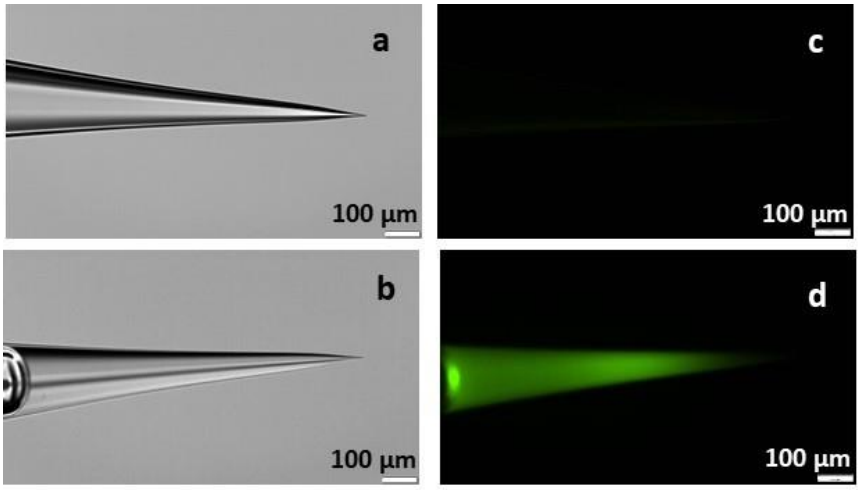

Figure 4-9. a) the bright field image of 1 µg/L DCF (2',7'-dichlorofluorescein) in methanol b) its fluoresence intensity under GXP mode. c) the bright field image of 1 µg/L DCF (2',7'-dichlorofluorescein) in methanol after preconcentration. d) its fluoresence intensity after preconcentration under GXP mode.

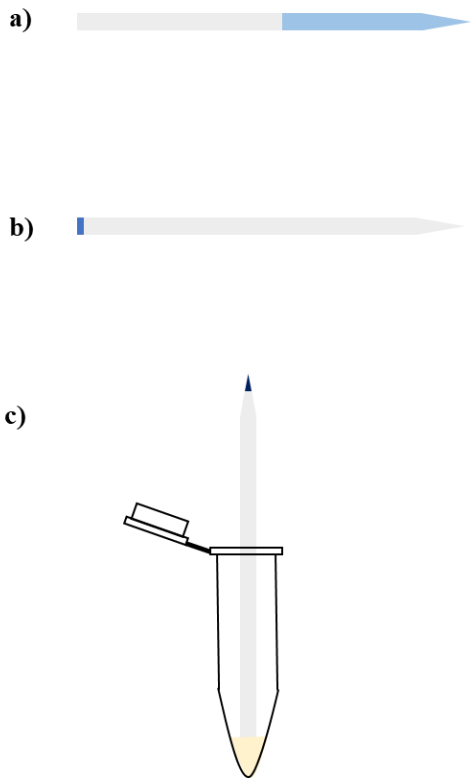

Scheme 4-2. The schematic representation of the preconcentration process using a filamented glass emitter. a) loading of 10 µL sample solution into the glass emitter. b) complete drying of the solvent. c) Dip the end of glass emitter into a 1.5-mL centrifuge vial containing 100 µL extraction solvent.

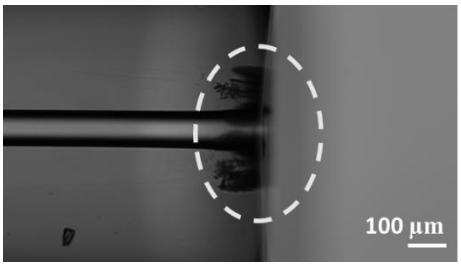

Figure 4-10. Photograph of the deposition of solutes at the end of a glass emitter. The solution used is 0.2 g/L methyl red in water.

The study by Wong et al. can help solve this issue. They demonstrated that applying heat to a paper-based device can efficiently concentrate analytes of interest from biological fluids for downstream detection. In their study, they heated the distal 1 cm of an 80 × 5 × 0.8 mm strip of chromatography paper to 220 °C, resulting in a 20-fold concentration in just 20 minutes. [22] So, we constructed a home-made heating device that could relocate the deposition site of the solute to the middle of the fluid flow pathway, as depicted in **Figure 4-11**. The evaporation rate at the heated place was the maximum so that the analytes would deposte at a specific place. The heating device was composed of a ceramic element with a resistance of ~800 Ω and two aluminum plates, which were assembled using transparent acrylic material. A solution of 80 μM naphthol blue black dye in methanol was loaded into a glass emitter, which was then inserted into the heating device. By applying 30 volts to the heater, the surface temperature reached 50-60 ˚C, at which point the solvent evaporated faster than other positions along the solvent flow pathway. After the solvent was completely evpoarted, the solutes were deposited at approximately 13 mm from the emitter's end, which can prevent the solutes from diffusing during the subsequent dip-and-go reconstitution.

To evaluate the efficacy of our preconcentration method, ESI-MS analysis was performed on the naphthol blue black dye solution. A concentration of 0.8 μM naphthol blue black dye in methanol was used for the ESI-MS analysis. As shown in **Figure 4-12a**, the doubly charged ion at *m/z* 285, which corresponds to the blue dye, was not detected. However, following the preconcentration treatment, as shown in **Figure 4-12b**, a clear peak was detected at m/z 285, demonstrating the efficacy of the preconcentration effect in the ESI-MS analysis. This finding highlights the potential application of our preconcentration method in the field of ESI-MS analysis, which could enable the analysis of low-concentration samples with improved sensitivity and

selectivity. Future studies could explore the application of this preconcentration method to other analytes and optimize the preconcentration conditions for different types of analytes.

One could argured that the preconcentration method suffers severe matrix effects, as all the non-volatile species would be enriched. This enrichment could be harmful for electrospray ionization of analyte due to the increaesd competetion for surface charges based on the ion evaporation model,and difficuties to access the droplet surface.[24] Moverover, in practice, dillution of complex sample by a factor of 25-40 folds can reduce ion suppression from 80% to 20% as demonstrated in Stahnke et al.' study [23].However, our study implies that, despite the potential effect of ion suppression, the absolute signal of analytes was still boosted.

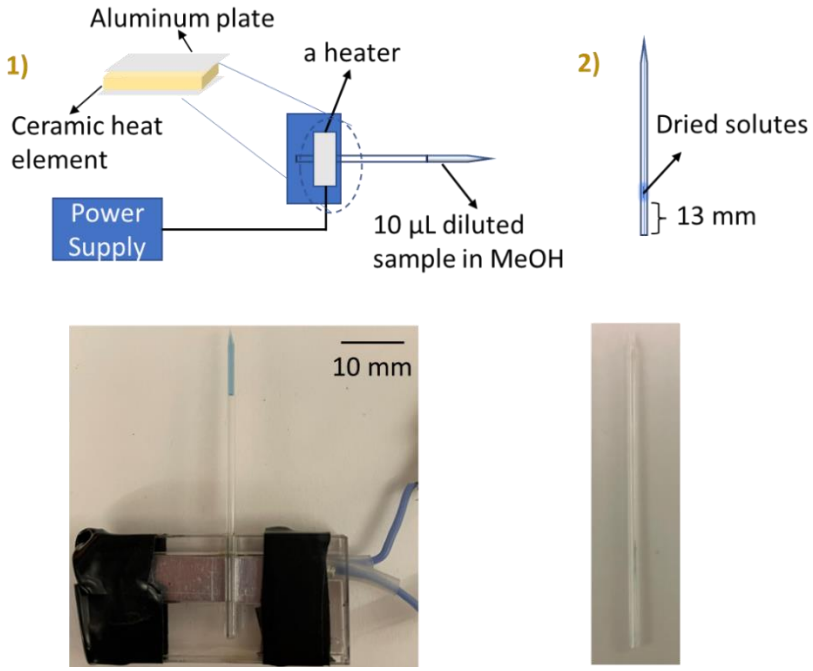

Figure 4-11. A heating device to relocate the deposition of solutes.

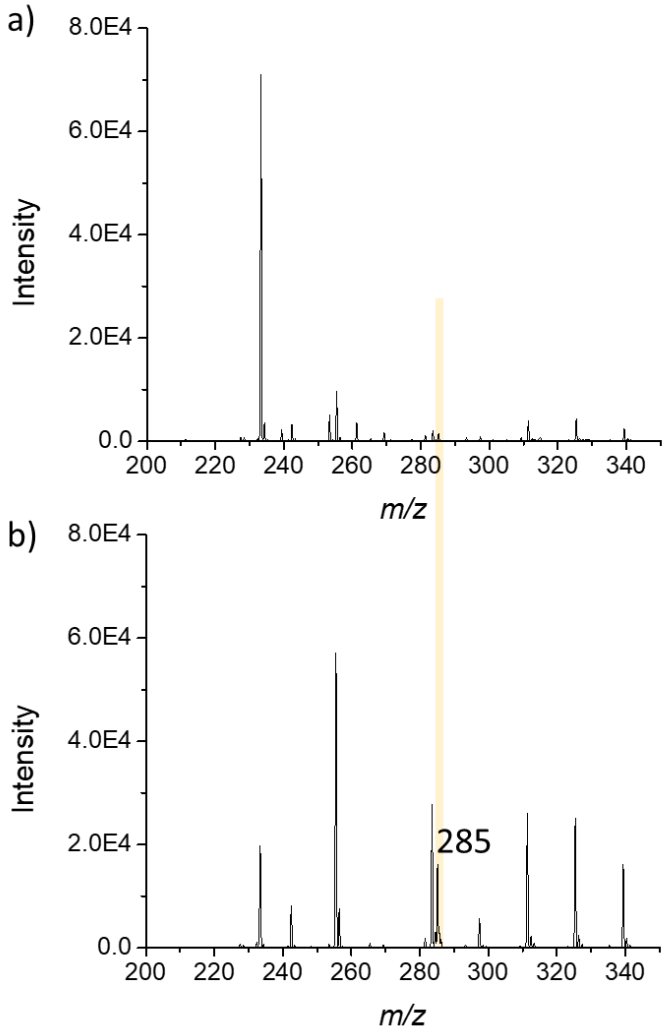

Figure 4-12. Full mass spectra of 0.8 µM naphthol blue black dye in methanol a) before preconcentration and b) after preconcentration, using non-contact ESI-MS analysis. Nanoliter volume sample is loaded into tapper emitter via capillary action. The double charged ion at *m/z* 285 corresponds to naphthol blue black dye. The mass spectra are an average of 80 scans. (2 min)

4.4 Conclusions

This study highlights the potential of a filamented glass emitter as a nanoliter sampling device for preconcentration treatment. The annealed subchannels facilitate fluid flow via capillary action and accumulation at the tapered region, with an estimated volume of 152 ± 42 nL stored in the subchannels. The volume accumulated at the tip is affected by the emitter's orientation during backfilling, which makes it an adjustable nanoliter-level solvent sampling tool. The outward flow induced by evaporation through the grooved subchannels enables the construction of a preconcentration setup. A homemade heater allowed for the relocation of solute deposition and increased robustness. Both direct visualization of DCF under microscopy and ESI-MS analysis of naphthol blue black confirm the method can bring the concentration above the detection limits. Unlike other reported methods utilizing glass emitters, this approach offers a disposable, simple, and low-cost platform for generic enrichment method to reduce the sample size from microliter to nanoliter and avoid the clogging issues.

4.5 References

(1) Feider, C. L.; Krieger, A.; DeHoog, R. J.; Eberlin, L. S. Ambient Ionization Mass Spectrometry: Recent Developments and Applications. *Anal Chem* **2019**, *91* (7), 4266–4290. https://doi.org/10.1021/acs.analchem.9b00807.

(2) Lu, H.; Zhang, H.; Chingin, K.; Xiong, J.; Fang, X.; Chen, H. Ambient Mass Spectrometry for Food Science and Industry. *TrAC Trends in Analytical Chemistry* **2018**, *107*, 99–115. https://doi.org/10.1016/j.trac.2018.07.017.

(3) Chen, C.-H.; Lin, Z.; Tian, R.; Shi, R.; Cooks, R. G.; Ouyang, Z. Real-Time Sample Analysis Using a Sampling Probe and Miniature Mass Spectrometer. *Anal. Chem.* **2015**, *87* (17), 8867–8873. https://doi.org/10.1021/acs.analchem.5b01943.

(4) Hecht, M.; Evard, H.; Takkis, K.; Veigure, R. T.; Aro, R.; Lohmus, R.; Herodes, K.; Leito, I.; Kipper, K. Sponge Spray-Reaching New Dimensions of Direct Sampling and Analysis by MS. *Anal Chem* **2017**, *89* (21), 11592–11597. https://doi.org/10.1021/acs.analchem.7b02957.

(5) Green, F. M.; Salter, T. L.; Stokes, P.; Gilmore, I. S.; O'Connor, G. Ambient Mass Spectrometry: Advances and Applications in Forensics. *Surface and Interface Analysis* **2010**, *42* (5), 347–357. https://doi.org/10.1002/sia.3131.

(6) Ren, Y.; McLuckey, M. N.; Liu, J.; Ouyang, Z. Direct Mass Spectrometry Analysis of Biofluid Samples Using Slug-Flow Microextraction Nano-Electrospray Ionization. *Angewandte Chemie International Edition* **2014**, *53* (51), 14124–14127. https://doi.org/10.1002/anie.201408338.

(7) Ren, Y.; Zhang, W.; Lin, Z.; Bushman, L. R.; Anderson, P. L.; Ouyang, Z. In-Capillary Microextraction for Direct Mass Spectrometry Analysis of Biological Samples. *Talanta* **2018**, *189*, 451–457. https://doi.org/10.1016/j.talanta.2018.07.027.

(8) Zhang, W.; Chiang, S.; Li, Z.; Chen, Q.; Xia, Y.; Ouyang, Z. A Polymer Coating Transfer Enrichment Method for Direct Mass Spectrometry Analysis of Lipids in Biofluid Samples. *Angewandte Chemie International Edition* **2019**, *58* (18), 6064–6069. https://doi.org/10.1002/anie.201900011.

(9) Liu, Q.; Ahmed, E.; Kabir, K. M. M.; Huang, X.; Xiao, D.; Fletcher, J.; Donald, W. A. Pulsed Nanoelectrospray Ionization Boosts Ion Signal in Whole Protein Mass Spectrometry. *Applied Sciences* **2021**, *11* (22), 10883. https://doi.org/10.3390/app112210883.

(10) Huang, G.; Li, G.; Cooks, R. G. Induced Nanoelectrospray Ionization for Matrix-Tolerant and High-Throughput Mass Spectrometry. *Angew Chem Int Ed Engl* **2011**, *50* (42), 9907–9910. https://doi.org/10.1002/anie.201103687.

(11) Wei, Z.; Han, S.; Gong, X.; Zhao, Y.; Yang, C.; Zhang, S.; Zhang, X. Rapid Removal of Matrices from Small-Volume Samples by Step-Voltage Nanoelectrospray. *Angewandte Chemie International Edition* **2013**, *52* (42), 11025–11028. https://doi.org/10.1002/anie.201302870.

(12) Wang, Q.; Zhong, H.; Zheng, Y.; Zhang, S.; Liu, X.; Zhang, X.; Zhang, X.; Zhang, Z. Analyte Migration Electrospray Ionization for Rapid Analysis of Complex Samples with Small Volume Using Mass Spectrometry. *Analyst* **2014**, *139* (22), 5678–5681. https://doi.org/10.1039/C4AN01397B.

(13) Yuill, E. M.; Baker, L. A. Ion Concentration in Micro and Nanoscale Electrospray Emitters. *Anal Bioanal Chem* **2018**, *410* (16), 3639–3648. https://doi.org/10.1007/s00216-018-1043-5.

(14) Walker, G. M.; Beebe, D. J. An Evaporation-Based Microfluidic Sample Concentration Method. *Lab Chip* **2002**, *2* (2), 57. https://doi.org/10.1039/b202473j.

(15) Li, M.; Li, H.; Allen, N. R.; Wang, T.; Li, L.; Schwartz, J.; Li, A. Nested-Channel for on-Demand Alternation between Electrospray Ionization Regimes. *Chem. Sci.* **2021**, *12* (5), 1907–1914. https://doi.org/10.1039/D0SC06221A.

(16) Oesterle, A. *What is "Filamented" Glass & Who Needs It?* www.sutter.com. https://www.sutter.com/MICROPIPETTE/glass.html (accessed 2023-03-01).

(17) Hsieh, C.-H.; Chang, C.-H.; Urban, P. L.; Chen, Y.-C. Capillary Action-Supported Contactless Atmospheric Pressure Ionization for the Combined Sampling and Mass Spectrometric Analysis of Biomolecules. *Anal. Chem.* **2011**, *83* (8), 2866–2869. https://doi.org/10.1021/ac200479s.

(18) Deegan, R. D.; Bakajin, O.; Dupont, T. F.; Huber, G.; Nagel, S. R.; Witten, T. A. Capillary Flow as the Cause of Ring Stains from Dried Liquid Drops. *Nature* **1997**, *389* (6653), 827–829. https://doi.org/10.1038/39827.

(19) Wang, W.; Yin, Y.; Tan, Z.; Liu, J. Coffee-Ring Effect-Based Simultaneous SERS Substrate Fabrication and Analyte Enrichment for Trace Analysis. *Nanoscale* **2014**, *6* (16), 9588–9593. https://doi.org/10.1039/C4NR03198A.

(20) Halvorson, R. A.; Leng, W.; Vikesland, P. J. Differentiation of Microcystin, Nodularin, and Their Component Amino Acids by Drop-Coating Deposition Raman Spectroscopy. *Anal. Chem.* **2011**, *83* (24), 9273–9280. https://doi.org/10.1021/ac201617g.

(21) Kočišová, E.; Procházka, M.; Vaculčiaková, L. Drop-Coating Deposition Raman (DCDR) Spectroscopy as a Tool for Membrane Interaction Studies: Liposome–Porphyrin Complex. *Appl Spectrosc* **2015**, *69* (8), 939–945. https://doi.org/10.1366/14-07836.

(22) Wong, S. Y.; Cabodi, M.; Rolland, J.; Klapperich, C. M. Evaporative Concentration on a Paper-Based Device to Concentrate Analytes in a Biological Fluid. *Anal. Chem.* **2014**, *86* (24), 11981–11985. https://doi.org/10.1021/ac503751a.

(23) Stahnke, H.; Kittlaus, S.; Kempe, G.; Alder, L. Reduction of Matrix Effects in Liquid Chromatography–Electrospray Ionization–Mass Spectrometry by Dilution of the Sample Extracts: How Much Dilution Is Needed? *Anal. Chem.* **2012**, *84* (3), 1474–1482. https://doi.org/10.1021/ac202661j.

(24) Furey, A.; Moriarty, M.; Bane, V.; Kinsella, B.; Lehane, M. Ion Suppression; A Critical Review on Causes, Evaluation, Prevention and Applications. Talanta 2013, 115, 104–122. https://doi.org/10.1016/j.talanta.2013.03.048.

5 Electrochemical Oxidation of Dihydroethidium in Electrospray

5.1 Introduction

Dihydroethidium (5-ethyl-5,6-dihydro-6-phenyl-3,8-diaminophenanthridine, DHE) is a uncharged reactive fluoresence compound that can easily cross biological membranes, [1] making it a commonly used fluoresence probe for detecting superoxide in various biological systems, including intracellular organelles and live animals. [2-3] DHE is a versatile redox probe that can undergo both one electron and two-electron oxidations.[3] When DHE reacts with superoxide, it initially forms a free radical and undergoes one-electron oxidation, resulting in the formation of 2-hydroxyethidium (2-OH-E^+), ethidium (E^+) and dimeric products. For example, the one-electron oxidant ferricytochrome c can induce DHE to form dimeric products,[4] while two-electron oxidation pathway yields E^+, as shown in **Figure 5-1.**

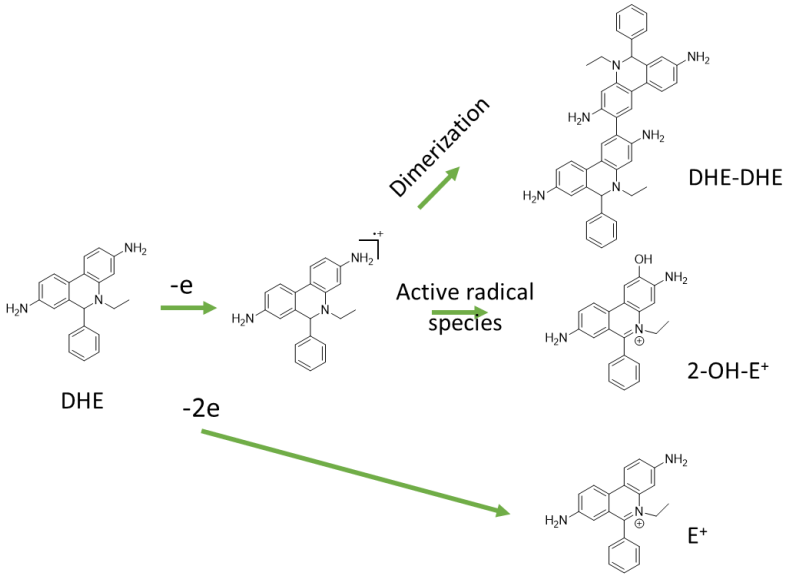

Figure 5-1. Oxidative pathways of DHE

Despite the wide utilization of DHE, there are still debates surrounding the formation of its oxidative products with superoxide. Initially, E^+ was believed to be the major oxidative product of DHE and reactive oxygen species (ROS). However, in 2003, Zhao et al. reported the formation of

a different product, oxy-ethidium, when using DHE to detect intracellular superoxide anions like O_2^- *in vitro*.[5] This observation was supported by Kalyanaraman's study. [6] While, Hall et al. [7] reported that E^+ was the major product of the DHE reaction with O_2^- under *in vivo* conditions with low oxygen levels, contradicting the findings of Zhao et al. in 2003. Later Michalski et al. [3] confirmed that 2-OH-E^+ was the only product formed when using DHE to a wide concentration range of O_2^-.

The study of DHE with ROS in biological systems has yielded varying results, highlighting the need for a reliable method to differentiate oxidative products rapidly and sensitively. While optical methods, such as fluoresence microscopy, have been commonly used, the overlapping fluoresence spectra of oxyethidium and ethidium have led to questions about their reliability. [8-9] As a result, researchers have turned their attention to HPLC (high performance liquid chromatography) assay, which can effectively separate these species on a reversed phase column,[10-11] as well as LC-MS (liquid-chromatograph coupled with mass spectrometry) method that use MRM (multiple reaction monitoring) to distinguish the co-eluting peaks.[8]

The ability of ESI-MS to probe reactive intermediates [12-17] has drawn our attention to developing a more rapid, sensitive, and specific real time detection of oxidative products of DHE with ROS under different biological conditions. The prerequisite for building the ESI-MS based method is to understand the oxidation behavior of DHE in electrospray process, particularly as certain substances, such as metal electrode (Ag and Cu), [18] peptides,[19-21] and drugs, [22] with low oxidation potentials (<1 V vs. SCE) ,[23-24] can undergo electrooxidation at the metal-liquid interface with a positive voltage is applied. [23, 25] To this end, our study aimed to guide the analysis of DHE probe using ESI-based mass spectrometry by investigating the oxidation products in the

electrospray process, as this technique can produce artifacts specific to this fluorescence probe, as well as provide a good guidance to other fluorogenic probes.

5.2 Experimental

5.2.1 Chemicals

Methanol (HPLC grade), acetonitrile (HPLC grade), water (HPLC grade) and formic acid (LC-MS grade) were purchased from Fisher Scientific (Hampton, NH, USA). Sodium sulfate (Na_2SO_4) and sodium periodate ($NaIO_4$) were obtained from Acros Organics (Thermo Fisher Scientific, NJ, USA). Silver nitrate ($AgNO_3$) was purchased from Alfa Aesar (Haverhill, MA, USA). Platinum wire was also obtained from Alfa Aesar (Haverhill, MA, USA) and used as electrode in nanoESI. Dihydroethidium (DHE) and ethidium bromide were purchased from Sigma-Aldrich (St. Louis, Mo, USA).

5.2.2 Real-time electrochemical oxidation of DHE in nanoESI

10 μM DHE solutions dissolved in acetonitrile containing 1% formic acid were transferred into nanoESI emitter. Formic acid was added to ensure the protonation of DHE and thus improve the ionization efficiency. Silver wire was used as electrode with a spray voltage of 2.5 kV in positive ion mode. The products were studied by continuously spraying the sample solution within 3 min. The parameters of the setup are shown in **Figure 5-2**.

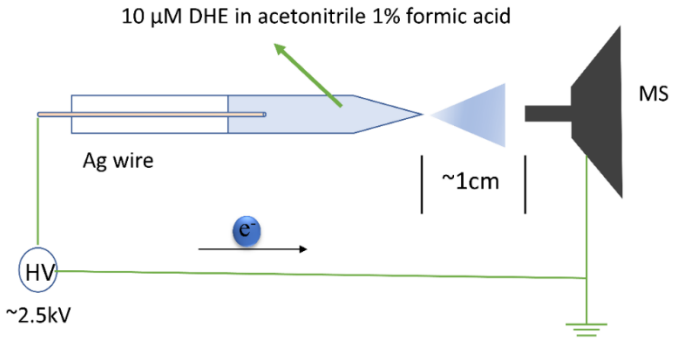

Figure 5-2. Setup of the real-time electrochemical oxidation of DHE. The borosilicate glass capillary with filament (Sutter Instrument, USA) was used with O.D.=1.5 mm and I.D. = 0.86 mm. The distance of Ag electrode away from the capillary tip was ~ 0.2 cm. 10 µL sample was transferred into the capillary, and the distance of sample liquid level to the capillary tip was about 1.5 cm. The distance between the capillary tip and MS inlet was kept at 0.5 cm. The diameter of Ag electrode is 0.25 mm. The emitter tip was about 3.5 um.

5.2.3 Ion soft-landing driven oxidation of DHE.

The schematic of ion soft-landing driven oxidation of DHE was shown in **Figure 5-3**. A high voltage (model PS350, SRS Stanford research systems) was connected to the Pt wire. For safety considerations and to avoid shocking, a high resistor 100 M Ohm was connected in the circuit. The same emitter as **5.2.2** was used in the setup. 50% MeOH/water was the spray solvent. The landing surface was an Indium-Tin-Oxide (ITO) slide with low resistance that could work as electrochemical half-cell, and about 5 µL 30 µM DHE in 50% MeOH/water was drop-casted on the slide. The surface was grounded. A negative voltage 1.5 kV was applied to the emitter, making the slide an anode where oxidation happened. a flux of 0.96-1.9 $\mu A \cdot cm^{-2}$ were landed in a ~3 mm circle where sample. After desired spraying time, the sample droplet was extracted with 10 µL acetonitrile (1% formic acid) three times for further analysis.

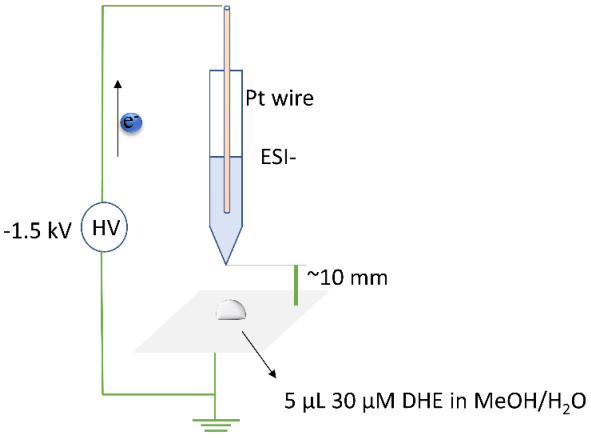

Figure 5-3. A simplified schematic of ion soft-landing driven oxidation of DHE. Pt wire was inserted in glass emitter containing 50% methanol/water (v/v). 1.5 kV spray voltage was applied to glass emitter. Platinum wire is used in this study because it is inert. a drop (~5 µl) containing 100 ppm DHE in methanol/water. The distance between the emitter tip and ITO was around 10 mm.

5.2.4 Oxidation of DHE using silver nitrate

$AgNO_3$ solutions with various concentrations (10 μM, 50 μM, 75 μM, 100 μM, 125 μM, 150 μM, 180 μM, 200 μM, 400 μM, 600 μM, and 800 μM) were mixed with 100 μM DHE in methanol/water (v/v: 1:1) separately. Note that DHE and $AgNO_3$ solutions were prepared freshly. The reactions of various $AgNO_3$/DHE mixtures were performed in 1.5 mL centrifuge tube (Eppendorf, Enfield, CT) at room temperature for 10 min. A control without adding $AgNO_3$ was performed to monitor the autooxidation of DHE in the solution system. Prior to nanoESI mass spectrometric analysis, the samples were diluted by a factor of 10 with acetonitrile containing 1% formic acid.

5.2.5 Mass spectrometry

An LTQ-Orbitrap Velos mass spectrometer (San Jose, CA, USA) was used to analyze samples in the full mass spectrum mode. DHE contains basic amine groups and is prone to be protonated and analyzed in positive ion mode. Moreover, potential oxidation products are also expected to be protonated in positive mode due to their similar backbone structures. Therefore, all the samples were analyzed in positive polarity mode in this study. The experimental parameters were set as follows: capillary temp 150 ˚C, full MS range: 100-600 Th; maximum ion injection time: 100 ms, microscan time: 3 μs, spray voltage: 1.5 kV unless otherwise stated; and mass resolution: 70,000. The mass spectra were recorded in 0.2 min. The Xcalibur software (Thermo Scientific, version 4.0) was used to control the MS system and data acquisition.

5.2.6 Data process

Previous studies show that oxidation products of DHE (M.W.: 315 Da) includes E^+ (M.W.: 314 Da), DHE-DHE (M.W.: 628 Da), DHE-E^+ (M.W.: 626 Da), and E^+-E^+ (M.W.: 624 Da). The doubly charged dimeric species could overlap with the ^{13}C isotopic peak of monomers, leading to

an inaccurate signal intensity. To correct for this, the theoretical isotopic distribution was utilized to adjust the signal intensity for each observed species. For example, the theoretical isotopic peak ratio of the doubly charged dimer DHE-E^+ *m/z* 314.6 to *m/z* 314.1 is 45.4%. Therefore, the 2.2-fold of the isotopic peak at *m/z* 314.6 was used to represent the signal intensity of dimer DHE-E^+, The signal intensity for E^+ was obtained by subtracting the 2.2-fold intensity of *m/z* 314.6 from the signal intensity of peak at *m/z* 314.1, taking into consideration the overlap between DHE-E^+ (*m/z* 314.1) and E^+ (*m/z* 314.1).

$$I(E^+) = \frac{I_{m/z314.1} - 2.2I_{m/z314.6}}{I_{m/z313.1} + I_{m/z314.1} + 2.2I_{m/z315.6} + I_{m/z316.1}}$$

$$I(DHE - DHE) = \frac{2.2I_{m/z315.6}}{I_{m/z313.1} + I_{m/z314.1} + 2.2I_{m/z315.6} + I_{m/z316.1}}$$

$$I(E^+ - E^+) = \frac{I_{m/z313.1}}{I_{m/z313.1} + I_{m/z314.1} + 2.2I_{m/z315.6} + I_{m/z316.1}}$$

$$I(E^+ - DHE) = \frac{2.2I_{m/z314.6}}{I_{m/z313.1} + I_{m/z314.1} + 2.2I_{m/z315.6} + I_{m/z316.1}}$$

5.3 Results and discussions

The extracted ion chronogram (EIC) of *m/z* 316.1 from 10 μM DHE in acetonitrile (1% formic acid) was presented in **Figure 5-4**, the relative standard deviation of the signal intensity of ion at *m/z* 316, which corresponds to DHE, was found to be 5.8% within 40 scans. No obvious oxidative products were observed, except for a few ions at *m/z* 314.1, even at 0.01 min. These ions are likely to be impurities in the standards, as DHE is synthesized by the reduction of ethidium. As a result, nanoESI-MS could screen oxidation products of DHE when the analysis time is less than 0.28 min. Under this condition, the oxidation resulted from ESI mass analysis showed negligible effect on our study and could be ignored.

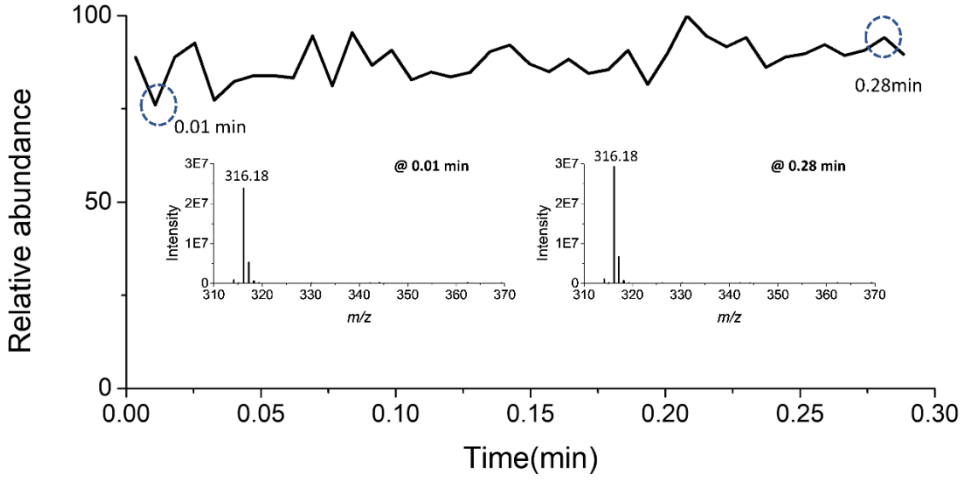

Figure 5-4. Extracted ion chronogram (EIC) of ion at *m/z* 316 corresponding to protonated DHE $[M+H]^+$. The inserted figure showed the mass spectra of DHE at 0.01 min and 0.28 min. To make sure the mass spectra obtained could reveal the actual changes of DHE, not from inherent in-source oxidations.

5.3.1 Realtime screening of DHE electrooxidation products in nanoESI platform

Nano-electrospray ionization mass spectrometry could be utilized to screen electrooxidation reactions because it is also considered as a controlled-current electrochemical cell, where redox chemistry could occur at the solvent/metal electrode interface.[26] Meanwhile, mass spectrometry is capable to provide qualitative and quantitative information on chemical substances.[27] Herein, the electrooxidation of DHE was studied for the first time in nanoESI. As shown in **Figure 5-5**, after applying DC voltage for 2.5 min, the relative signal intensity (%) of DHE at *m/z* 316 obtained from the10 μM DHE solution varied in range of 51% to 61% during 0.7 min, which is likely due to the fluctuations of home-made nanoESI source and oxidation of a small amount of DHE stock solution, because there were no significant changes in the full mass scan patterns within this period. Then the relative signal intensity of DHE decreased from 58% to 10% quickly within 0.4 min, at the same time the relative abundance of oxidative product detected at *m/z* 314 increased significantly from 26% to 57%. The distance between electrode to emitter tip was about 2 mm, and the flow rate was measured to be 140 nL/min. [28] It was assumed that the time delay before appearance of the expected product at *m/z* 314 was approximately equal to the elution time spent from electrode to MS inlet, at which the MS analyzing time (milliseconds, <1 second) was ignorable. As the inner diameter of the emitter taper was 0.86 mm, the average linear flow velocity was calculated to be 0.72 mm/min. As a result, the time delay between DHE oxidized on the electrode and its spraying was estimated to be 2.8 min. The estimated delay time was 4-fold longer (2.8 min) than the time needed to observe DHE conversion (0.7 min), implying that a fast mass transfer occurred in the narrow capillary emitter tip and thus shorten the delay time. [27]

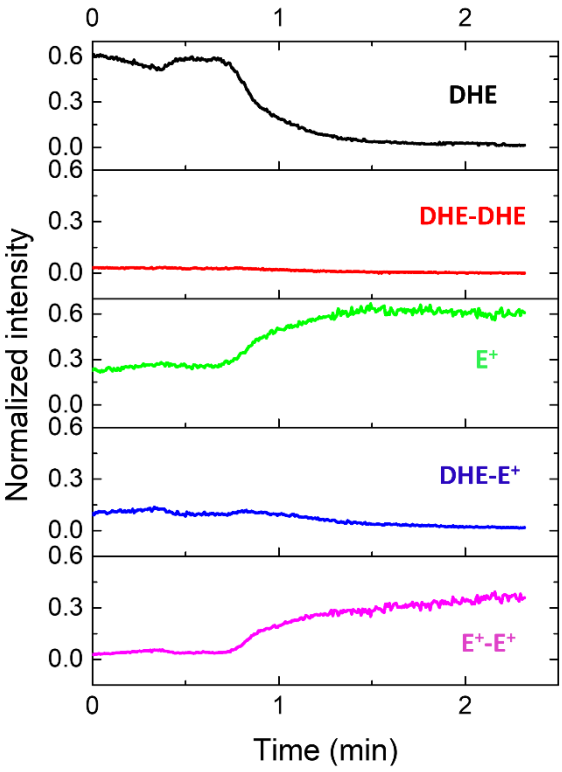

Figure 5-5. *In-situ* monitoring of oxidation of 10 µM DHE in acetonitrile with 0.1% formic acid in conventional nano-ESI setup. The observed oxidative products were normalized by measuring the intensity of specific ion relative to the sum of intensity of species derived from DHE. (Shown in experimental section).

Figure 5-6 shows that at 1.5 min oxidative product detected at *m/z* 314 became the predominant peak along with the disappearance of DHE molecular ion $[M+H]^+$ at *m/z* 316 indicating a rapid conversion of picomole level DHE in this conventional nanoESI setup. The oxidative products were identified based on accurate mass analysis. The elemental composition analysis derived from exact mass (< 5 ppm) indicated that the dominated oxidative species at *m/z* 314.1 was generated from DHE by losing two hydrogens and assigned as E^+, which is in accordance with the reported oxidative product ethidium cation of DHE with the presence of ROS *in vitro* study. A less abundance dimeric oxidative product at *m/z* 313.16 was observed and assigned as E^+-E^+ as the distance between the isotopic peaks (*m/z* 313.16 and *m/z* 313.66) was 0.5 Th and the isotopic abundance 44.3% was close to the theoretical value 45.4%. Likewise, two minor isotopic peaks at *m/z* 314.67 and *m/z* 315.68 demonstrated the presence of two other dimeric species. These observations also agree with previous studies that ethidium cation at *m/z* 314 was a major oxidative product of DHE accompanied with dimers.[1] The elemental composition analysis derived from exact mass (< 5 ppm) showed that the dimer at *m/z* 315.1 was attributed to dimerization between DHE radical (lose one H) and assigned as DHE-DHE, and another dimer at *m/z* 314.1 was assigned as DHE-E^+ and could be obtained from either dimerization between DHE radical and ethidium cation or further oxidation of DHE-DHE dimer. It was also noticed that a larger mass error occurred between calculated *m/z* for DHE-DHE dimer and measured *m/z* was 9.0 ppm, which is due to the overlapping of isotopic peak at *m/z* 315.1685 from ethidium cation of which value is smaller than the doubly charged ion of dimer at m/z 315.1730, lowering the measured value.

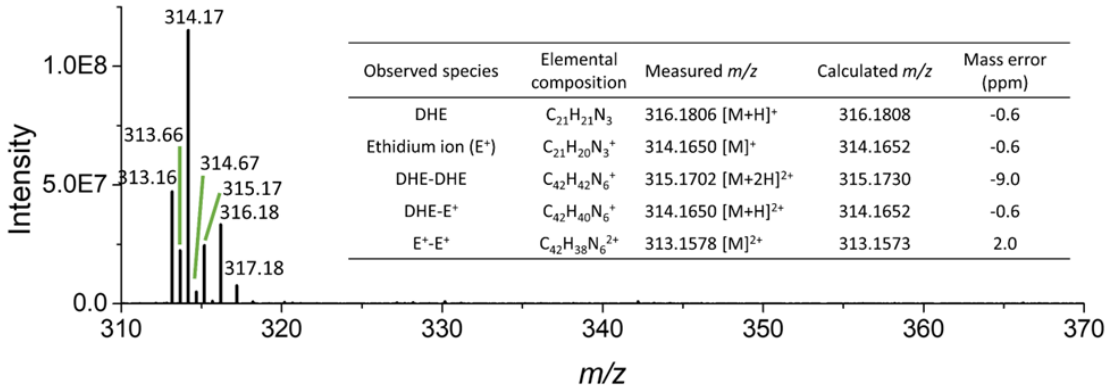

Observed species	Elemental composition	Measured *m/z*	Calculated *m/z*	Mass error (ppm)
DHE	$C_{21}H_{21}N_3$	316.1806 $[M+H]^+$	316.1808	-0.6
Ethidium ion (E^+)	$C_{21}H_{20}N_3^+$	314.1650 $[M]^+$	314.1652	-0.6
DHE-DHE	$C_{42}H_{42}N_6^+$	315.1702 $[M+2H]^{2+}$	315.1730	-9.0
DHE-E^+	$C_{42}H_{40}N_6^+$	314.1650 $[M+H]^{2+}$	314.1652	-0.6
E^+-E^+	$C_{42}H_{38}N_6^{2+}$	313.1578 $[M]^{2+}$	313.1573	2.0

Figure 5-6. Full mass spectra across 0.25 min obtained from *in-situ* monitoring of oxidative process of 10 µM DHE in acetonitrile with 0.1% formic acid with the nanoESI-MS. The inserted table showed the elemental composition analysis based on accurate mass measurements. (Shown in experimental section)

To further investigate the changes of oxidative species in the system, the relative intensity of ions corresponding to oxidative species were monitored. It was shown that the relative intensity of ion at *m/z* 315.6 attributed to the dimeric product DHE-DHE was almost unchanged, indicating DHE-E^+ was formed by DHE radical and ethidium cation. Otherwise, it would expect for the DHE-DHE species to decrease if the dimer DHE-E^+ species was formed by a further oxidation of DHE-DHE. Meanwhile, the dimer DHE-E^+ decreased at 1.0 min, which coincided with the increase of dimer E^+-E^+, implicating that E^+-E^+ was formed by further oxidization of DHE-E^+.

In this setup, we did not observe the specific oxidative product 2-hydroxyethidium (2-OH-E^+) firstly characterized by Zhao and his colleagues, [5] in which they demonstrated that 2-hydroxyethidium rather than E^+ was generated specifically by superoxide $O_2^{-\bullet}$ based on HPLC-fluorescence analysis, while the two-electron oxidized product ethidium was associated mainly with pathways involving hydrogen peroxide H_2O_2, as well as metal-based oxidizing systems such as $Fe(CN)^{3-}_6$ anion, heme Fe(III) of mitochondrial cytochromes C.[5] So, on the other hand if we observed the specific oxyethidium products in the oxidative system, we would expect the presence of superoxide. In addition, the absence of 2-OH-E^+ in this setup suggested the non-existence of peroxide.

5.3.2 Oxyethidium observed in ambient ion soft-landing driven oxidation of DHE

One conclusion drawn from the above observations was that oxidation reactions took place at the electrode/solution interface in positive ion mode. If so, DHE could be oxidized on the counter electrode in the negative ion mode, as would be the oxidative products obtained similar to the conventional nanoESI setup shown in **Figure 5-2**. In this course, ion soft-landing driven oxidation of DHE was studied using setup 2 (**Figure 5-3**). Apply a negative high voltage (-1.5 kV), the indium tin oxide (ITO) slide was acted as the counter anode electrode, where 5 μL DHE at a

concentration of 100 mg/L was drop-casted on and could undergo oxidative reactions. The most relevant difference between the two setups was there was spume (charged fine droplets) hitting on the droplet containing reactants. The process was also referred to ion soft-landing to deposit ions with low kinetic energy (<100 eV) on the desired surfaces. [29]

In the representative mass spectra obtained from setup 2 after 10 min continuous spraying at negative ion mode, the relative abundance of ion at *m/z* 314.6 was 3.4% to the ion at *m/z* 314.1. According to calculated isotopic abundance of dimeric product, the isotope peak at *m/z* 314.6 was expected to be 45.4% of the abundance of the doubly charged dimeric ion at *m/z* 314.1, that means 92% of the peak at *m/z* 314.1 should be contributed to E^+ cation after correcting for the overlapping with dimeric species. As a result, the major oxidative species in setup 2 was E^+ as s well. (**Figure 5-7**).

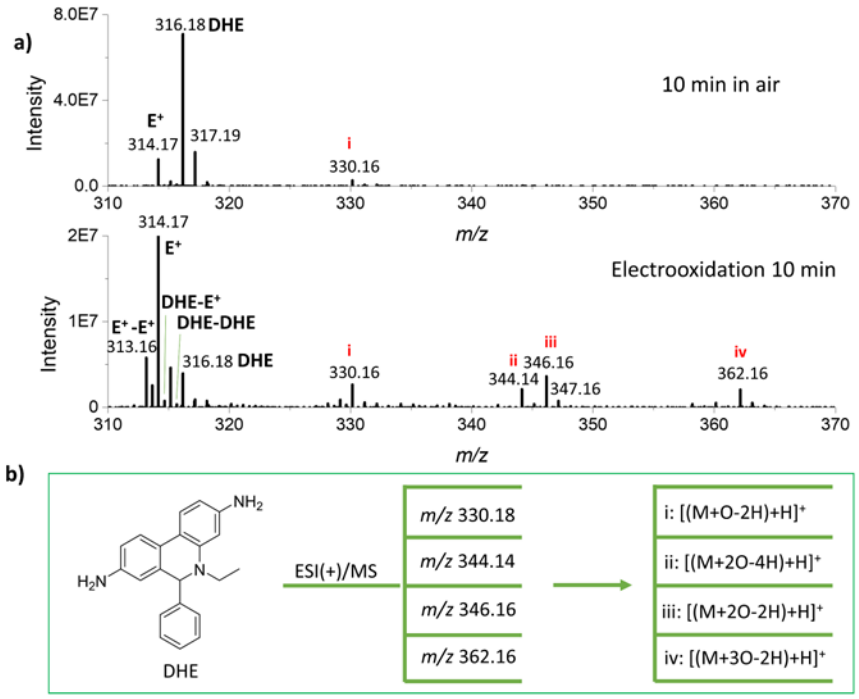

Figure 5-7. a) electrochemical oxidation products of DHE observed using setup 2. To correct for autooxidation of DHE in ambient atmosphere. Full mass spectra of 10 mg/L DHE in solvent (90:5:5, ACN/MeOH/H_2O, v/v/v, with 1% FA) was acquired as well. b) The proposed modifications of new observed species based on accurate mass analysis.

However, the differences between the two setups were also apparent. There were three new species detected at *m/z* 344.1, *m/z* 346.1 and *m/z* 362.1 only observed in setup 2. The high-resolution mass analysis suggested the elemental compositions of three species were $C_{21}H_{18}N_3O_2^+$, $C_{21}H_{20}N_3O_2^+$, and $C_{21}H_{20}N_3O_3^+$, respectively (**Figure 5-7**). The peak at *m/z* 344.1 showed a 14 Th shift, suggesting a pathway of dehydrogenation followed with oxidation occurred on oxyethidium detected at *m/z* 330.1.

The three new species were further confirmed by a comparison with the full-mass spectra acquired from the control sample, which was placed in air for 10 min. As can be seen in **Figure 5-7**, none of them were detectable in the control, ruling out the possibility that the new species were generated through autooxidation of DHE in air. It is safe to ascribe the occurrence of three species (ii-iv, **Figure 5-7**) to the ion landing process. One possible explanation is that collisions between charged droplets and oxygen help produce peroxide $O_2^{-\bullet}$ based on the studies that oxyethidum was specific oxidative product by peroxide. Besides the peroxide $O_2^{-\bullet}$, Lee et al. have demonstrated that H_2O_2 could be produced from microdroplets (<10 μM) by recombination of hydroxyl radial (·OH) [30] Considering the diameter of charged fine droplets generated in nanoESI is at nanometer level, the production of hydrogen peroxide during the process is strongly suggested, which may account for oxyethidium species generation..

5.3.3 Oxidation of DHE with $AgNO_3$

It was reported that ferricyanide $Fe(CN)_6^{3-}$ with a reduction potential of 0.48 V ($Fe(CN)_6^{3-}$ / $Fe(CN)_6^{4-}$ vs. SHE) could oxidize DHE to form E^+, as well as dimeric products. [31-32] Considering $AgNO_3$/Ag has a reduction potential of 0.54 V against NHE, as well as the threshold oxidation potential of DHE was as low as to 0.126 V measured by Wang et al, [33] we presumed that the Ag ions produced in nanoESI could also oxidize DHE. In electrospray process, oxidation occurs not

only on the analyte, but also electrode and solvent. Li et al. showed that metal electrode Ag could be oxidized to form solvated $Ag(ACN)^+$ in nano-electrospray.[18] A question arises: whether Ag ion from Ag electrode could oxidize DHE in nanoESI? To explore the possibility, Ag electrode was used to spray acetonitrile solvent until silver-containing ions at *m/z* 148 and *m/z* 150 appeared (**Figure 5-8**), then setup 2 was used to deposit the plume (silver ions) onto counter electrode for 30 min. Li et al have estimated that around 10 nL silver ions at a concentration of 10 μM could be generated every minute in this process. [18] So we were able to collect 0.3 μL 10 μM silver ions after spraying for 30 min. Then 5 μL DHE at a concentration of 10 μM in MeOH/water was transferred on the slide to mix with deposited Ag ions, followed by incubation in 0.1 mL centrifuge tube for 10 min. The mass analysis showed DHE did not change obviously, and the solvated silver ions were not observed either. The observation indicated that the deposited silver ions could undergo reduction on the counter electrode as cathode when positive voltage is applied.

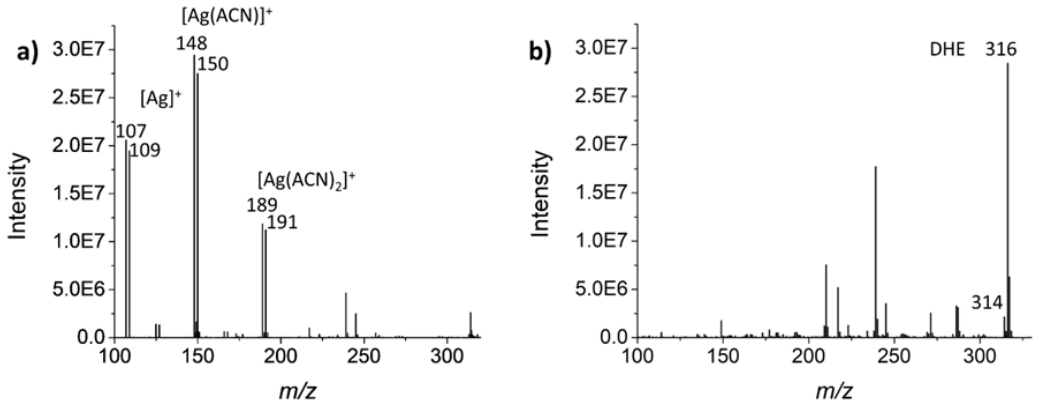

Figure 5-8. a) Mass spectra of solvated silver ion using silver electrode to spray acetonitrile in nano-ESI b) Mass spectra of DHE after reacting with deposited silver species.

To investigate the oxidative ability of Ag^+ ions on DHE, $AgNO_3$ was used. we have incubated 10 μM DHE in solution (50% methanol/water, v/v) containing 100 μM $AgNO_3$ for 10 min. To exclude the possibility that salts could act as catalysts to facilitate the oxidation of dissolved oxygen with DHE, Na_2SO_4 and a common strong oxidizing agent $NaIO_4$ were applied as controls.

Mass spectra were obtained from the mixtures containing DHE and different salts. As can be seen in **Figure 5-9**, with the presence of $AgNO_3$, the peak at *m/z* 316 corresponding to protonated DHE disappeared but peaks detected at *m/z* 313 occurred. When Na_2SO_4 was used as control we observed only minimal oxidation, in which the signal intensity ratio of *m/z* 314 relative to *m/z* 316 was 0.03. For $NaIO_4$, there was a slightly higher oxidative effect on DHE relative to Na_2SO_4, because the signal intensity ratio increased from 0.03 to 0.20, further confirming that Ag^+ was served as an oxidant rather than a catalyst in the oxidation of DHE. Meanwhile the color of solution with presence of Ag^+ turned from colorless to red, showing a great correlation between MS results and color change.

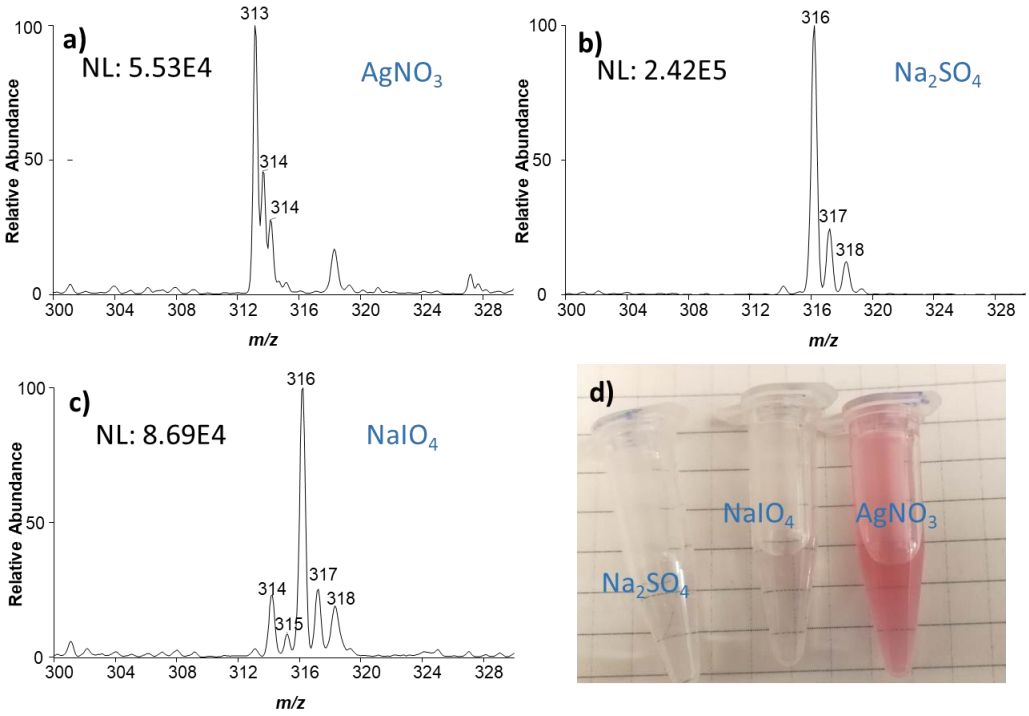

Figure 5-9. Mass spectra of 10-fold diluted sample a) 10µM DHE incubated with 100 µM $AgNO_3$ in 50% MeOH/water for 10 min; b) 10µM DHE incubated with 50 µM Na_2SO_4 in in 50% MeOH/water for 10 min; c) 10µM DHE incubated with 100 µM $NaIO_4$ in in 50% MeOH/water for 10 min. The diluted solution is acetonitrile with 1% formic acid. Mass spectrum is an average of 50 scans. d) Photograph of incubated samples.

This was the first time that DHE has been observed to be oxidized by Ag^+. To gain more insights into Ag^+ oxidation of DHE, the concentration of 100 µM DHE was monitored after incubation with various concentrations of Ag^+ from 0 µM to 800 µM. We observed that the relative signal intensity of DHE decreased linearly with the increase of concentration of $AgNO_3$ to 200 µM with R^2 value 0.92 (**Figure 5-10**). Meanwhile, the addition of $AgNO_3$ at a concentration of 200 µM caused the disappearance of protonated DHE at *m/z* 316.1 (**Figure 5-10**), indicating the average stoichiometry ratio between Ag^+ and DHE was 2:1 although the oxidative species were complex. As it is seen in **Figure 5-10**, the signal intenisty of ion at *m/z* 314.67 corresponding to isotopic peak of dimer DHE-E^+ relative to the most intense peak detected at m/z 314.17 was 30%, indicating the peak at m/z 314.17 was composed of 62% dimer DHE-E^+ and 38% E^+.

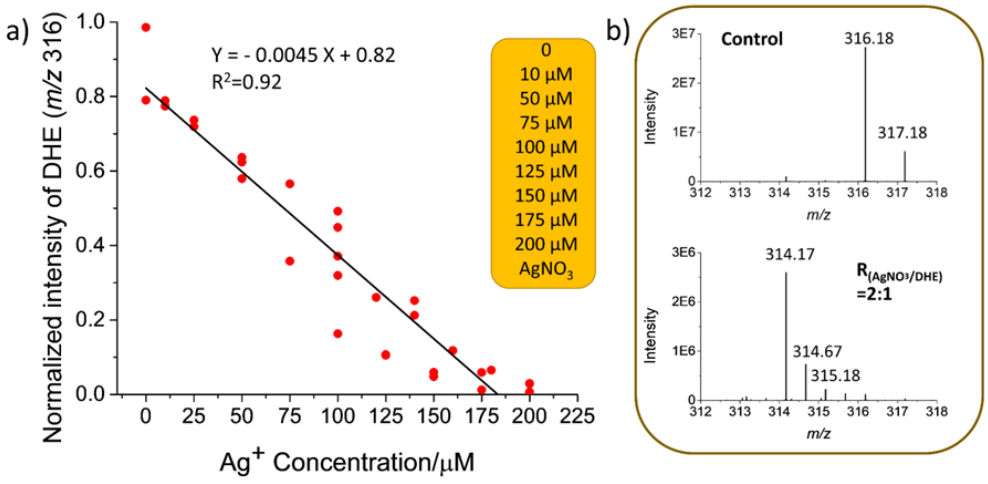

Figure 5-10. a) plot of normalized signal intensity of DHE molecular ion at *m/z* 316 against a series of concentration of Ag+ in range of 0-200 µM. A linear regression analysis showed R^2=0.92. b) Representative mass spectra of control sample without $AgNO_3$ and sample with molar ratio of $AgNO_3$/DHE =2.

Additionaly, as shown in **Figure 5-11**, the relative intensity of dimeric product DHE-DHE increased upon the addition of Ag^+ ion and reached to the highest point with molar ratio of $AgNO_3$/DHE = 1, at which point another dimeric product DHE-E^+ started to increase and reached to the highest when the relative intensity of DHE-DHE decreased to almost 0. This consistency strongly indicated DHE-DHE was further oxidized by Ag^+ to form DHE-E^+. Likewise, the intensity of dimer DHE- E^+ decreased along with increasing of dimer E^+-E^+, implying that Ag^+ could oxidize DHE-E^+ to E^+-E^+. Besides the dimerization oxidative pathway, a relatively small portion of DHE was converted to E^+ (<30%) by losing two electrons. Michalski et. al showed oxidation of DHE with the ferricyanide anion led to the formation of major product E+ and minor HE dimers, and they postulated the mechanism that DHE was oxidized to generate the radical cation, which then decayed by dimerization in the absence of superoxide.[32] Similar oxidation products were observed in Ag^+ oxidative system, however, in Ag^+ oxidation system we found that the major product was DHE-E^+ rather than E^+ when the molar ratio was 2:1. It could be due to that 1) difference of the incubation solvents that Michalski et al have used ACN/phosphate butter (50 mm, pH 7.4), whereas in our study MeOH/water was used. 2) oxidizing agents, even one electron oxidant ferricyanide anion also exhibited 2:1 stoichiometry, that said DHE needs to give out 2 equivalents of electrons. Even the mechanism is unclear, it was shown that dimerization was the major oxidative pathway in the case with Ag^+ as the oxidizing agent, and nanoESI-MS analysis method could differentiate the oxidative products of DHE under different conditions (setup 2 verse $AgNO_3$).

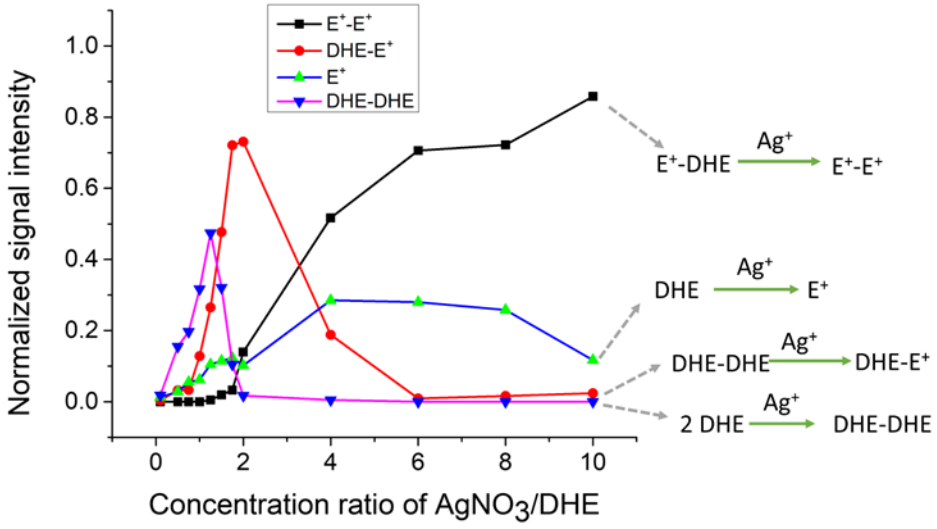

Figure 5-11. Plots of normalized signal intensities of oxidative products against various concentration ratio of $AgNO_3$/DHE

5.3.4 Structural elucidations of oxidative products with tandem MS

As the fragmentation patterns of products would provide detailed structural information, the sites where the modifications undergo on parent compound could be examined by comparing the fragmentations of oxidation products with the parent species. An assumption in the strategy is that the modified products would have common core structures with the parent compound, irrespective of the pathways either through oxidation, reduction, or conjugations. Therefore, the tandem mass spectra of modified compounds and parent compound would present similar characteristic fragments, and the site can be narrowed down to a certain spot based on a corresponding shift in *m/z* value of a characteristic product ion after comparing with that from the parent species.

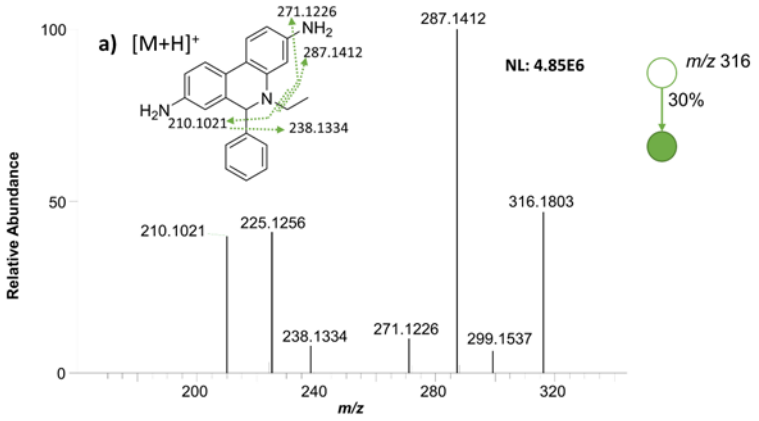

Table b: Predicted Elemental composition of fragmentations of DHE based on exact mass

Product ion	Formula	Monoisotopic mass exp. *m/z*	Monoisotopic mass theo. *m/z*	Mass error ppm
OE cation	$C_{19}H_{17}N_3$	287.1412	287.1417	1.7
EE cation	$C_{19}H_{15}N_2$	271.1226	271.1230	1.5
EE cation	$C_{15}H_{16}N_3$	238.1334	238.1339	2.1
OE cation	$C_{14}H_{15}N_3$	225.1256	225.1260	1.8
EE cation	$C_{13}H_{12}N_3$	210.1021	210.1026	2.4

Figure 5-12. a) Tandem mass spectra of ethidium ion $[M]^+$ at *m/z* 314 in positive mode (NCE: 40%). The concentration was 1 µM. The isolation window was set to 1.0. b) Table of elemental analysis

Consequently, the 2 Th shift of ethidium ion relative to that of DHE would expect to be observed in tandem mass spectra as well. The MS^2 spectra of protonated DHE and ethidium ion were acquired from 10 mg/L standard solution in acetonitrile with 1% formic acid, respectively. As can be seen in **Figure 5-12**, the nanoESI-MS/MS spectra of $[M+H]^+$ ion (*m/z* 316.1) of DHE presented abundant product radical ion at *m/z* 287.1412 through a homolytic cleavage between C-N bond, which is further confirmed by element composition analysis (mass error < 5 ppm) in **Figure 5-12**. It rarely occurs to form radicals with an odd number electron from an even-electron cation because the process is usually highly endothermic and thus improbable. The unpaired electron on radical cations may be stabilized by the conjugated π system. Another abundant product ion at *m/z* 271.1226 was generated by neutral loss of CH_2CH_2 group and NH_3 group. A neutral loss of phenyl group C_6H_6 yielded product ion at *m/z* 238.1334, and additional of a neutral loss of CH_2CH_2 group gave another product ion *m/z* 210.1021. The mass accuracy of elemental composition for the proposed fragments was less than 5 ppm, as shown in Table b.

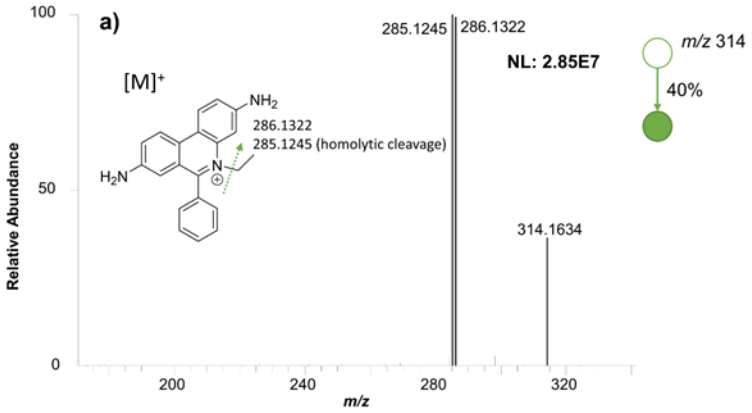

Table b: Elemental composition of fragmentations of ethidium cation based on exact mass

Product ion	Formula	Monoisotopic mass exp. *m/z*	Monoisotopic mass theo. *m/z*	Mass error ppm
EE cation	$C_{19}H_{16}N_3$	286.1322	286.1339	5.9
OE cation	$C_{19}H_{15}N_3$	285.1245	285.1260	5.3

Figure 5-13. a) Tandem mass spectra of protonated DHE $[M+H]^+$ at *m/z* 316 in positive mode (NCE: 30%). The concentration was 1 µM. The isolation window was set to 1.0. b) elemental analysis of product ions

The ethidium ion at *m/z* 314 gave only two intense peaks at *m/z* 285.1244 and *m/z* 286.1322 in tandem mass analysis (**Figure 5-13**). The mass difference between fragment ion at *m/z* 286.1322 and the precursor ion (ethidium cation) at *m/z* 314.1634 was 28.0312 Th, which corresponded to a neutral loss of CH_2CH_2 group (28.0308 amu, mass error 14 ppm). The elemental composition data showed the fragment at *m/z* 285.1244 was a radical cation by the loss of CH_3CH_2• through a homolytic cleavage of C-N bonding. Additionally, the almost equal mass spectral intensities of two fragments indicated the radical cation was stable in gas phase although in the view of classical chemistry even-electron fragment is more stable. The significant different fragmentation patterns between ethidium ion and DHE indicates the change of core structures and thus disable us to apply tandem mass spectra to narrow down the reaction sites, otherwise, the same fragmentation pattern would expect to be observed.

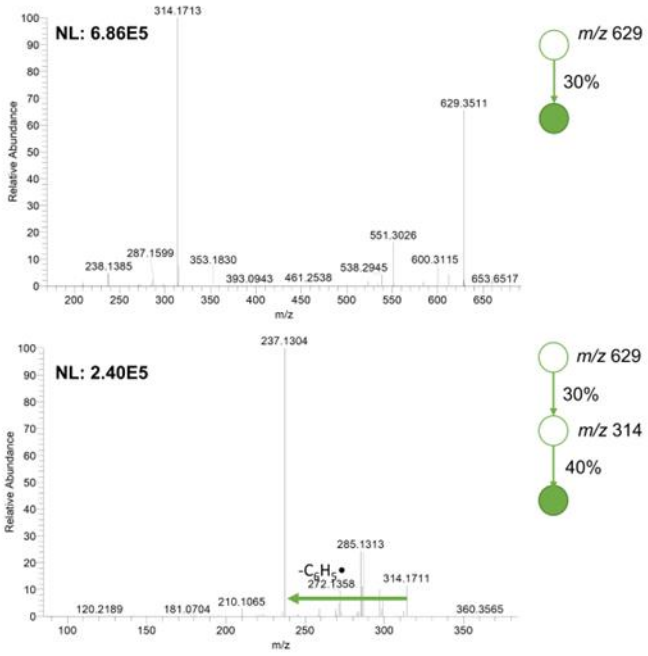

Figure 5-14.Tandem mass spectra of dimer DHE-DHE

In spite of monomeric oxidative product E^+, the tandem mass spectra of dimers were also acquired. As can be seen in **Figure 5-14**, the MS^2 spectrum of protonated dimeric species DHE-DHE at *m/z* 629 showed that the most abundant product ion was detected at *m/z* 314, and the MS^3 analysis of product ion at *m/z* 314 revealed that the most intense ion at *m/z* 237 resulted from a loss of phenyl radical. Another protonated dimeric species DHE-E^+ (*m/z* 627) generated abundant product ions at *m/z* 521, which resulted from the neutral losses of CH_2CH_2 group and phenyl group C_6H_6. The MS^3 product ions of precursor ion (*m/z* 521) was observed at *m/z* 492, arising from a loss of CH_2CH_2 group, **Figure 5-15**.

The homodimer E^+-E^+ was confirmed by MS^2 analysis as well (**Figure 5-16**), of which the fragmentation patterns agreed with that reported by Zielonka et al.[34] The most abundant product ions at *m/z* 299.1 was corresponding to the neutral loss of C_2H_4 group.

In summary, the main fragmentation pathways in DHE oxidative products included a loss of either CH_2CH_2 or radical CH_3CH_2• and a loss of either phenyl or radical phenyl. We inferred that the existence of a conjugated π system in DHE makes it difficult to acquire more fragments and dive into the conjugation sites between monomers. So, the tandem MS strategy did not work well in my attempts to narrow down the modifications sites and elucidate the structure.

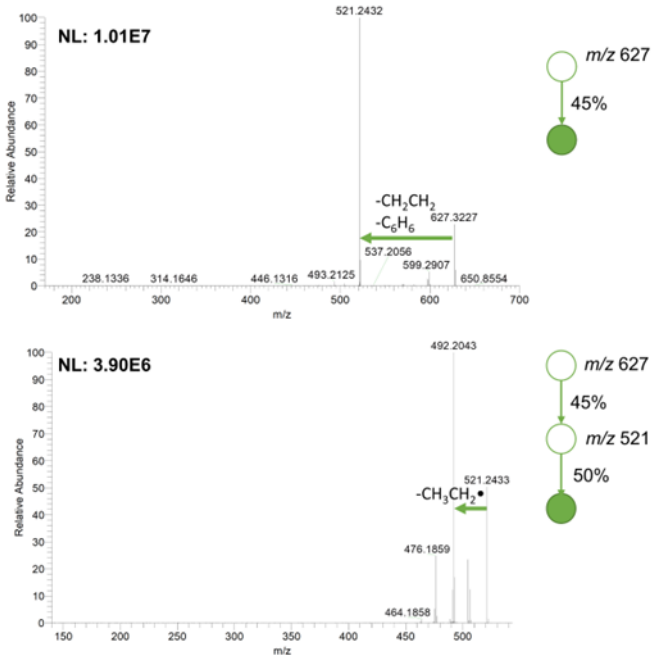

Figure 5-15. Tandem mass spectra of dimer DHE-E^{+}

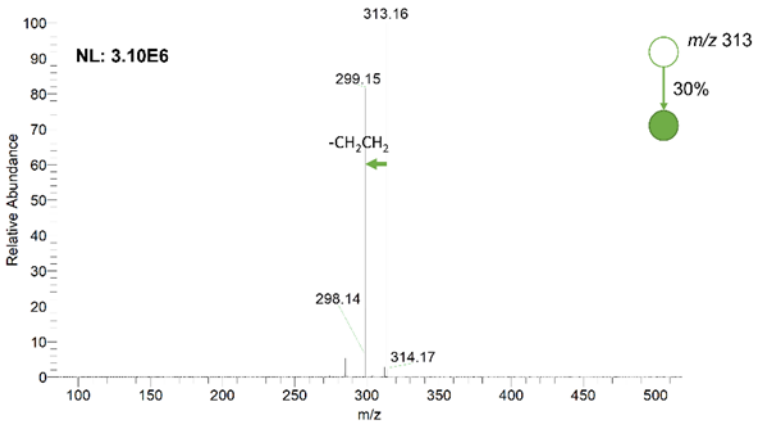

Figure 5-16. Tandem mass spectra of dimer E^{+}-E^{+}

5.4 Conclusions

NanoESI-MS is capable of screening DHE oxidation products when the total electrospray time is less than 0.2 min. After keeping spraying for over a few minutes, both positive nanoESI regular setup and negative soft-landing setup show similar oxidative product profiles, with the exception of oxyethidium products observed in the soft-landing setup, which might result from the charge droplet plume casting process. In addition, the investigation into the oxidative potential of Ag^+ ions to DHE revealed that dimer was the major oxidative product with a stoichiometric ratio of 2:1, and this differed from the oxidation product profile observed in both nanoESI and soft-landing processes. To gain insights into the modification sites on DHE, tandem mass analysis was performed, odd electron fragments were observed in the fragmentation patterns due to the stability of the conjugated π system. The stable core backbone structure of DHE prevented us from obtaining detailed structural information on the oxidation sites.

5.5 References

1. Laurindo, F. R.; Fernandes, D. C.; Santos, C. X., Assessment of superoxide production and NADPH oxidase activity by HPLC analysis of dihydroethidium oxidation products. *Methods in enzymology* **2008,** *441*, 237-60.

2. Chen, J.; Rogers, S. C.; Kavdia, M., Analysis of Kinetics of Dihydroethidium Fluorescence with Superoxide Using Xanthine Oxidase and Hypoxanthine Assay. *Annals of Biomedical Engineering* **2013,** *41* (2), 327-337.

3. Michalski, R.; Michalowski, B.; Sikora, A.; Zielonka, J.; Kalyanaraman, B., On the use of fluorescence lifetime imaging and dihydroethidium to detect superoxide in intact animals and ex vivo tissues: a reassessment. *Free Radic Biol Med* **2014,** *67*, 278-84.

4. Zielonka, J.; Srinivasan, S.; Hardy, M.; Ouari, O.; Lopez, M.; Vasquez-Vivar, J.; Avadhani, N. G.; Kalyanaraman, B., Cytochrome c-mediated oxidation of hydroethidine and mito-hydroethidine in mitochondria: identification of homo- and heterodimers. *Free Radic Biol Med* **2008,** *44* (5), 835-46.

5. Zhao, H.; Kalivendi, S.; Zhang, H.; Joseph, J.; Nithipatikom, K.; Vásquez-Vivar, J.; Kalyanaraman, B., Superoxide reacts with hydroethidine but forms a fluorescent product that is distinctly different from ethidium: potential implications in intracellular fluorescence detection of superoxide. *Free Radical Biology and Medicine* **2003,** *34* (11), 1359-1368.

6. Kalyanaraman, B., Oxidative chemistry of fluorescent dyes: implications in the detection of reactive oxygen and nitrogen species. *Biochemical Society Transactions* **2011,** *39* (5), 1221-1225.

7. Hall, D. J.; Han, S. H.; Chepetan, A.; Inui, E. G.; Rogers, M.; Dugan, L. L., Dynamic optical imaging of metabolic and NADPH oxidase-derived superoxide in live mouse brain using fluorescence lifetime unmixing. *Journal of cerebral blood flow and metabolism : official journal of the International Society of Cerebral Blood Flow and Metabolism* **2012,** *32* (1), 23-32.

8. Xiao, Y.; Meierhofer, D., Are Hydroethidine-Based Probes Reliable for Reactive Oxygen Species Detection? *Antioxidants & Redox Signaling* **2018,** *31* (4), 359-367.

9. Kalyanaraman, B.; Darley-Usmar, V.; Davies, K. J.; Dennery, P. A.; Forman, H. J.; Grisham, M. B.; Mann, G. E.; Moore, K.; Roberts, L. J., 2nd; Ischiropoulos, H., Measuring reactive oxygen and nitrogen species with fluorescent probes: challenges and limitations. *Free Radic Biol Med* **2012,** *52* (1), 1-6.

10. Kalyanaraman, B.; Dranka, B. P.; Hardy, M.; Michalski, R.; Zielonka, J., HPLC-based monitoring of products formed from hydroethidine-based fluorogenic probes--the ultimate approach for intra- and extracellular superoxide detection. *Biochim Biophys Acta* **2014,** *1840* (2), 739-44.

11. Fernandes, D. C.; Gonçalves, R. C.; Laurindo, F. R. M., Measurement of Superoxide Production and NADPH Oxidase Activity by HPLC Analysis of Dihydroethidium Oxidation. In *Hypertension: Methods and Protocols*, Touyz, R. M.; Schiffrin, E. L., Eds. Springer New York: New York, NY, 2017; pp 233-249.

12. Zhu, W.; Yuan, Y.; Zhou, P.; Zeng, L.; Wang, H.; Tang, L.; Guo, B.; Chen, B., The expanding role of electrospray ionization mass spectrometry for probing reactive intermediates in solution. *Molecules* **2012,** *17* (10), 11507-37.

13. Van Berkel, G. J.; McLuckey, S. A.; Glish, G. L., Electrospray ionization of porphyrins using a quadrupole ion trap for mass analysis. *Analytical Chemistry* **1991,** *63* (11), 1098-1109.

14. Brown, T. A.; Chen, H.; Zare, R. N., Detection of the short-lived radical cation intermediate in the electrooxidation of N,N-dimethylaniline by mass spectrometry. *Angew Chem Int Ed Engl* **2015,** *54* (38), 11183-5.

15. Iftikhar, I.; Brajter-Toth, A., Solution or Gas Phase? Oxidation and Radical Formation in Electrospray Ionization Mass Spectrometry (ESI MS). *Electroanalysis* **2015,** *27* (12), 2872-2881.

16. He, G.-Y.; Cai, T.; Xu, X.-Y.; Fang, D.-M.; Wu, Z.-J., Radical ions and dehydro cations in detection of 2,3′-bisindolylmethanes using electrospray mass spectrometry. *International Journal of Mass Spectrometry* **2016,** *410*, 63-67.

17. Qiu, R.; Zhang, X.; Luo, H.; Shao, Y., Mass spectrometric snapshots for electrochemical reactions. *Chem Sci* **2016,** *7* (11), 6684-6688.

18. Li, A.; Luo, Q.; Park, S. J.; Cooks, R. G., Synthesis and catalytic reactions of nanoparticles formed by electrospray ionization of coinage metals. *Angew Chem Int Ed Engl* **2014,** *53* (12), 3147-50.

19. Morand, K.; Talbo, G.; Mann, M., Oxidation of peptides during electrospray ionization. *Rapid Communications in Mass Spectrometry* **1993,** *7* (8), 738-743.

20. Liu, S.; Griffiths, W. J.; Sjövall, J., On-column electrochemical reactions accompanying the electrospray process. *Anal Chem* **2003,** *75* (4), 1022-30.

21. Pei, J.; Zhou, X.; Wang, X.; Huang, G., Alleviation of Electrochemical Oxidation for Peptides and Proteins in Electrospray Ionization: Obtaining More Accurate Mass Spectra with Induced High Voltage. *Analytical Chemistry* **2015,** *87* (5), 2727-2733.

22. Peintler-Krivan, E.; Van Berkel, G. J.; Kertesz, V., Minimizing analyte electrolysis in electrospray ionization mass spectrometry using a redox buffer coated emitter electrode. *Rapid Communications in Mass Spectrometry* **2010,** *24* (9), 1327-1334.

23. Van Berkel, G. J.; Zhou, F., Characterization of an electrospray ion source as a controlled-current electrolytic cell. *Analytical Chemistry* **1995,** *67* (17), 2916-2923.

24. Van Berkel, G. J.; Zhou, F., Electrospray as a Controlled-Current Electrolytic Cell: Electrochemical Ionization of Neutral Analytes for Detection by Electrospray Mass Spectrometry. *Analytical Chemistry* **1995,** *67* (21), 3958-3964.

25. Blades, A. T.; Ikonomou, M. G.; Kebarle, P., Mechanism of electrospray mass spectrometry. Electrospray as an electrolysis cell. *Analytical Chemistry* **1991,** *63* (19), 2109-2114.

26. Freitas, D.; Chen, X.; Cheng, H.; Davis, A.; Fallon, B.; Yan, X., Recent Advances of In-Source Electrochemical Mass Spectrometry. *Chempluschem* **2021,** *86* (3), 434-445.

27. Wan, Q.; Chen, S.; Badu-Tawiah, A. K., An integrated mass spectrometry platform enables picomole-scale real-time electrosynthetic reaction screening and discovery. *Chem Sci* **2018,** *9* (26), 5724-5729.

28. Li, M.; Li, H.; Allen, N. R.; Wang, T.; Li, L.; Schwartz, J.; Li, A., Nested-channel for on-demand alternation between electrospray ionization regimes. *Chemical Science* **2021,** *12* (5), 1907-1914.

29. Badu-Tawiah, A. K.; Wu, C.; Cooks, R. G., Ambient Ion Soft Landing. *Analytical Chemistry* **2011,** *83* (7), 2648-2654.

30. Lee, J. K.; Walker, K. L.; Han, H. S.; Kang, J.; Prinz, F. B.; Waymouth, R. M.; Nam, H. G.; Zare, R. N., Spontaneous generation of hydrogen peroxide from aqueous microdroplets. *Proceedings of the National Academy of Sciences* **2019,** *116* (39), 19294.

31. Gong, K.; Xu, F.; Grunewald, J. B.; Ma, X.; Zhao, Y.; Gu, S.; Yan, Y., All-Soluble All-Iron Aqueous Redox-Flow Battery. *ACS Energy Letters* **2016,** *1* (1), 89-93.

32. Michalski, R.; Thiebaut, D.; Michalowski, B.; Ayhan, M. M.; Hardy, M.; Ouari, O.; Rostkowski, M.; Smulik-Izydorczyk, R.; Artelska, A.; Marcinek, A.; Zielonka, J.; Kalyanaraman,

B.; Sikora, A., Oxidation of ethidium-based probes by biological radicals: mechanism, kinetics and implications for the detection of superoxide. *Sci Rep* **2020,** *10* (1), 18626.

33. Wang, S. T.; Zhegalova, N. G.; Gustafson, T. P.; Zhou, A.; Sher, J.; Achilefu, S.; Berezin, O. Y.; Berezin, M. Y., Sensitivity of activatable reactive oxygen species probes by fluorescence spectroelectrochemistry. *Analyst* **2013,** *138* (15), 4363-4369.

34. Zielonka, J.; Srinivasan, S.; Hardy, M.; Ouari, O.; Lopez, M.; Vasquez-Vivar, J.; Avadhani, N. G.; Kalyanaraman, B., Cytochrome c-mediated oxidation of hydroethidine and mito-hydroethidine in mitochondria: Identification of homo- and heterodimers. *Free Radical Biology and Medicine* **2008,** *44* (5), 835-846.

6 Ultra-low Current Electrospray Ionization of Chloroform Solution for the Analysis of Perfluorinated Sulfonic Acids

6.1 Introduction

The advent of electrospray ionization (ESI) in the 1980s was a turning point for the development of liquid chromatography-mass spectrometry (LC-MS), and since then LC-MS has been widely used for qualitative and quantitative analysis of a broad class of small molecules (e.g., lipids, vitamins, xenobiotics, and peptides) in complex biological and environmental media.[1] In 1993, nanoESI was introduced,[2] in which a high voltage was applied to the solution loaded in a capillary emitter (1-10 μm, tip diameter). It is distinguished by lower flow rate (25-200 nL/min), smaller initial charged droplets, lower sample consumption(~microliter), and higher sensitivity.[3] It has been applied in direct MS analysis without separation.[4–6] Spray ionization from a variety of substrates (paper[7], wooden tip[8], thread[9]) often is operated in the nano flow modes[10] in food safety, drug discovery, environmental monitoring applications.[11]

The electrospray methods typically have detection limits at ppb to ppm levels.[11] Many environmental contaminants are monitored or regulated at trace levels down to ~ppt concentrations. One example is perfluorooctanoate sulfonate (PFOS), which has been on the Stockholm Convention's list of persistent organic pollutants since 2009. As a result, most ESI methods for ppt level PFOS involve extraction and preconcentration, such as solid phase microextraction (SPME),[12,13] aerosol enrichment,[14] and electromembrane extraction.[15]

Liquid-liquid extraction is a robust procedure that has one less step than SPME.[16] For water samples, typical extraction solvents are non-polar and often incompatible with conventional ESI.[17–22] Conventional ESI methods are also known to produce nanoamps of ionization current, while mass analyzers nowadays only require a much low current ranging from individual ions to

picoampere. Reducing ionization current could be a way to conserve samples and to improve detection limit. Recently, it was demonstrated that ESI at femtoampere and picoampere (<1 nA) currents can be conducted [23–25] and show practical benefits in regulating flow rates,[24,26] improving microsample utilization[27], and reducing carry over contamination in direct analysis[28]. ESI under voltage lower than conventional onset has also been utilized in the on-demand analysis with miniature mass spectrometer.[29] It was also demonstrated that nanoESI could be generated from a much larger emitter by using super atmospheric pressure,[30] or giga-ohm resister[31]. Inspired by these recent progresses, we investigate the electrospray ionization of chloroform solution in low current and low voltage regimes. Femtoampere and picoampere ionization was established, characterized, and applied in the analysis of ppt level PFOS in drinking water.

6.2 Experimental

6.2.1 Chemicals and materials

Water (HPLC grade) and methanol (HPLC-grade, ≥99.9%, Product NO. 34860) were purchased from Sigma-Aldrich (St. Louis, MO). Chloroform (Certified ACS reagent, ≥99.8 %, Cat No: C298-4) was obtained from Fisher Chemical (Waltham, MA). Perfluoro-1-hexane sulfonic acid (PFHxS), perfluoro-1-hepane sulfonic acid (PFHpS), perfluoro-1-octane sulfonic acid (PFOS), perfluoro-1-nonane sulfonic acid (PFNS), perfluoro-1-decane sulfonic acid (PFDS), and perfluoro-1-dodecane sulfonic acid (PFDoS) were purchased from Wellington Laboratories (Guelph, Ontario, Canada). $^{13}C_8$-PFOS was purchased from Cambridge Isotope Laboratories (Tewksbury, MA). Methionine, 1-heptanesulfonic acid sodium salt, and 4-(2-hydroxyethyl-)-1-piperazineethanesulfonic acid (HEPES) were purchased from Sigma-Aldrich (St. Louis, MO). 1,2-ethanedisulfonic acid was purchased from TCl AMERICA (Portland, OR). Borosilicate glasses (ID 0.86mm, O.D. 1.5 mm) were purchased from Sutter Instrument (Novato, CA).

6.2.2 Measurement of ionization current

The ion current measurements were performed on the setup developed by Li et al.[24,25]. A 1000-Mohm resistor was connected into the circuit, as shown in **Figure 6-1**. The distance between the emitter tip and the copper plate (as ground, MS inlet) was around 0.5 cm.

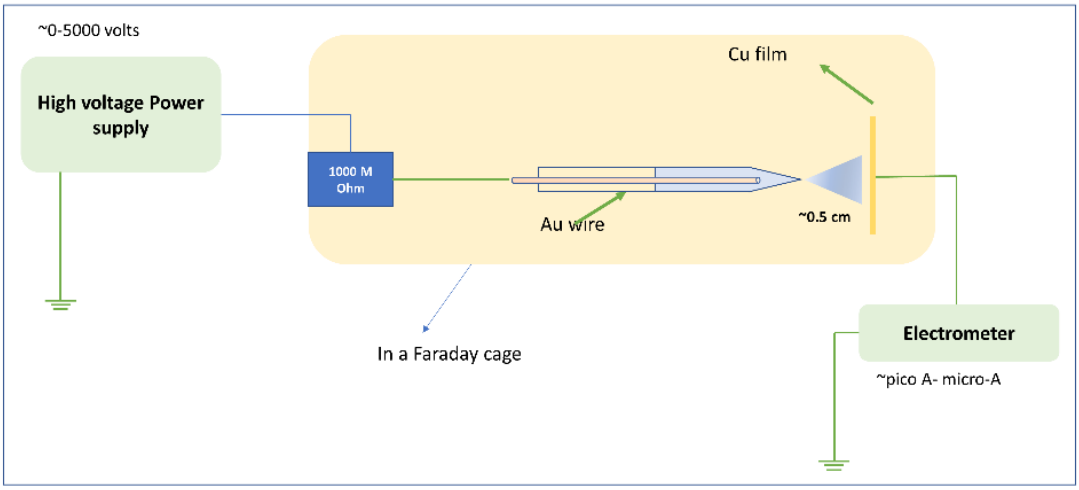

Figure 6-1. The setup of ion current measurement, A DC high voltage power supply (Model PS350) was purchased from Stanford Research System, Inc. (Sunnyvale, CA). The electrometer (Keithley 6514) was used. To reduce background noise, all measurements were carried out inside a grounded Faraday cage.

6.2.3 Conductivity of solvents measurements

The setup of conductivity measurements was shown in **Figure 6-2**, in which a 5-mL solution was added into the glass bottle holding the two copper electrodes (width = 0.6 cm, length = 6.5 cm). The copper electrodes were immersed in the solution for about 1.1 cm. The current was measured using an electrometer (Keithley 6514). A stepwise DC voltage (Stanford Research Systems, Inc. Model PS350) ranging from 50 v to 250 v was applied to the copper electrode. The resulting currents were then plotted against the voltages to acquire the linear regression curve, of which the slope ß was the resistance R (ohm) of the solution. Since the glass bottle is not a standard conductivity cell, the cell constant k (**Equation 6-1**) was determined using HPLC grade water, which has a known conductivity of 0.0549 µS/cm, as a control. Note that the conductance G is the

reciprocal of the resistance R. The slope β_{water} was $2.0\times10^5\,\Omega$, so the conductivity equation was derived as **Equation 6-3**.

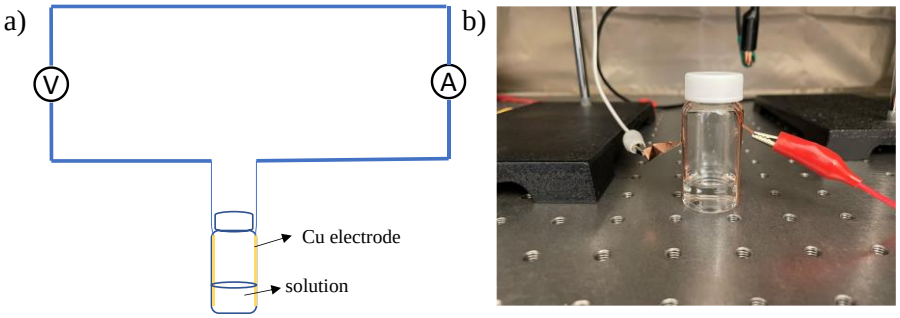

Figure 6-2. a) The setup for conductivity measurement. b) the photography of the 20-ml glass bottle used as the conductivity cell

$$C = kG$$

Equation 6-1

$$C = \frac{5.49 \times 10^{-5}\,\beta_{water}}{\beta_{solvent}}$$

Equation 6-2

$$C = \frac{11}{\beta_{solvent}}$$

Equation 6-3

6.2.4 Optimization of extraction solvent

Three extraction solvents, including ethyl acetate, chloroform, and hexane (Fisher chemical, Waltham, MA) were tested. The extraction was performed at room temperature. The 0.5-mL water sample spiked with 100 µg/L PFOS was stored in 1.5 mL polypropylene centrifuge tubes. Then 500 µL organic solvent (1:1 v/v) was added into the tubes, followed by 3-min sonication. 100 µL organic solution was transferred into another empty 0.5 mL polypropylene centrifuge tube and dried. After that, 100 µL spray solvent methanol spiked with analogue internal standards (20 µg/L PFHxS) was added to monitor the extraction

efficiency. About 5 µL sample was transferred into the capillary emitter for ESI-MS analysis. The measurements were repeated three times. The extraction efficiency was evaluated with the signal ratio of PFOS at *m/z* 499 to IS at *m/z* 399 in the full scan mode (*m/z* range: 350-550). The results are shown in **Table 6-1**.

Table 6-1. The optimization of the extraction solvents for PFOS analysis. Each data point is the ratio of a 30-scan average in full scan mode. The samples were analyzed by ESI-MS in triplicate.

Extraction Solvent	**Signal ratio of PFOS/IS**
Ethyl acetate	3.96±0.25
Hexane	0.00
Chloroform	0.78±0.16

6.2.5 Water sample preparations

Spring water samples were purchased from local markets (Rochester, NH). Tap water and deionized water were collected from Parson Hall of the University of New Hampshire (Durham, NH). 500 µL extraction solvent ethyl acetate was added into 1 mL water sample containing 50 ppt 13C8-PFOS as internal standard, which was placed in 1.5-mL polypropylene microcentrifuge tube (BioChrom, Amazon, Seattle, WA). The tubes were vortexed for 10 seconds and sonicated them for 3 min using a digital ultrasonic cleanser (H&B Luxuries, Amazon, Seattle, WA), followed by the transfer of ethyl acetate (ACS grade, Cat No. E145-4, Fisher Chemical, Waltham, MA) into an empty 1.5-mL polypropylene microcentrifuge tube (BioChrom, Amazon, Seattle, WA). In the fume hood, a N_2 stream was used to dry out about 0.4 mL of extraction solvent. The N_2 flow rate was carefully adjusted to avoid blowing the sample out. It usually took about 15 minutes to completely remove the solvent. The samples were then reconstituted with 30 µL of chloroform solvent for further examination.

6.2.6 ESI-MS analyses

The electrospray emitters were made from borosilicate capillaries (1.5 mm o.d./0.86 mm i.d., BF 150-86-10, Sutter Instruments, Novato, CA, USA) by pulling the tip to o.d. 3.5 ± 0.5 μm with a Model P-1000 micropipette puller (Sutter Instrument, Novato, CA, USA). The emitter tips were checked by a bright-field microscope (Olympus IX73). The capillary emitters were held around 0.5 cm in front of the MS inlet using a manual XYZ stage. A gold wire was inserted into the emitters at 0.5 cm from the emitter tip. An aliquot of 5 μL sample was loaded into the emitter for each measurement.

The mass spectrometric analysis was implemented on an LTQ-XL linear ion trap mass spectrometer (Thermo Fisher Scientific, San Jose, CA). Full scan negative mass spectra were obtained over a mass-to-charge ratio (m/z) range from 100 to 800. The other parameters were as below: inlet capillary voltage -36 V, the tube lens voltage -57 V, and the capillary temp 150 ˚C. The automatic gain control (AGC) target value was 3.0×104. A single scan mass spectrum was recorded with maximum an injection time (IT) of 100 ms and 3 micro-scans, unless otherwise stated. Mass spectra were recorded and analyzed using the Xcalibur 4.1 (Thermo Fisher Scientific, San Jose, US) and R (open-source statistical software).

6.2.7 Limits of Detection (LODs) determination

A primary dilution standard solution (1000 ppt) was prepared for the calibration of 6 target analytes (**Table 6-5**) via serial dilution of the stock standard solutions in HPLC grade water to prepare a 7-point calibration solution from 5 to 400 ppt concentrations. All calibration solutions were prepared in triplicate, followed by liquid-liquid extraction (described 6.2.5 section) for further analysis. Each data point for constructing the calibration curves contained 100 scans

acquired in full scan (m/z range 100-800) with 3 micro-scans (One complete scan is called a microscan in the ion trap). A mass tolerance of 100 ppm to the targeted m/z values was used for calculating the signal ratio between analytes and the internal standard. The calibration curves were summarized in Table 1. The LODs were determined using the formula 3*SB/m, where SB is the standard deviation of the targeted PFS in blank and m is the slope of the calibration curve. As the LOD of PFHxS was beyond the lowest calibration concentration (5 ppt), it was recalculated with the corrected slope after removing the lowest point.

6.2.8 Distribution coefficient of ethyl acetate

The distribution coefficient (D) of PFOS in ethyl acetate and water was determined by **Equation 6-4**. Based on the definition of distribution coefficient D, the D value is the ratio of the concentration of a solute between two immiscible solvents. Herein, the concentration of PFOS in ethyl acetate C_{PFOS} was determined by one-pint method, shown in **Equation 6-5**. Since 10 ppb PFOS was spiked into HPLC grade water ($C_{water} = 10\ ppb$), the signal intensity ratio between analyte and IS $\frac{I_{PFOS}}{I_{IS}}$ was 2.5, and the concentration of IS ($^{13}C_8$-PFOS) in ethyl acetate C_{IS} was 10 ppb, consequently the D was 2.5, shown in **Equation 6-6**.

$$D = \frac{C_{ethyl\ acetate}}{C_{water}}$$

Equation 6-4

$$C_{PFOS} = \frac{I_{PFOS}}{I_{IS}} C_{IS}$$

Equation 6-5

$$D = \frac{(I_{PFOS}/I_{IS})C_{IS}}{C_{water}}$$

Equation 6-6

6.3 Results and Discussions

6.3.1 Ultralow current using chloroform in ESI

The current-voltage (I-V) response curves are acquired using methanol and chloroform as spray solvents in ESI, respectively. The onset current is defined as the ion currents that are significantly higher than the baseline (30-50 fA) [24,25], and thus the related voltages are the onset voltages. As shown in **Figure 6-3**, the onset voltage of methanol is -800 volts, producing an ion current of 5.6 ± 1.7 nA. It is consistent with our previous study that neat organic solvents such as methanol, isopropanol, and acetonitrile cannot obtain ionization currents in the pA region.[25] Alternatively, after -500 V is applied, chloroform produces an ion current of 92 ± 16 fA.

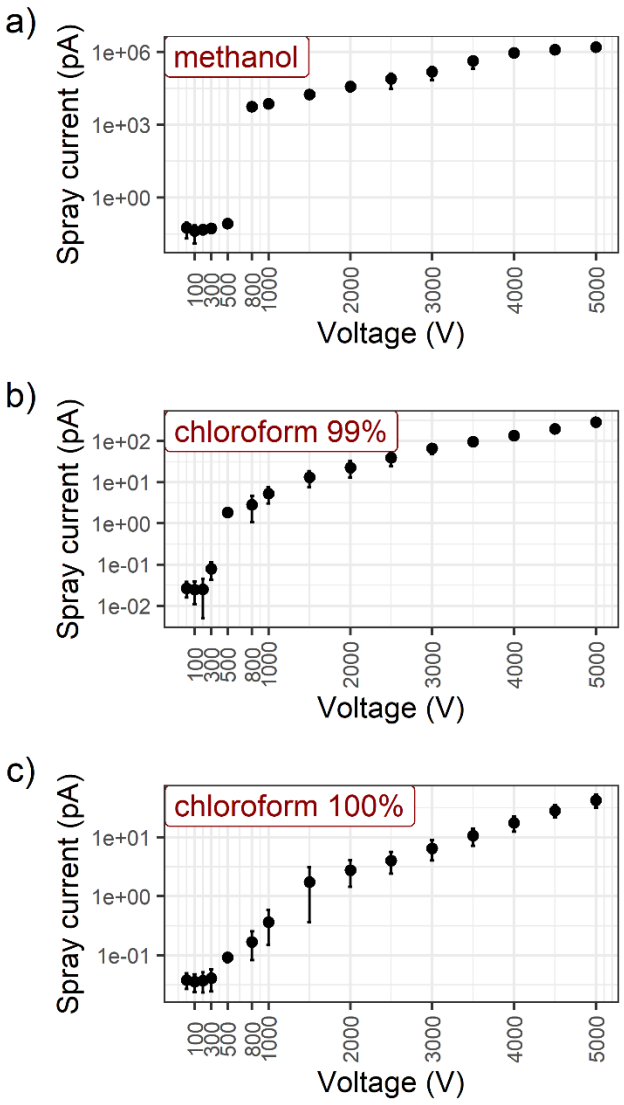

Figure 6-3. Current versus voltage (I-V) curves of a) methanol containing 10 ppb PFOS, b) 99% chloroform containing 1% methanol and 10 ppb PFOS; c) chloroform containing 10 ppb. Negative voltages were applied. The error bar is the standard deviation of 3 measurements. As the baseline varied from -30 to +30 fA, a 40-fA subtraction was made from all the measurement currents to make sure all the data points have same signs.

Therefore, we deduce from the I-V curves that a few hundred volts should be able to induce electrospray for chloroform. With further mass spectrometric analysis of 10 ppb PFOS in chloroform, we find that the PFOS ion at *m/z* 499 is detectable at -300 V (**Figure 6-4a**), which is even lower than the onset voltage of -500 V anticipated by the I-V curve. Thus, the actual onset voltage for chloroform should be -300 V, which yields ion currents of 41 ± 17 fA that overlaps with the baseline (30-50 fA). Meanwhile, the -300 V ESI onset of chloroform (the onset voltage in ESI refers to the minimum voltage required to produce detectable ion signals) is lower than that of a methanol solution, as no signal occurs after subjecting -500 V to the methanol sample (**Figure 6-4b**). Smith et al.'s model shows that the onset voltage of ESI (cone-jet) is proportional to the square root of the surface tension T of the solution when the ESI capillary radius and emitter-MS distance are constant,[32] which is confirmed by the fact that water (T: 72.8 mN/m) has a greater onset voltage than methanol (T: 22.7 mN/m).[29] However, this property does not seem to be the cause in the chloroform versus methanol system, at least in the sub nano current modes, since methanol's surface tension is akin to that of chloroform (T: 27.5 mN/m), **Table 6-2.** Meanwhile, a surfactant is known to reduce the surface tension of aqueous picoliter droplets at mM concentrations,[33] It is unlikely that a surfactant like PFOS at nM concentrations would alter the surface tension of nonpolar solvents. The I-V curves (Figure **6-3**b, c) show similar onset voltage (300, 500 V) when spiking 1% MeOH in chloroform, which suggests hydrogen bond between MeOH, and glass surface is not a key factor to the establishment of femto ESI mode.

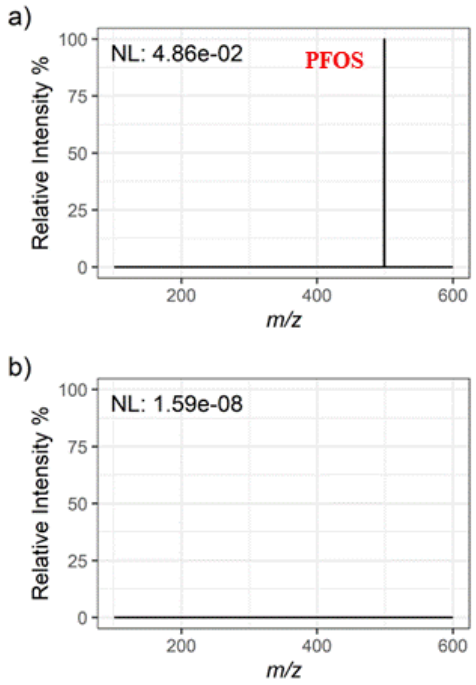

Figure 6-4. Representative mass spectra of 10 ppb PFOS acquired by applying sub-kilovolt voltages to a) chloroform at -300 V; b) methanol at -500 V. As only two out of the twenty-one scans had ions detected, the mass spectrum (b) was an average of two scans. The mass spectrum b) was an average of 20 scans. The humidity was 20%, and the room's temperature was 24.7 °C.

Table 6-2. The physical properties of solvents methanol and chloroform. These parameters are looked up in the Handbook of Organic Solvent Properties [ae].

Solvent	Surface tension @ 20°C in mN/m	Viscosity 10^{-3} Pa s	Dielectric constant
Methanol	22.7	0.54	33
Chloroform	27.5	0.54	4.8

[e] Smallwood IM, ed. Bibliography. In: *Handbook of Organic Solvent Properties*. Butterworth-Heinemann; 1996:305-306. doi:10.1016/B978-0-08-052378-1.50077-3

The ionization currents above the onset voltage for chloroform are kept in the picoampere range (0.092-42 pA) when the spray voltage increases to -5000 volts. Adding PFOS to chloroform slightly increases its conductivity (**Table 6-3**), yet it is still 3 orders of magnitude lower than that of methanol and water, so it stays in the pA range. When the chloroform volume decreases from 100% to 99%, the ion currents remain in the picoampere range (1.8-290 pA) but with an overall increase over the neat chloroform. It suggests that the ion currents can be tuned within the fA to nA range by varying the ratio of methanol and chloroform.

Table 6-3. The conductivity of solvents. The measurements were conducted at 23 °C.

Solvent	Measured R/ Ω	Conductivity C (S/cm)
18.2 MΩ /cm HPLC grade water	2.0e5	5.49e-5
Chloroform	4.1e9	2.7e-9
10 ppb PFOS in chloroform	3.5e9	3.1e-9
Methanol	5.1e6	2.1e-6

6.3.2 Effect of the chloroform compositions on PFOS analysis

The effect of spiking methanol into chloroform on the establishment of a sub-nanoampere regime has been investigated, in which the ionization currents (I) are examined against varied chloroform content levels in spray solvents at 1.5 kV. **Figure 6-5** shows that the ion currents remain in the picoampere range (~230 pA) with the spiking of methanol being no more than 5% (v/v). while methanol percentage above 10% result in ion currents in the range of 3-38 nA, which is within the typical nanoESI current region (1-100 nA) with a μm tip glass emitter characterized by Schmidt et al. [34] We conclude that the ESI enters nanoampere mode when the methanol concentration exceeds 10% (v/v).

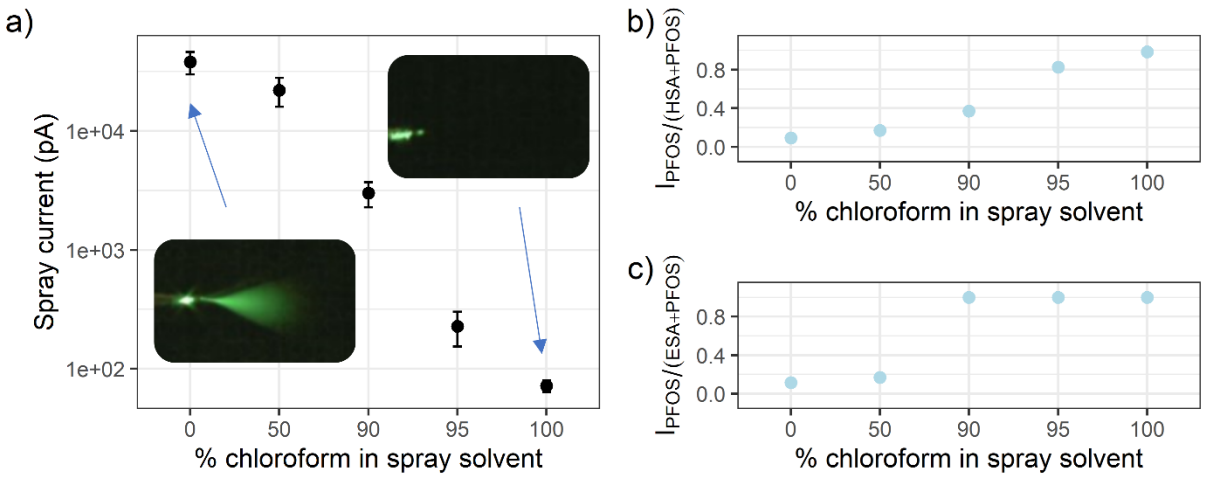

Figure 6-5. a) Plot of spray ion current against various spiked methanol volumes in chloroform (v/v). The lower inserted photograph is of the spray plume using methanol as the spray solvent, and the upper inserted photograph is of the spray plume using the 100% neat solvent chloroform. Each point represents the average of three measurements, and the error bar is the standard deviation of three measurements. For the purposes of comparison, the spray voltage was kept at 1.5 kV. b) plot of the relative signal intensity of PFOS to the sum of HSA and PFOS against various spiked methanol volumes in chloroform (v/v). The molar ratio of HSA and PFOS in solution was kept at 100 (10 µM HSA and 0.1 µM PFOS). c) Plot of the relative signal intensity of PFOS to the sum of ESA and PFOS against various spiked methanol volumes in chloroform (v/v). The molar ratio of ESA and PFOS in solution was kept at 100 (10 µM ESA and 0.1 µM PFOS). All the relative signal intensity was obtained from the 100-scan averaged mass spectra.

How does the mode switch influence the PFOS analysis? In our preliminary study, we found that PFOS was ionized from the chloroform solvent (**Figure 6-4a**) as the dominant peak without solvent background ions, which was consistent with Henderson et al.'s study that the surfactant ions can be ionized by nonpolar solvent, [20] and agreed with Henriksen et al.'s findings that the species that had a significant non-polar portion and already existed as a ion are expected to give a high ESI response as well. [35,36] Consequently, two model compounds (1-heptanesulfonic acid sodium (HSA) and ethane-1,2-disulfonic acid (ESA), **Figure 6-6**) are mixed with PFOS separately to evaluate the relative PFOS ion abundance in various chloroform compositions. The molar ratio of PFOS to the other compound is held constant (1:100). With 100% methanol as the spray solvent, the relative signal intensity of PFOS at *m/z* 499 is $1/10^{th}$ of that of HSA corresponding to the ion at *m/z* 179 (**Figure 6-6b**). As the molar ratio of PFOS to HSA is 1:100, we infer that PFOS exhibits a higher ionization efficiency due to the greater hydrophobicity of the fluorocarbon chain than the hydrocarbon chain. [37]. When the percentage of methanol decreases to 90%, **Figure 6-5b** shows that the relative abundance of the PFOS ion increases from 9% to 37% in the nanoamp range. After switching to sub-nanoamp mode with methanol below 5%, the relative PFOS ion intensity rises from 83% to 98%, becoming the most abundant peak in the full scan spectrum.

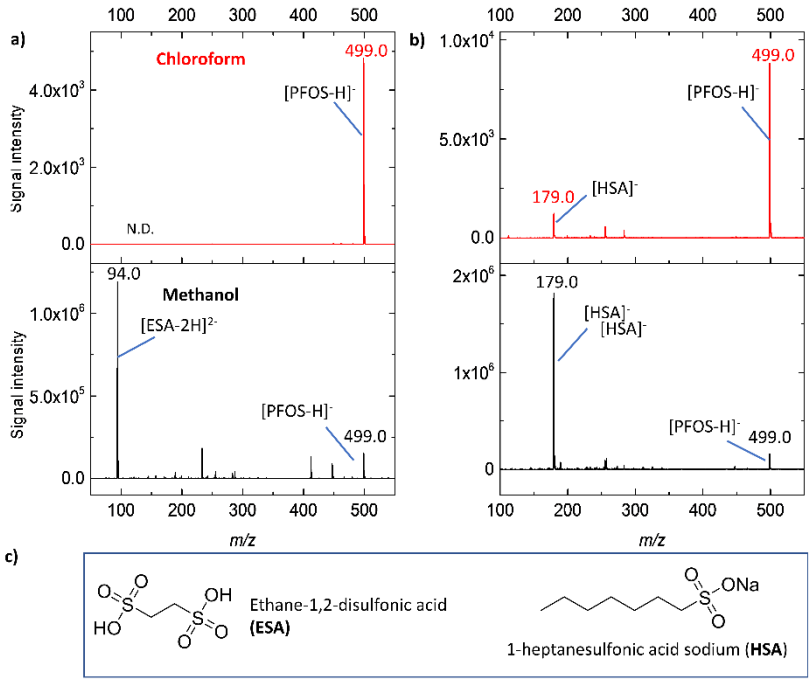

Figure 6-6. Mass spectra of 10 µM ethane-1,2-disulfonic acid (ESA) and 0.1 µM PFOS in spray solvent methanol and chloroform with 1% methanol **a)**. Mass spectra of 10 µM 1-hepanesulfonic acid sodium (HSA) and 0.1 µM PFOS in spray solvent methanol and chloroform with 0.1% methanol **b)**. The mass spectra were an average of 50 scans. The ion at *m/z* 94 was a doubly charged ion $[ESA\text{-}2H]^{2-}$, and the ion at *m/z* 179 corresponds to HSA anion. Spray voltages 1.5 kV and 2.5 kV were applied to methanol and chloroform, respectively. **c)** the structures of 1-hepanesulfonic acid sodium and ethane-1,2-disulfonic acid.

Additionally, the ESA and PFOS mixtures show a similar trend, wherein the doubly charged ion at *m/z* 94 corresponds to ESA, **Figure 6-6a**. As it can be seen in **Figure 6-5c**, the relative signal intensity of $[PFOS\text{-}H]^-$ to the total of $[ESA\text{-}2H]^{2-}$ and $[PFOS\text{-}H]^-$ increases noticeably from 11% to 100% (9-fold) as the percentage of methanol decreases from 100% to 90%. This is to say that $[ESA\text{-}2H]^{2-}$ becomes undetectable in 90% chloroform. The early loss of doubly charged ESA ions may be explained by the chloroform's inability to effectively stabilize multiply charged species. [38] We also observe a slight shift to singly charged ions as the amount of chloroform increases from 50% to 80%, as shown in **Figure 6-7**.

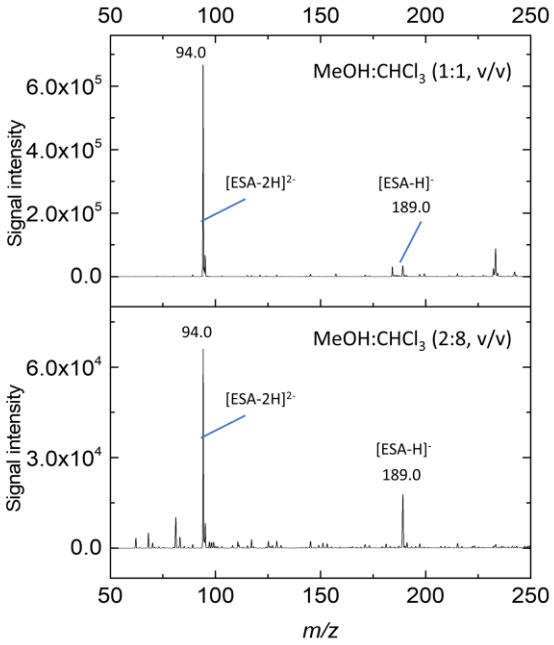

Figure 6-7. Mass spectra of 10 µM ESA in spray solvent: a) MeOH: $CHCl_3$ (1:1, v/v); b) MeOH: $CHCl_3$ (2:8, v/v). The mass spectrum is an average of 50 consecutive scans. The spray voltage was 1.5 kV.

Therefore, when there is more than 95% chloroform present, the ionization of PFOS is enhanced with significantly reduced solvent background ions. The reverse correlation between the ionization enhancement to PFOS and the ionization current also indicates that ESI preferentially produces PFOS ions when the spray current is in the picoampere regime, and this is in association with a low flow rates (V_f) based on the scaling law ($V_f \propto I^{7/4}$) developed by Pfeifer and Hendricks.[39] The relatively low flow rate in the pA region is also confirmed by the much fainter ESI plume using chloroform as the spray solvent as opposed to methanol, as shown in **Figure 6-5a** in the inserted photographs. Interestingly, the reported PFOS solubility in methanol was greater than the chlorinated solvents, such as tetrachloride (37 g/L vs. 25 mg/L)[40] While there is no reported (to our best knowledge) solubility for PFOS in chloroform, the calculated solvation energy (ΔGsolv°) for PFOS in these solvents (MeOH: -4.79 kcal/mole, CCl_4: 7.14 kcal/mole, $CHCl_3$: 2.99 kcal/mole) (**Table 6-4**) suggest the solubility in chloroform could be lower than that in methanol. This also suggests that chloroform droplets are more energetically favorable (than methanol) for desolvation process that would facilitate the formation of gas phase PFOS ions.[41f]

Table 6-4. Solvation free energy of PFOS in different solvents.[g]

Solvent	$\Delta G_{solv}°$ (kcal/mol)
methanol	-4.79
chloroform	2.99
tetrachloride	7.14

[g] The $\Delta G_{solv}°$ was calculated using Gaussian 09 with the input lines Ground state/6-311+G (2d, p), self-consistent reaction field (SCRF)= (charge-density (D) based solvation model SM, SMD, externaliteration, DoVacuum).

6.3.3 Effect of the spray voltages and inlet temperatures on PFOS signal intensity

In our preliminary study, a significant signal intensity of PFOS dependent on spray voltage was found. **Figure 6-8a** illustrates the relationship between the applied voltages and PFOS signal intensities, showing that the PFOS signal intensity rises from 54 to 7.3×10^5 as the spray voltage increases from 0.5 kV to 4 kV (Negative mode). Meanwhile, for almost 20 minutes, we did not observe any tips being damaged by the-4.0 kV spray voltage applied to chloroform. The relatively low spray current in chloroform compared to that in methanol (140 pA vs. 930 nA, **Figure 6-3**) is responsible for the glass tip's stability at high voltages, since it significantly reduces the Joule heating.[42] This argument is further supported by **Figure 6-7**, which depicts a burning glass tip after applying -4.0 kV to methanol for over 5 min. Meanwhile, no corona discharge phenomenon has been observed when using voltages up to -5 kV, which might be attributed to the electron capture of chlorinated solvents.[38,43] Consequently, a 4-kV spray voltage in negative mode is used for the following PFSs analysis in water samples.

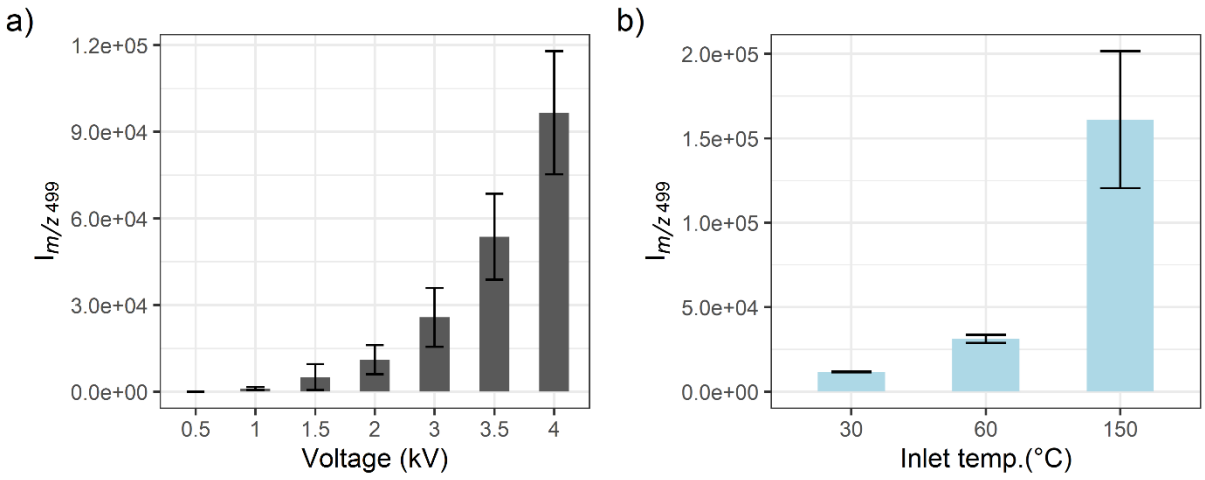

Figure 6-8. a) Bar plot of the signal intensity of $[PFOS-H]^-$ at m/z 499 in 99% chloroform containing 10 ppb PFOS and 1% methanol against spray voltages from 0.5 kV to 4 kV. b) Bar plot of the signal intensity of $[PFOS-H]^-$ at m/z 499 in 99% chloroform containing 10 ppb PFOS and 1% methanol against inlet temperatures. 4-kV spray voltages were used. Each bar represents the signal intensity of PFOS at m/z 499 in the 50-scan averaged full scan mass spectrum. The error bar is the standard deviation of triplicate measurements.

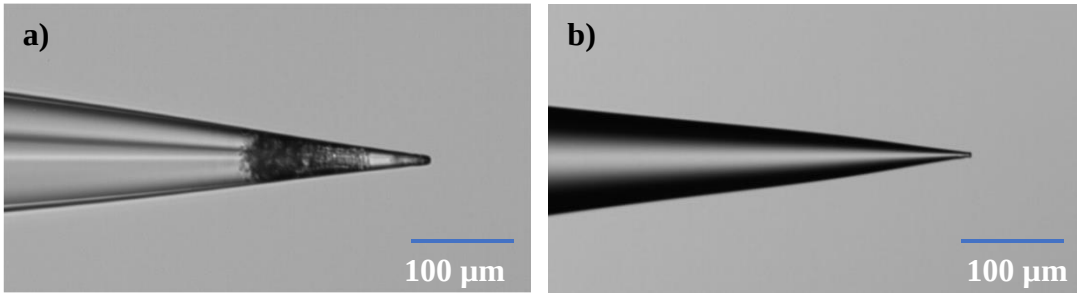

Figure 6-9. Photograph of an emitter tip after applying 4.0 kv to the emitter tip containing methanol. **b)** chloroform. Note that auto exposure was used.

The inlet temperature can aid in the desolvation of charged droplets, which affects the transmission efficiency and is related to the volatility of spray solvents.[44] **Figure 6-8a** shows the PFOS signal intensity as a function of inlet temperatures from 30 °C to 150 °C. We observed an overall ion abundance increase with increasing temperature (1.2×10^4 to 1.6×10^5), as a result, 150 °C was used in the study. It is amazing that the inlet temperature has a comparable effect on the spray solvents methanol and chloroform (**Figure 6-10**), despite the fact that the low-polar solvent chloroform (boiling point: 61.2°C) evaporates faster than the polar solvent methanol (boiling point: 64.7°C) and has a relatively lower flow rate than methanol.

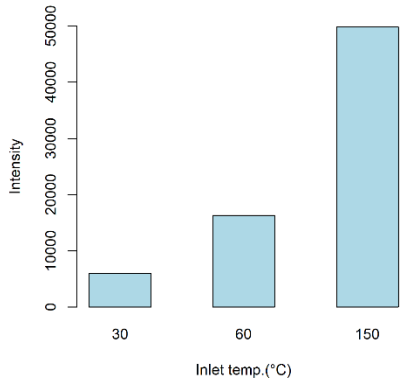

Figure 6-10. Bar plot of signal intensity of PFOS at *m/z* 499 in methanol containing 10 ppb PFOS against inlet temperature. Each bar represents an average of 50 scans. The spray voltage was 1.5 kV.

6.3.4 Comparative study of PFOS and PFHxS analysis in methanol and chloroform

Figure 6-11 shows the full scan mass spectrum of 10 µg/L PFOS and PFHxS in the spray solvent methanol, which is used as a control since it is commonly used in PFOS analysis based on mass spectrometry methods. The most abundant ion is presented at *m/z* 255. This signal represents deprotonated palmitate acid.[14] The PFHxS signal at *m/z* 399 and the PFOS signal at *m/z* 499 show a relative signal intensity of 24% and 29% to the base peak, respectively. The signal-to-noise ratios (SNRs) of PFHxS and PFOS are 16 and 15, respectively. The SNRs are determined by dividing the absolute signal intensity of the analyte by the noise. The latter is defined as the 50% quantile

of the signals in a certain mass range (e.g., the noise for the peak at *m/z* 399 is the median intensity in the *m/z* range 395-405, shown in **Figure 6-12**). With 99% (v/v) chloroform/methanol as the spray solvent, the mass spectrum changes significantly, as shown in **Figure 6-11b**. The PFHxS and PFOS anions become the dominant peaks, corresponding to SNRs of 1448 and 1338, respectively. The background ions at *m/z* 255 significantly decrease, and other background peaks disappear or occur in low abundances. Consequently, the SNRs have been enhanced nearly 100-fold. It is noteworthy that the absolute ion intensity of PFOS in methanol is stronger than that in chloroform when the spray voltage was the same for both solvents. However, when the spray voltage increases to 4.5 kV for chloroform, the absolute PFOS signal intensity becomes comparable and even higher than that in methanol. The enhancement of the PFOS signal in the sub-nanoampere region could also be explained by the low dielectric constants of chloroform (κ_{MeOH}: 33 vs. κ_{CHCl3}: 4.7), and in association with this, a small number of ions are accessible for charge separations under the electric potential. Consequently, chloroform generates a smaller population of noise-causing ions than methanol does, giving it a higher SNR. The mass spectrum of the blank solvent chloroform is shown in **Figure 6-13**.

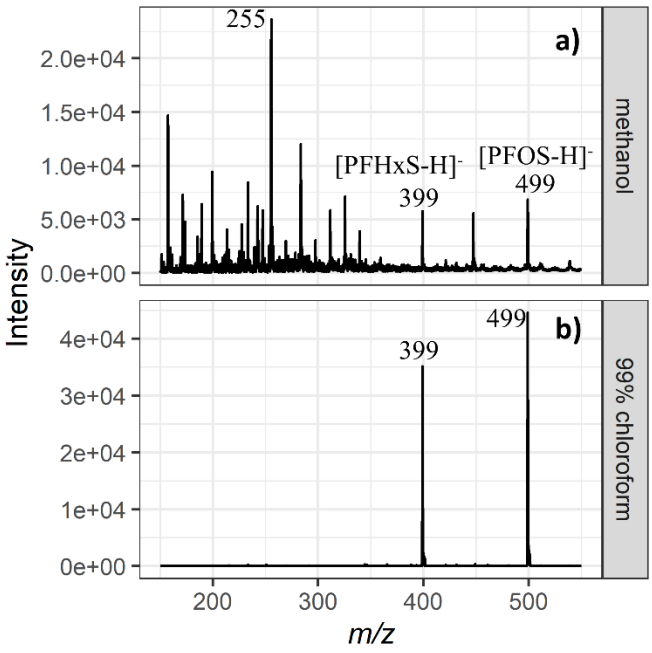

Figure 6-11. Mass spectra of 10 ppb PFHxS and PFOS in spray solvents: a) MeOH, b) chloroform with 1% methanol. ~5 µL solution was loaded into the capillary emitter for analysis. A total of 0.5-min scans were averaged to acquire the mass spectrum. The spray voltages were 1.5 kV and 4.5 kV for MeOH and chloroform, respectively.

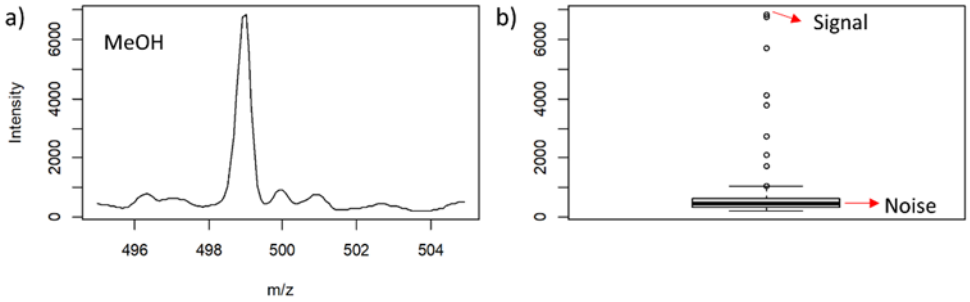

Figure 6-12. Signal to noise ratio determination. a) A plot of signal intensity versus *m/z* in a range of 495 to 505; b) The boxplot of a). Noise is defined as the medium throughout this range, and the signal is the maximum intensity at the targeted *m/z* value, in this case, the signal of ion at *m/z* 499 is the maximum intensity of 6800. The SNRs were automatically processed using R functions. The raw data was directly read by the package 'rawrr' developed by Kockmann and Panse.[h]

[h] Kockmann T, Panse C. The rawrr R Package: Direct Access to Orbitrap Data and Beyond. *J Proteome Res*. 2021;20(4):2028-2034. doi:10.1021/acs.jproteome.0c00866

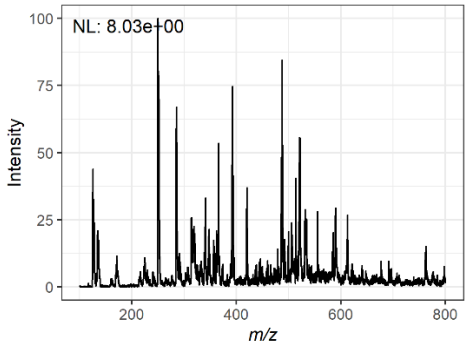

Figure 6-13. Representative mass spectrum of the blank solvent 99% chloroform in negative mode. The mass spectrum was an average of 20 scans. The spray voltage was set to 1.5 kV. The NL is 8.03.

The disappearance of background ions also confirms the selective ionization accessibility of chloroform to PFSs relative to other co-existing species, which has already been demonstrated in **Figure 6-11**. Additionally, we have examined two other species, methionine (Met) and 4-(2-hydroxyethyl-)-1-piperazine ethane sulfonic acid (HEPES), which possess polar groups in their backbones (**Figure 6-14**). The ions at *m/z* 148 and *m/z* 237 confirm the presence of Met and HEPES in methanol, respectively. While neither of them is detected in chloroform, even HEPES contains the -SO_3H group, which is prone to losing a proton in negative mode. This is consistent with the observation made by Xia et al. that nonpolar ESI has limited ionization performances. [17] The exception to PFSs becomes an advantage to develop quantitative method for PFSs.

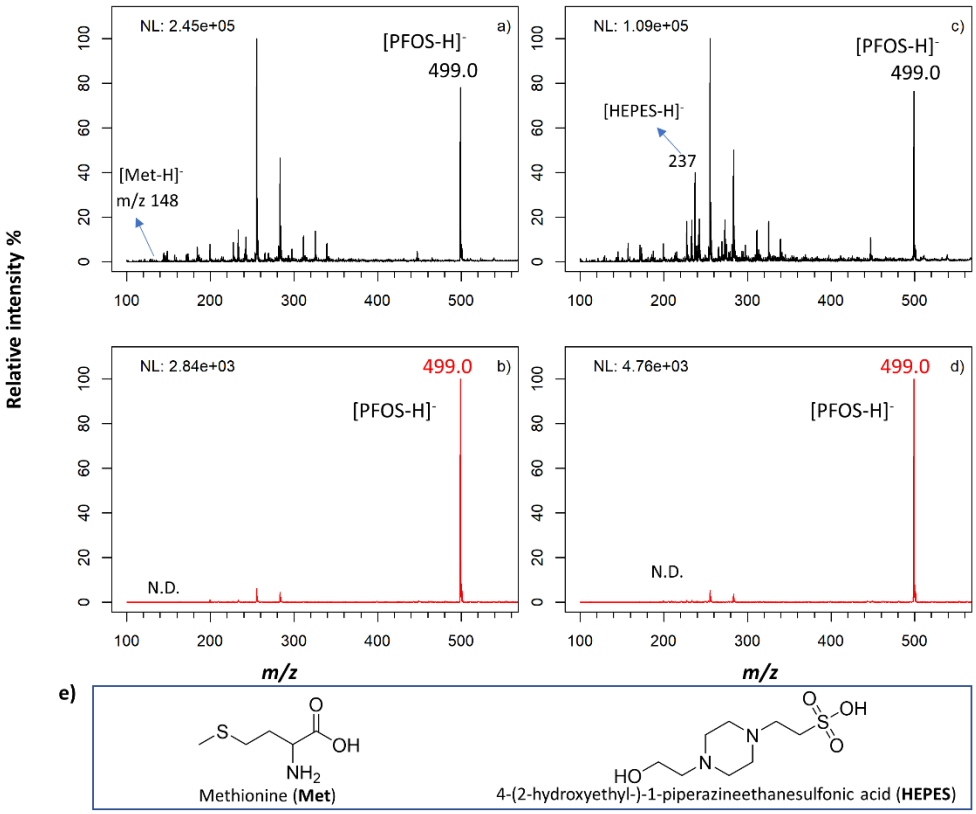

Figure 6-14. Representative mass spectra of 10 µM methionine (Met) and 0.1 µM PFOS in spray solvent methanol a) and chloroform with 1% methanol b). Mass spectra of 10 µM HEPES and 0.1 µM PFOS in spray solvent methanol c) and chloroform with 1% methanol d). The structure of Met and HEPES are depicted in e). The mass spectra were an average of 50 scans. The ion at *m/z* 148 was corresponding to $[Met\text{-}H]^-$, and the ion at *m/z* 237 was $[HEPES\text{-}H]^-$. Spray voltages 1.5 kV were applied to both methanol and chloroform, N.D. represents not detected.

6.3.5 Application: PFSs analysis in water sample

These results make chloroform the ideal spray solvent to analyze PFSs in real water samples. **Figure 6-15** shows the mass spectrum of 100 ppt PFSs mixture (PFHxS, PFHpS, PFOS, PFNS, PFDS, and PFDoS, **Table 6-5**) in 99% (v/v) chloroform. The signals at *m/z* 399, 449, 499, 549, 599, and 699 correspond to $[PFHxS-H]^-$, $[PFHpS-H]^-$, $[PFOS-H]^-$, $[PFNS-H]^-$, $[PFDS-H]^-$, and $[PFDoS-H]^-$, respectively. The instrumental detection limits (IDLs) of PFSs are estimated to be 25 ppt with SRN in the range of 2.5-4.5 since no PFCs are detectable after a further 2-fold dilution, **Figure 6-15b and 6-15c**. In contrast, nanoESI analysis of ppt level PFSs in methanol did not produce observable peaks at m/z 399, 449, 499, 549, 599 and 699 in the full scan spectrum (**Figure 6-16**), further demonstrating how femtoampere ESI using chloroform could improve the detectability of certain analytes. (Wu et al.[45] used methanol as the spray solvent in nanoESI analysis of PFSs, which reaches ILDs of 4-25 ppt but requires a high-resolution Thermo Scientific^{TM} Q Exactive Orbitrap mass spectrometer. Compared to that, the approach demonstrated here can obtain comparable IDLs but with a unit-resolution LTQ mass spectrometer.

Table 6-5: A summary of PFSs analyzed in the study

Name	Abbreviation	Molecular formula	Molecular mass	*m/z* (ESI-)
Perfluoro-1-hexane sulfonic acid	PFHxS	$C_6F_{13}SO_3H$	400	399
Perfluoro-1-hepane sulfonic acid	PFHpS	$C_7F_{15}SO_3H$	450	449
Perfluoro-1-octane sulfonic acid	PFOS	$C_8F_{17}SO_3H$	500	499
Perfluoro-1-nonane sulfonic acid	PFNS	$C_9F_{19}SO_3H$	550	549
Perfluoro-1-decane sulfonic acid	PFDS	$C_{10}F_{21}SO_3H$	600	599
Perfluoro-1-dodecane sulfonic acid	PFDoS	$C_{12}F_{25}SO_3H$	700	699

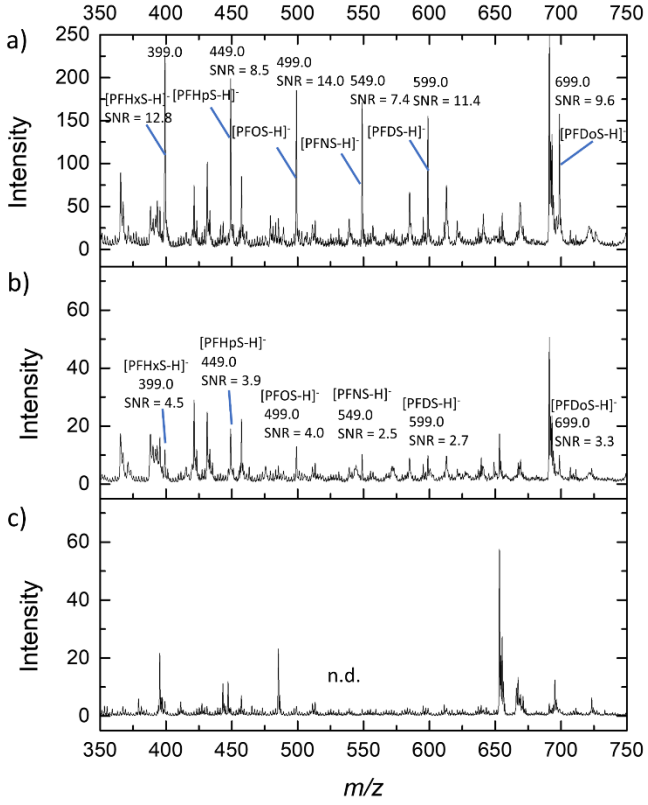

Figure 6-15. Mass spectra of a) 100 ppt PFSs; b) 25 ppt PFSs; c) 12.5 ppt PFSs in chloroform containing 1% methanol. The mass spectrum is an average of a 0.5-min scan. The calculation of SNRs is depicted in the supporting information. The n.d. represents “not detected”.

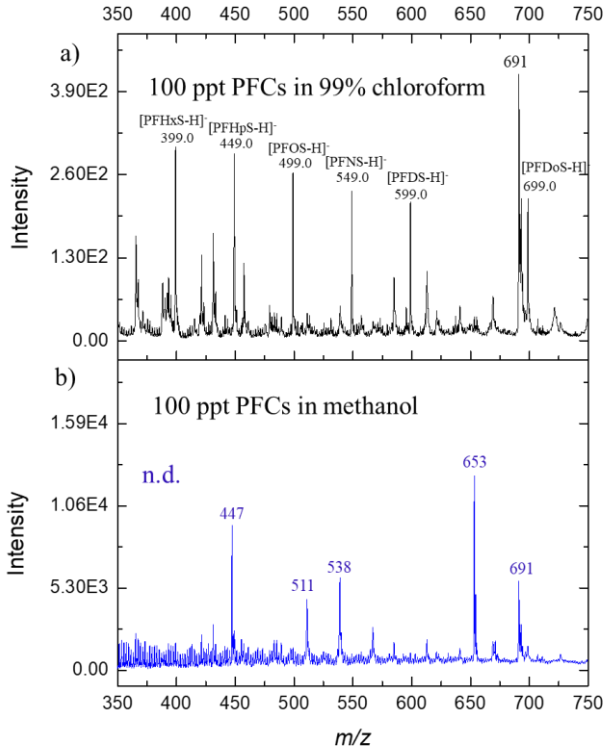

Figure 6-16. Mass spectra of 100 ppt PFSs in a) 99% chloroform and b) methanol

Since our IDLs are 25 ppt and the gold-standard approach (Method 537.1) utilizing LC-MS/MS reports a detection limit of 2.7 ppt for PFOS using a 250-ml drinking water sample,[46] we need to do a quick enrichment of PFSs to monitor PFSs. Because direct ESI-MS consumes microliter samples, we simply decrease the sample volume from 1 mL to 30~50 µl to boost the concentrations of PFSs above the lDLs. A liquid-liquid extraction following evaporation to exchange water for chloroform (**Scheme 6-1**) is employed. Since chloroform exhibits a weak efficiency for extracting PFOS from water (**Table 6-1**), ethyl acetate is selected as the extraction solvent. Since the distribution factor D of PFOS between ethyl acetate and water (pH =7) is 2.5, the volume ratio between water and ethyl acetate is set to 2 as a sizeable sample to extraction solvent volume ratio can increase the concentration of analyte in extraction solvent.[47] The internal standard IS calibration curves for 6 PFSs compounds are obtained by spiking the standards into HPLC grade water samples. As shown in **Table 6-6**, the obtained linear coefficients (R^2) are no less than 0.99 within the concentration range of 5-400 ppt, showing excellent linearity. The LODs (Limits of detection) of PFSs are varied in the range of 0.38-5.1 ppt. It might in part be attributed to the different extraction efficiency of 6 PFSs when using ethyl acetate. The LOD of PFOS is 1.0 ppt, which is comparable to the EPA 537.1 method (2.7 ppt). As a result, the method is sensitive enough for real sample analysis. Meanwhile, the 1-mL water sample consumption allows for testing PFOS across a wide area and on a large scale, compared to Deng et al.'s wooden-tip ambient ESI-MS method, in which 1000-mL of drinking water was needed to get an 8400-fold enrichment for PFOS analysis. [12] Furthermore, the IDL of PFOS at 25 ppt is at the same level as the method LOD (1 ppt ×1000 µL/30 µL=33 ppt), indicating the method is somehow devoid of the impact of matrix species. It is worth noting that the extraction solvent was not systematically optimized in this work. Other

fluorinated non-polar solvents [48] and dispersive liquid-liquid microextraction (DLLME) strategy [48–50] would provide improved extraction performances, particularly for the more complicated samples such as wastewater and urine. A more comprehensive study on the low current ionization phenomenon of non-polar solvents could enable the direct analysis of these extracts.

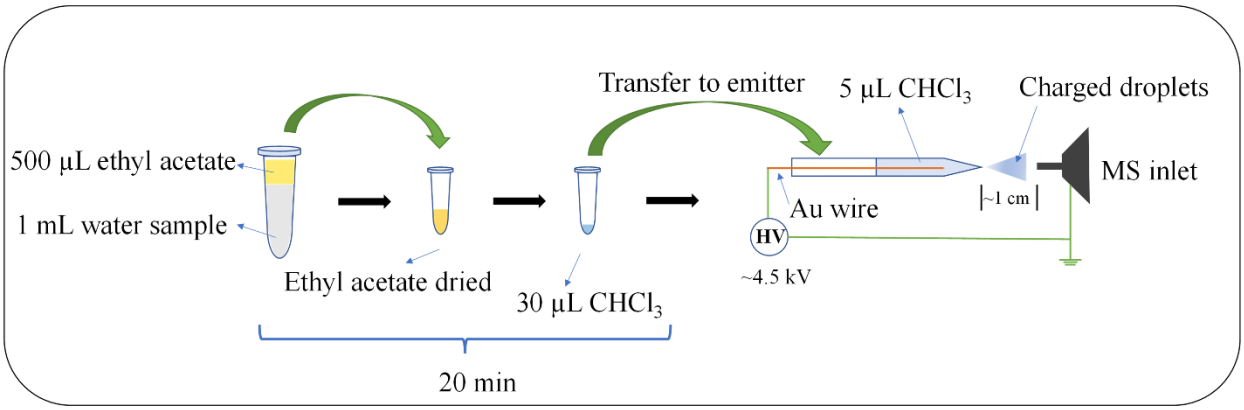

Scheme 6-1. The schematic of PFSs analysis, where $^{13}C_8$-PFOS internal standard was spiked into water sample at a final concentration of 50 ppt. The details are described in the Experimental section.

Table 6-6. The calibration curves of targeted PFSs. The determination of LODs is described in the experimental section.

Analyte	Regression equation	Linear range (ppt)	R^2	LOD (ppt)
PFHxS	Y=0.00081X+ 0.047	10-400	0.9989	5.1
PFHpS	Y=0.0145X+0.1347	5.0-400	0.9999	2.0
PFOS	Y=0.0205X+ 0.0573	5.0-400	0.9997	1.0
PFNS	Y=0.0211X+ 0.0333	5.0-400	0.9994	1.1
PFDS	Y=0.0168X+ 0.0904	5.0-400	0.9998	1.4
PFDoS	Y=0.0092X+ 0.0058	5.0-400	0.9941	0.38

Single-blind experiments were designed to verify the precision and accuracy of our method. One participant was assigned to prepare the samples by spiking various amounts of standard PFOS into HPLC grade water, while another participant in this study, who was kept ignorant of the concentration information, was assigned to analyze the samples using the developed method. Repeat measurements of 10 samples were performed over a period of 1 to 5 days. The method's precision is evaluated with the relative standard deviation (RSD) of. triplicate measurements of 10 samples; likewise, a measure of accuracy is relied on the known spiked concentration of PFOS with which to compare the measured values to obtain the absolute relative error % from the 10 samples. As shown in **Table 6-6**, the RSDs of PFOS in 10 samples measured on different days are less than 15%, demonstrating good repeatability. The absolute relative errors % of PFOS at various concentrations are less than 15% as well, exhibiting good accuracy. It is worth noting that the RSD is above 15% when the PFOS concentrations are less than 5 ppt, which are outside the range of the calibration curve.

Table 6-7. The single blind analysis results of PFOS in 10 spiked samples (#1-10) and real water samples (#A1-A4). The prepared concentrations of the 10 spiked samples were concealed from the operator until all the measurements were completed. The accuracy is the absolute relative error % which is acquired by dividing the average of the measured concentrations by the prepared concentrations. NA represents "not available". A new internal standard calibration curve (5-200 ppt PFOS, IS: 50 ppt) was constructed for each measurement. After all the three measurements, the concentrations of the unknowns were calculated and summarized in the table.

# Sample	Prepared conc.	Day 1	Day 6	Day 7	Average	Precision	Accuracy
1	**20**	23	24.2	19.1	22.1	12%	11%
2	**5**	4.8	4.1	5.4	4.8	14%	96%
3	**10**	10.5	10	11.7	10.8	7.5%	8%
4	**50**	58	61	46.3	55	14%	10%
5	**8**	8.8	7	7.4	7.7	12%	4%
6	**60**	65	60.1	62	62.4	4.0%	4%
7	**168**	161.4	163	153.2	159.2	3.3%	5%
8	**104**	95.5	90.4	85.6	90.5	5.5%	13%
9	**40**	44	37.2	43.4	41.5	9.1%	4%
10	**25**	26.7	25.3	29.2	27.1	7.3%	8%
A1	**NA**	n.d.	n.d.	n.d.			
A2	**NA**	16.3	18.9	16.5	17.2	8.3%	
A3	**NA**	2.4	1.9	1.7	2.0	18%	
A4	**NA**	2.4	3.2	4.4	3.4	30%	

The applicability of our simple PFSs analysis method is evaluated by the real water samples shown in **Table 6-8**. The PFHxS and PFOS are detected at a concentration of 5.1 ppt and 17 ppt in a spring water 1, which agrees with the concentration of PFOS (18 ppt) reported by the NHDES (New Hampshire Department of Environmental Services) but is a little bit off the reported PFHxS concentration (12 ppt).[51] No PFSs are detected in spring water sample 2 (**Figure 6-17a**). After spiking 50 ppt PFSs into a spring water sample, 6 PFSs are detected unambiguously in full scan mode (**Figure 6-17b**). Meanwhile, PFOS is measured at concentrations of 5.4 ppt and 50 ppt in tap water and deionized water, respectively. Those unknown peaks detected in the water samples indicate the method could work with other types of analytes. (**Figure 6-18)**. These results demonstrated the satisfactory application of our method for all kinds of water samples with a 1-mL sample volume on the ion trap analyzer-based mass spectrometer, suggesting its potential application for coupling with portable mass spectrometers such as the Mini β miniature mass spectrometer.[15,52]

Table 6-8. Analysis results of PFSs in 4 water samples. Each water sample was measured in triplicates. The n.d. stands for "not detected".

Water	Analyte (ppt)					
	PFHxS	PFHpS	PFOS	PFNS	PFDS	PFDoDS
Spring water 1	5.1 ± 0.7	n.d.	17± 0.3	n.d.	n.d.	n.d.
Spring water 2	n.d.	n.d.	n.d.	n.d.	n.d.	n.d.
Tap water	n.d.	n.d.	5.4 ± 0.09	n.d.	n.d.	n.d.
Deionized water	n.d.	n.d.	50 ± 1	n.d.	n.d.	n.d.

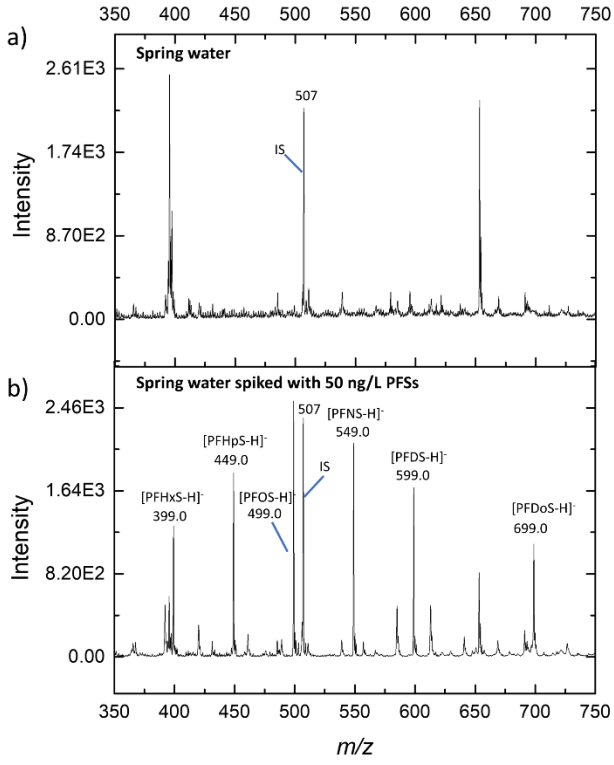

Figure 6-17. Mass spectra of PFSs analysis in a) spring water and b) spiked spring water with 50 ppt PFSs. IS was 50 ppt. The mass spectrum is an average of 100 scans.

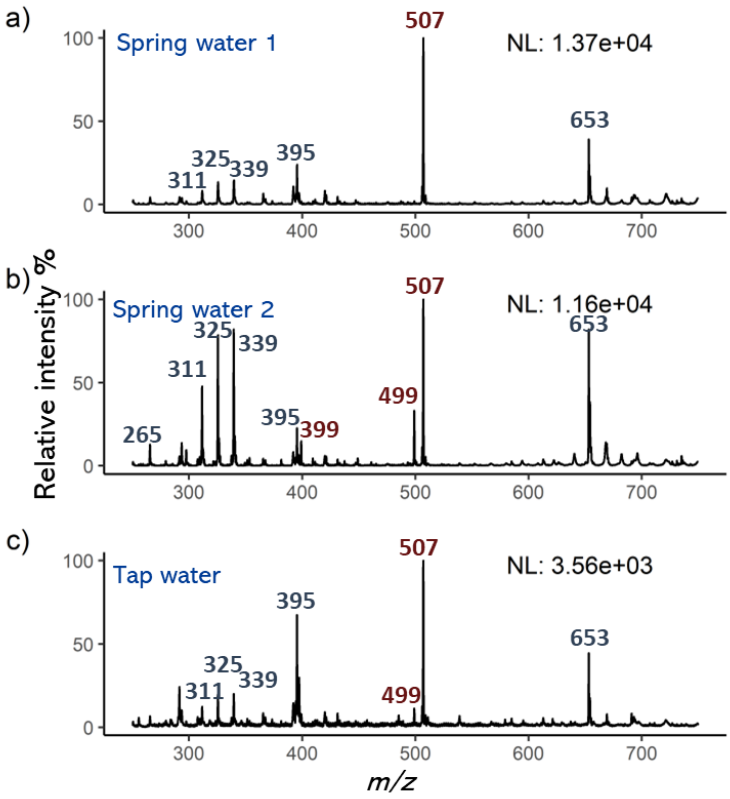

Figure 6-18. Representative mass spectra of water samples: a) drinking water 1 b) drinking water 2 c) tap water.

6.4 Conclusions

With femtoampere and picoampere sensitivity, electrospray ionization phenomena can be observed when using chloroform solvent. Interestingly, the -300 V ESI onset of chloroform is lower than that of a methanol solution. No corona discharge phenomenon was observed when using voltages up to -5 kV. Compared with aqueous solution in previous femtoampere ESI work,[24,25] chloroform provides a wider voltage window for the operating electrospray in the femtoampere and picoampere regimes. Chloroform also allowed the spiking of methanol so that the ESI may be adjusted between nanoampere and femtoampere modes. When there was more than 95% chloroform present, the ionization of PFOS was enhanced with significantly reduced solvent background ions. This enabled the quantitative analysis of ppt level PFOS in water using no more than 1 mL sample. The direct ionization of nonpolar solution makes the method compatible with many more extraction-based sample preparation workflow. It may also extend the application range of ESI-MS analysis to anhydrous chemical environment, or to other novel chemical systems [53] that would not dissolve in conventional ESI solvents. The ultra-low current ion beam could allow reducing the need of heating and pumping, making the method beneficial for miniature and low impact mass spectrometers.

6.5 Acknowledgement

This material is based upon work supported by the Chemical Measurement and Imaging program in the National Science Foundation Division of Chemistry under Grant No. CHE-2203289 and funding from the Established Program to Stimulate Competitive Research.

6.6 References

1. Pitt JJ. Principles and Applications of Liquid Chromatography-Mass Spectrometry in Clinical Biochemistry. *Clin Biochem Rev*. 2009;30(1):19-34.

2. Small volume and low flow-rate electrospray lonization mass spectrometry of aqueous samples - Gale - 1993 - Rapid Communications in Mass Spectrometry - Wiley Online Library. Accessed November 9, 2022. https://analyticalsciencejournals.onlinelibrary.wiley.com/doi/10.1002/rcm.1290071111

3. Karas M, Bahr U, Dülcks T. Nano-electrospray ionization mass spectrometry: addressing analytical problems beyond routine. *Fresenius J Anal Chem*. 2000;366(6):669-676. doi:10.1007/s002160051561

4. Fligge TA, Kast J, Bruns K, Przybylski M. Direct monitoring of protein-chemical reactions utilising nanoelectrospray mass spectrometry. *J Am Soc Mass Spectrom*. 1999;10(2):112-118. doi:10.1016/S1044-0305(98)00131-7

5. Ren Y, McLuckey MN, Liu J, Ouyang Z. Direct Mass Spectrometry Analysis of Biofluid Samples Using Slug-Flow Microextraction Nano-Electrospray Ionization. *Angewandte Chemie International Edition*. 2014;53(51):14124-14127. doi:10.1002/anie.201408338

6. Wickremsinhe E, Singh G, Ackermann B, Gillespie T, Chaudhary A. A Review of Nanoelectrospray Ionization Applications for Drug Metabolism and Pharmacokinetics. *CDM*. 2006;7(8):913-928. doi:10.2174/138920006779010610

7. Liu J, Wang H, Manicke NE, Lin JM, Cooks RG, Ouyang Z. Development, Characterization, and Application of Paper Spray Ionization. *Anal Chem*. 2010;82(6):2463-2471. doi:10.1021/ac902854g

8. Hu B, So PK, Chen H, Yao ZP. Electrospray Ionization Using Wooden Tips. *Anal Chem*. 2011;83(21):8201-8207. doi:10.1021/ac2017713

9. Jackson S, Badu-Tawiah AK. Enhanced thread spray mass spectrometry: a general method for direct pesticide analysis in various complex matrices. *Analyst*. 2021;146(18):5592-5600. doi:10.1039/D1AN00651G

10. Huang MZ, Yuan CH, Cheng SC, Cho YT, Shiea J. Ambient Ionization Mass Spectrometry. *Annual review of analytical chemistry (Palo Alto, Calif)*. 2010;3:43-65. doi:10.1146/annurev.anchem.111808.073702

11. Guo XY, Huang XM, Zhai JF, et al. Research Advances in Ambient Ionization and Miniature Mass Spectrometry. *Chinese Journal of Analytical Chemistry*. 2019;47(3):335-346. doi:10.1016/S1872-2040(19)61145-X

12. Deng J, Yang Y, Fang L, Lin L, Zhou H, Luan T. Coupling Solid-Phase Microextraction with Ambient Mass Spectrometry Using Surface Coated Wooden-Tip Probe for Rapid Analysis of Ultra Trace Perfluorinated Compounds in Complex Samples. *Anal Chem*. 2014;86(22):11159-11166. doi:10.1021/ac5034177

13. Hou YJ, Deng J, He K, Chen C, Yang Y. Covalent Organic Frameworks-Based Solid-Phase Microextraction Probe for Rapid and Ultrasensitive Analysis of Trace Per- and Polyfluoroalkyl Substances Using Mass Spectrometry. *Anal Chem*. 2020;92(15):10213-10217. doi:10.1021/acs.analchem.0c01829

14. Cao Y, Lee C, Davis ETJ, et al. 1000-Fold Preconcentration of Per- and Polyfluorinated Alkyl Substances within 10 Minutes via Electrochemical Aerosol Formation. *Anal Chem*. 2019;91(22):14352-14358. doi:10.1021/acs.analchem.9b02758

15. Chen M, Shang Y, Bai H, Ma Q. Electromembrane Extraction and Dual-Channel Nanoelectrospray Ionization Coupled with a Miniature Mass Spectrometer: Incorporation of a Dicationic Ionic Liquid-Induced Charge Inversion Strategy. *Anal Chem*. 2022;94(26):9472-9480. doi:10.1021/acs.analchem.2c01921

16. Rawa-Adkonis M, Wolska L, Przyjazny A, Namieśnik J. Sources of Errors Associated with the Determination of PAH and PCB Analytes in Water Samples. *Analytical Letters*. 2006;39(11):2317-2331. doi:10.1080/00032710600755793

17. Xia B, Gao Y, Ji B, Ma F, Ding L, Zhou Y. Analysis of Compounds Dissolved in Nonpolar Solvents by Electrospray Ionization on Conductive Nanomaterials. *J Am Soc Mass Spectrom*. 2018;29(3):573-580. doi:10.1007/s13361-017-1873-y

18. Huang Z, Yao YN, Li W, Hu B. Analytical properties of electrospray ionization mass spectrometry with solid substrates and nonpolar solvents. *Analytica Chimica Acta*. 2019;1050:105-112. doi:10.1016/j.aca.2018.10.064

19. Duffin KL, Henion JD, Shieh JJ. Electrospray and tandem mass spectrometric characterization of acylglycerol mixtures that are dissolved in nonpolar solvents. *Anal Chem*. 1991;63(17):1781-1788. doi:10.1021/ac00017a023

20. Henderson MA, McIndoe JS. Ionic liquids enable electrospray ionisation mass spectrometry in hexane. *Chem Commun*. 2006;(27):2872-2874. doi:10.1039/B606938J

21. Li A, Wang H, Ouyang Z, Cooks RG. Paper spray ionization of polar analytes using non-polar solvents. *Chem Commun*. 2011;47(10):2811-2813. doi:10.1039/C0CC05513A

22. Lv Y, Bai H, He Y, Yang J, Ma Q. Selective and sensitive analysis by reactive easy ambient sonic-spray ionization: Synergistic combination of non-polar spray solvent and dicationic ionic liquid. *Talanta*. 2020;215:120929. doi:10.1016/j.talanta.2020.120929

23. Li M, Li H, Allen NR, et al. Nested-channel for on-demand alternation between electrospray ionization regimes. *Chem Sci*. 2021;12(5):1907-1914. doi:10.1039/D0SC06221A

24. Li H, Allen N, Li M, Li A. Conducting and characterizing femto flow electrospray ionization. *Analyst*. 2022;147(6):1071-1075. doi:10.1039/D1AN02190G

25. Allen NR, Li H, Cheung A, Xu G, Zi Y, Li A. Femtoamp and picoamp modes of electrospray and paper spray ionization. *International Journal of Mass Spectrometry*. 2021;469:116696. doi:10.1016/j.ijms.2021.116696

26. Han Z, Chen LC. High-pressure nanoESI of highly conductive volatile and non-volatile buffer solutions from a large Taylor cone: Effect of spray current on charge state distribution. *International Journal of Mass Spectrometry*. 2022;476:116845. doi:10.1016/j.ijms.2022.116845

27. Frey BS, Damon DE, Badu-Tawiah AK. Emerging trends in paper spray mass spectrometry: Microsampling, storage, direct analysis, and applications. *Mass Spectrom Rev*. 2020;39(4):336-370. doi:10.1002/mas.21601

28. Dowling S, McBride EM, McKenna J, Glaros T, Manicke NE. Direct soil analysis by paper spray mass spectrometry: Detection of drugs and chemical warfare agent hydrolysis products. *Forensic Chemistry*. 2020;17:100206. doi:10.1016/j.forc.2019.100206

29. Wu J, Zhang W, Ouyang Z. On-Demand Mass Spectrometry Analysis by Miniature Mass Spectrometer. *Anal Chem*. 2021;93(15):6003-6007. doi:10.1021/acs.analchem.1c00575

30. Han Z, Chen LC. Generation of Ions from Aqueous Taylor Cones near the Minimum Flow Rate: "True Nanoelectrospray" without Narrow Capillary. *J Am Soc Mass Spectrom*. 2022;33(3):491-498. doi:10.1021/jasms.1c00322

31. Rahman MdM, Wu D, Chingin K, Xu W, Chen H. High ohmic resistor hyphenated gel loading tip nano-electrospray ionization source for mini mass spectrometer. *Talanta*. 2019;202:59-66. doi:10.1016/j.talanta.2019.04.052

32. Smith DPH. The Electrohydrodynamic Atomization of Liquids. *IEEE Transactions on Industry Applications*. 1986;IA-22(3):527-535. doi:10.1109/TIA.1986.4504754

33. Bzdek BR, Reid JP, Malila J, Prisle NL. The surface tension of surfactant-containing, finite volume droplets. *Proceedings of the National Academy of Sciences*. 2020;117(15):8335-8343. doi:10.1073/pnas.1915660117

34. Schmidt A, Karas M, Dülcks T. Effect of different solution flow rates on analyte ion signals in nano-ESI MS, or: when does ESI turn into nano-ESI? *Journal of the American Society for Mass Spectrometry*. 2003;14(5):492-500. doi:10.1016/S1044-0305(03)00128-4

35. Cech NB, Enke CG. Practical implications of some recent studies in electrospray ionization fundamentals. *Mass Spectrometry Reviews*. 2001;20(6):362-387. doi:10.1002/mas.10008

36. Henriksen T, Juhler RK, Svensmark B, Cech NB. The relative influences of acidity and polarity on responsiveness of small organic molecules to analysis with negative ion electrospray ionization mass spectrometry (ESI-MS). *Journal of the American Society for Mass Spectrometry*. 2005;16(4):446-455. doi:10.1016/j.jasms.2004.11.021

37. Dalvi VH, Rossky PJ. Molecular origins of fluorocarbon hydrophobicity. *Proc Natl Acad Sci U S A*. 2010;107(31):13603-13607. doi:10.1073/pnas.0915169107

38. Cole RB, Harrata AK. Solvent effect on analyte charge state, signal intensity, and stability in negative ion electrospray mass spectrometry; implications for the mechanism of negative ion formation. *J Am Soc Mass Spectrom*. 1993;4(7):546-556. doi:10.1016/1044-0305(93)85016-Q

39. Pfeifer RJ, Hendricks CD. Parametric studies of electrohydrodynamic spraying. *AIAA Journal*. 1968;6(3):496-502. doi:10.2514/3.4525

40. Meng P, Deng S, Du Z, et al. Effect of hydro-oleophobic perfluorocarbon chain on interfacial behavior and mechanism of perfluorooctane sulfonate in oil-water mixture. *Scientific Reports*. 2017;7(1):44694. doi:10.1038/srep44694

41. Fenn JB. Ion formation from charged droplets: roles of geometry, energy, and time. *Journal of the American Society for Mass Spectrometry*. 1993;4(7):524-535. doi:10.1016/1044-0305(93)85014-O

42. Kulyk DS, Swiner DJ, Sahraeian T, Badu-Tawiah AK. Direct Mass Spectrometry Analysis of Complex Mixtures by Nanoelectrospray with Simultaneous Atmospheric Pressure Chemical Ionization and Electrophoretic Separation Capabilities. *Anal Chem*. 2019;91(18):11562-11568. doi:10.1021/acs.analchem.9b01456

43. McClory PJ, Håkansson K. Corona Discharge Suppression in Negative Ion Mode Nanoelectrospray Ionization via Trifluoroethanol Addition. *Anal Chem*. 2017;89(19):10188-10193. doi:10.1021/acs.analchem.7b01225

44. Page JS, Marginean I, Baker ES, Kelly RT, Tang K, Smith RD. Biases in ion transmission through an electrospray ionization-mass spectrometry capillary inlet. *J Am Soc Mass Spectrom*. 2009;20(12):2265-2272. doi:10.1016/j.jasms.2009.08.018

45. Wu C, Wang Q, Chen H, Li M. Rapid quantitative analysis and suspect screening of per- and polyfluorinated alkyl substances (PFASs) in aqueous film-forming foams (AFFFs) and municipal wastewater samples by Nano-ESI-HRMS. *Water Research*. 2022;219:118542. doi:10.1016/j.watres.2022.118542

46. Development O of R&. Method 537.1: Determination of Selected Per- and Polyfluorinated Alkyl Substances in Drinking Water by Solid Phase Extraction and Liquid Chromatography/Tandem Mass Spectrometry (LC/MS/MS). Accessed December 8, 2022. https://cfpub.epa.gov/si/si_public_record_Report.cfm?dirEntryId=343042&Lab=NERL

47. Zhang W, Ren Y, Lin Z, Ouyang Z. High-Precision Quantitation of Biofluid Samples Using Direct Mass Spectrometry Analysis. *Anal Chem*. 2019;91(11):6986-6990. doi:10.1021/acs.analchem.9b01694

48. Wang J, Shi Y, Cai Y. A highly selective dispersive liquid–liquid microextraction approach based on the unique fluorous affinity for the extraction and detection of per- and polyfluoroalkyl substances coupled with high performance liquid chromatography tandem–mass spectrometry. *Journal of Chromatography A*. 2018;1544:1-7. doi:10.1016/j.chroma.2018.02.047

49. Zgoła-Grześkowiak A, Grześkowiak T. Dispersive liquid-liquid microextraction. *TrAC Trends in Analytical Chemistry*. 2011;30(9):1382-1399. doi:10.1016/j.trac.2011.04.014

50. Vela-Soria F, García-Villanova J, Mustieles V, de Haro T, Antignac JP, Fernandez MF. Assessment of perfluoroalkyl substances in placenta by coupling salt assisted liquid-liquid extraction with dispersive liquid-liquid microextraction prior to liquid chromatography-tandem mass spectrometry. *Talanta*. 2021;221:121577. doi:10.1016/j.talanta.2020.121577

51. N.H. Tests Find PFAS Chemicals In Bottled Water Brands Sourced From Mass. Spring. New Hampshire Public Radio. Published July 30, 2019. Accessed November 8, 2022. https://www.nhpr.org/post/nh-tests-find-pfas-chemicals-bottled-water-brands-sourced-mass-spring

52. Li L, Chen TC, Ren Y, Hendricks PI, Cooks RG, Ouyang Z. Mini 12, Miniature Mass Spectrometer for Clinical and Other Applications—Introduction and Characterization. *Anal Chem*. 2014;86(6):2909-2916. doi:10.1021/ac403766c

53. Li Y, Emge TJ, Moreno-Vicente A, et al. Unexpected Formation of Metallofulleroids from Multicomponent Reactions, with Crystallographic and Computational Studies of the Cluster Motion. *Angewandte Chemie*. 2021;133(48):25473-25477. doi:10.1002/ange.202110881

.

6.7 Supporting information

6.7.1 Calculate the intensity ratio between analyte and IS using R codes

```
Library(rawrr)
trimmed.mean = function(v,prop.trim=0.1) {
  q1 = quantile(v, prob=prop.trim/2)
  q2 = quantile(v, prob=1-prop.trim/2)
  output = mean(v[q1 <= v & v <= q2])
  return(output)
}
Ratio_A_IS <- function(df,ms1=94,ms2=499){
  ms1.intensity <- rawrr::readChromatogram(df,mass = ms1,tol=100)[[1]][['intensities']]
  ms2.intensity <- rawrr::readChromatogram(df,mass = ms2,tol=100)[[1]][['intensities']]
  n <- length(ms1.intensity)
  n <- length(ms2.intensity)
  k=floor(n/3)
  R.ms1.ms2.1 = ms1.intensity[1:k]/ms2.intensity[1:k]
  R.ms1.ms2.2 = ms1.intensity[k:(2*k)]/ms2.intensity[k:(2*k)]
  R.ms1.ms2.3 = ms1.intensity[(2*k):(3*k)]/ms2.intensity[(2*k):(3*k)]
  output = list('file'=df,'#scan'=n,'Ratio.mean.1'= trimmed.mean(R.ms1.ms2.1,prop.trim =
0.1),'Ratio.mean.2'= trimmed.mean(R.ms1.ms2.2,prop.trim = 0.1),'Ratio.mean.3'=
trimmed.mean(R.ms1.ms2.3,prop.trim = 0.1))
  return(output)
}
```

6.7.2 Calculate the SNR using R codes

The *m/z* values and their corresponding signal intensities should be imported and saved as a .csv file before the calculations.

```
SNR.medium <- function(df,mz1=395,mz2=405,mz3=399){
  df=data.frame(sapply(df,as.numeric))
  df.sub <- subset(df,df[,1]>mz1&df[,1]<mz2)
  signal <- as.numeric(max(subset(df,df[,1]>(mz3-1)&df[,1]<(mz3+1))[,2]))
  noise <- unname(summary(as.numeric(df.sub[,2]))[3])
  SNR = signal/noise
  output <- list('SNR'=SNR,'Signal'=signal,'noise'=noise,plot =
plot(df.sub[,1],df.sub[,2],type='l',xlab='m/z',ylab='Intensity'),quantile =
boxplot(as.numeric(df.sub[,2])))
  return(output)
}
```

7 Charge State Distributions of Proteins in Femto-Ampere ESI under Different pH

7.1 Introduction

Electrospray ionization, developed by Fenn in 1984, is a highly sensitive and informative method for characterizing protein structure coupling with mass spectrometry,[1,2] especially when combined with ion mobility mass spectrometry,[3–5] and is a faster alternative to crystallography.

It is widely accepted that proteins exhibiting a distinct difference in their charge state distribution which reflects their solution conformations,[6] with the native form having fewer charges via a charge residue pathway and the denatured form having more charges due to additional protonation sites available through a charge ejection pathway. [7,8] Besides the inherent protein conformations, the charge state distributions are influenced by factor, including spray tip emitter, [9,10] flow rates, [11] spray solvents,[12] and instrumental parameters. [13,14]

There still exists debate regarding whether the gas phase retains the solution phase structure. Meanwhile many researchers demonstrated that ESI undergoes a acidification journey from the electrooxidation at electrode/solution interface[15,16] to the droplet shrinkage.[17] To reveal the underlying mechanisms and fulfill applications purposes, a variety of methods have been developed to manipulate the charge states of proteins produced by ESI, including adding supercharging agents,[18] performing chemical derivation, [19] and changing buffer cations.[20]

Recently, a novel method called Femtoampere electrospray (femtoESI) has been developed. This technique is conducted at ultra-low (fA to pA) ionization currents with flow rates at fL/min to low pL/min ranges.[21,22] In this work, model protein ions produced by Femtoampere ESI under a series of pH conditions were studied. By comparing the results with those obtained by

conventional nanoESI, the evolution history for charged droplets produced by femtoESI was deduced, revealing the ESI mechanism better.

7.2 Experimental

7.2.1 Chemicals

Cytochrome c from equine heart (C7752), ubiquitin from bovine erythrocytes (U6253), and lysozyme from chicken egg white (L6876) were purchased from Sigma Aldrich (St. Louis, MO). HPLC grade water (JT4218-03) was from Avantor Performance Materials, LLC (Radnor, PA). Formic acid (98%-100% for LC-MS LiChropur®) was purchased from EMD Millipore Corporation (Billerica, MA).

The stock solutions at concentrations of 1 mM were prepared by dissolving weighed powders into water and stored at -20 °C prior to use. The pH of solutions was adjusted by adding formic acid based on Henderson-Hasselbalch equation, using the pKa of formic acid (3.75). The pH was confirmed using pH strips purchased from Millipore-Sigma (Burlington, MA). 10 µM protein samples at desired pH were obtained by a 100-fold dilution of stock solutions. This dilution ensured that the percentage of formic acid in the samples remained almost unchanged, thereby maintaining a constant pH.

7.2.2 Nanoampere ESI and Femtoampere ESI mass spectrometric analysis

The borosilicate glass emitters (O.D. 0.86 mm, w/ filament) purchased from Sutter Instruments (Novato, CA) were pulled using a Model P-1000 micropipette puller (Sutter Instruments, Novato, CA) into tips with an outer diameter (O.D.) of 3.5 ± 0.5 µm. Subsequently, 3-10 µL of the samples was loaded into the glass emitters using a micropipette (Eppendorf, Humburg, Germany). A gold wire (O.D. 0.1 mm) purchased from Fisher Scientific (Hampton, NH) was inserted into the capillary to establish contact with the solution. The distance between

emitter tips and MS inlet was 2 mm. In nanoampere ESI mode, the spray voltage ranged between 1.2 and 1.5 kV. In contrast, the spray voltage was carefully regulated to fall between 0.7 and 0.9 kV for the femtoampere mode. The onset of femtoampere mode was indicated by a decrease in ion intensity (NL: 1-10) so that the maximum injection time reached 1000-8000 ms with the auto gain control (AGC) was set to 3e4. Based on Allen et al.'s study, which indicates that multiple spraying modes may exist under certain conditions in femtoampere mode, we monitored the TIC and ACS at each scan (**Figure S 7-1**). To ensure the reliability of our results, all mass spectra acquired in this study were filtered based on the TIC. Specifically, spectra with a TIC lower than 100 were discarded.

All the measurements were carried on an LTQ-XL mass spectrometer (Thermo Fisher Scientific, San Jose, CA) with the following instrumental parameters for protein analytes: inlet temperature of 150-200 ˚C, high mass scan range (150-4000), microscan set to 1, inlet capillary voltage 46 V, and tube lens voltage 60 V. The in-source ion dissociation (SID) was set to 100 V to reduce the dimeric species. (**Figure S 7-2**)

7.2.3 Data Process

The ACSs (average charge state) of each distribution in the mass spectra were processed using R programing language, an open-source statistical tool. The raw data was directly accessed using the "rawrr" package developed by Kockmann and Panse. [23] After importing the data set (either single scan or an average of multiple scans) into the environment, a custom R function (**Equation 7-1**) was written to automatically calculate the ACS, where the I_{zi} represents the intensity of a given charge state z_i. The "ggplot" package was utilized for data visualization.

$$Z_{av} = \frac{\sum z_i I_{zi}}{\sum I_{zi}}$$

Equation 7-1

The low charge states ions ranging from +6 through to +9 were assigned to the folded cytochrome c, while the remaining charge states were associated with unfolded cytochrome c. Thus, the fraction of folded cytochrome c was calculated using **Equation 7-2**, where *I* is the peak intensity of the relevant cytochrome c ion. [14]

$$Fraction_{folded} = \frac{\sum_{i=6}^{i=9} I_i}{\sum I_i} \times 100\%$$

Equation 7-2

The folded fraction % of cytochrome as a function of pH was fitted using a four- parameter Sigmoid function with R package "drc". The quality of the fit was evaluated by the residual standard error. All the R functions used in this study were listed in the supporting information (7.8.3-7.8.5).

7.3 Results and Discussions

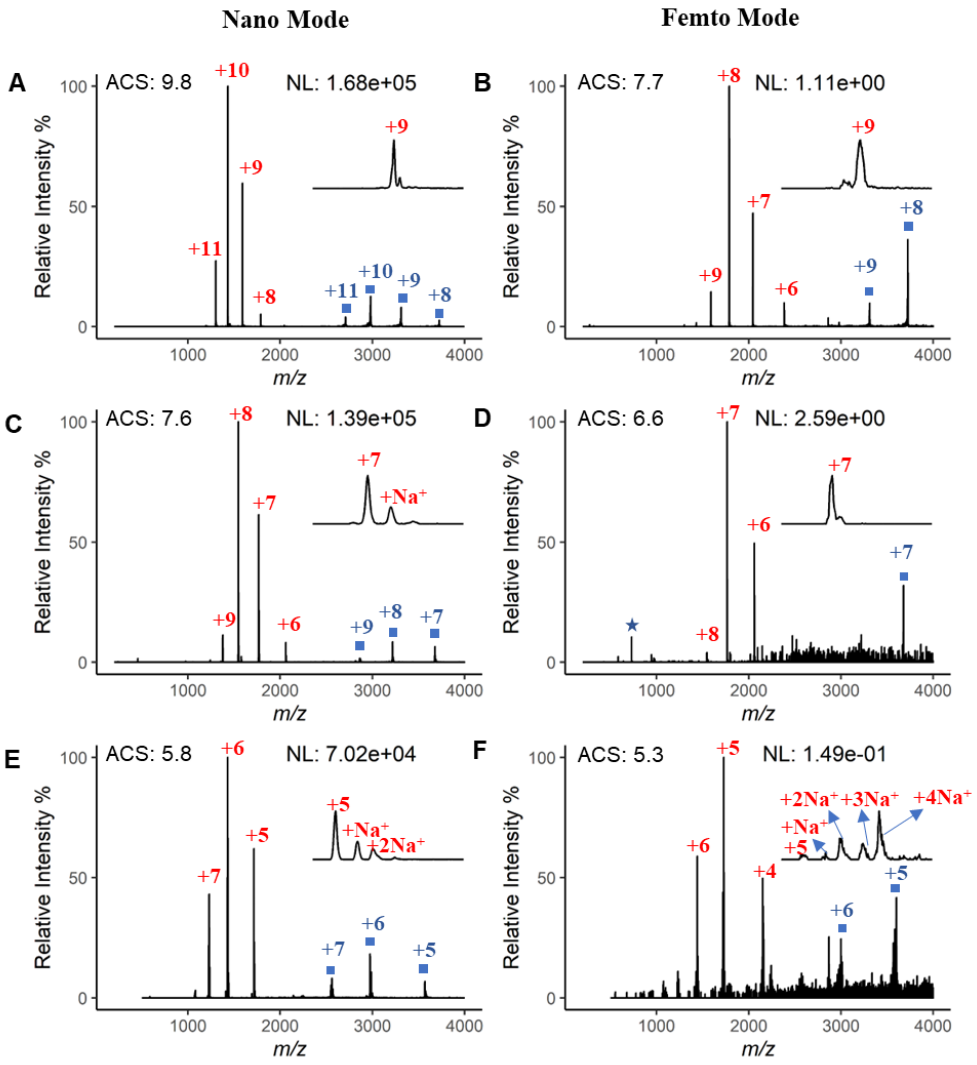

Figure 7-1. Comparison of average charge states (ACS) between nanoampere mode and femtoampere mode with the same protein standards. A) Mass spectrum of 10 µM lysozyme in pure water acquired in the nanoampere mode; B) Mass spectrum of 10 µM lysozyme in pure water acquired in the femtoampere mode; C) Mass spectrum of 10 µM Cytochrome C in pure water acquired in the nanoampere mode; D) Mass spectrum of 10 µM Cytochrome C in pure water acquired in the femtoampere e mode; E) Mass spectrum of 10 µM ubiquitin in pure water acquired in the nanoampere mode; F) Mass spectrum of 10 µM ubiquitin in pure water acquired in the femtoampere mode. The mass spectra are an average of 10 scans. The blue filled squares represent dimer species. The star in D represents a fragment from cytochrome c (elucidation shown in **Supporting information 7.8.6**).

7.3.1 nanoampere mode versus femtoampere mode

Both femtoampere mode and nanoampere mode can be achieved using a typical nanoESI source with glass emitter of tip diameter of 3-4 μm. By lowering the voltage to a few hundreds of volts, nanoampere mode was able to switch to the femtoampere mode, which featured Femto-Pico A spray currents. [21,22] As depicted in **Figure 7-1**, the same proteins dissolved in pure water and analyzed on the LTQ, demonstrated a signal intensity of 1.68e5 for lysozyme in the nanoampere ESI mode, which decreased to 1.11 in femtoampere ESI mode. Similarly, the signal intensity of cytochrome c decreased from 1.39e5 to 2.59. Furthermore, for ubiquitin, the signal intensity decreased from 7.02e4 to 0.15. It was obvious that the total ion currents (TIC) rapidly decrease by at least four orders of magnitude with switching to femtoampere mode.

In addition to the point at which the total ion currents (TIC) rapidly decreased, the average charge state (ACS) in the nano mode consistently shifted towards to lower values with switching to femtoampere mode. In the case of lysozyme, the +10 charged species dominated in the nano mode, whereas the femtoampere mode mass spectrum was dominated by +8 charged ions, resulting in a shift of ACS from 9.8 to 7.7 by 2 charge units. The trend remained the same for cytochrome c, but the ACS shift was much lessened. **Figure 7-1 C** showed that the main charge state of cytochrome c in nano ESI was +8, which is consistent with that obtained by other research groups with the regular nanoESI setups. [24,25] In the femtoampere mode, the peak corresponding to cytochrome c +7 ions was very strong. The ubiquitin results (**Figure 7-1 E and F**) echoed the charge state distributions of lysozyme and cytochrome c, with the nanoampere mode producing higher ACS values relative to the femtoampere mode. These observations further suggest that the extent of ACS shift appears to be protein dependent. With the highest pI value, lysozyme (MW = 14307, pI = 11.1) has a 2-charge unit ACS shift. Next, cytochrome c (MW = 12362, pI = 9.6) shifts

1 charge unit from 7.6 to 6.6. A lower degree of ACS shift from 5.8 to 5.3 by 0.5-charge unit is seen in ubiquitin (MW = 8568, pI = 6.8).

The extent of sodium adduction in the femtoampere and nanoampere modes was another observation of interest. In the case of lysozyme, neither the femtoampere nor the nanoampere mode mass spectrum exhibited any sodium adductions. A small portion of sodiated cytochrome c +7 ions was observed in the nano mode, whereas no sodium incorporation was detected in the femtoampere mode. The case of ubiquitin was unique, with significant and extensive sodium incorporation in femtoampere mode. As shown in **Figure 7-1 F**, only 0.4% of ubiquitin +5 ions did not have sodium cation incorporated. The degree of sodiation on the three proteins appeared to be independent of the sodium and hydronium ion concentrations in the solution but rather depended more on the protein's properties. It seemed that sodium ion incorporation was more extensive in acidic proteins than basic proteins, although the trend was subtle. It was worth noting that HPLC grade water was used throughout the study, and no sodium was deliberately added to the solution.

Finally, protein dimerization was observed in both nanoampere mode and femtoampere mode. The ESIprot tool developed by Robert Winkler was used to calculate the molecular weights of these dimer species, [26] which are summarized in **Table S7-1**. The deconvolution of the lysozyme dimeric ions yielded a molecular weight of 29,795 Da, which corresponds to an adduct mass of 1,181 Da. For cytochrome c and ubiquitin, the adduct masses were 1,018 Da and 706 Da, respectively. Plotting the adduct mass against the molecular weight of the protein resulted in a linear regression with an R^2 value of 1 (**Figure S7-5**). Dugan and Bier also identified a mass of 474 Da adduct for insulin (MW=5,734) in their mechanospray ionization MS. [27] Interestingly, this data point fits ideally into the linear regression equation (**Figure S7-5**). Although it is still unclear

why a perfect linear relationship exists between the adduct mass and the protein's molar mass for these dimeric species, it is evident that the dimer-like species were produced during the electrospray process since ubiquitin and cytochrome c exist as monomers in the solution phase. [28] Thus, this linear relationship can be potentially used to rule out nonspecific dimerization species in native MS analysis.

7.3.2 Influence of spray voltage on ACS

The impact of spray voltage was examined using ubiquitin, an exceptionally stable protein, as a model system since lowering the spray voltage is necessary to achieve femtoampere mode. The mass spectra of ubiquitin in a pH 2.7 aqueous solution are displayed in **Figure 7-2**, with the dominant peak being the +7 charged ion in an acidic environment, consistent with the observations of Pan et al. [29] regarding the shift of ubiquitin's charge state distribution to a lower state in more acidic aqueous solutions. Increasing the spray voltage from 1.2 kV to 2.5 kV did not significantly alter the charge state distribution of ubiquitin. This observation aligns with the observations made by Peng et al. that a range of DC voltages spanning from 2.0 kV to 4.0 kV did not induce modifications to the charge state distribution of peptides. [30].

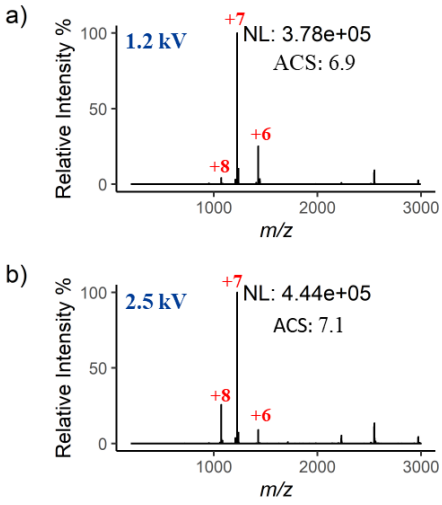

Figure 7-2. Mass spectra of 10 µM aqueous ubiquitin solution containing 0.22% (v/v) formic acid against spray voltages. a) 1.2 kV; b) 2.5 kV. The mass spectra were an average of 10 scans.

7.3.3 Influence of spray currents on ACS

The impact of spray current on the charge state distribution was investigated as well. Allen et al. conducted research on the reduction of spray currents by introducing a high resistor, with values of up to 10 TΩ, into the ESI circuit, as described in the manuscript "Giga-ohm and Tera-ohm Resistors in femtoampere and picoampere Electrospray Ionization." In **Figure 7-3**, it was evident that when the resistor was increased from 100 MΩ to 1 TΩ, the absolute signal intensity of the dominant +7 ubiquitin ion decreased by almost two orders of magnitude, which suggests a decline in the spray currents as well. While no notable ACS shifts were observed following the reduction of the spray currents. Therefore, it can be inferred that the femtoampere mode is not a direct outcome of modifications in the spray current and voltage, despite being a derivative of the nano mode through a decrease in spray voltage, and so are the ACS shifts. Although in a recent study by Han and Chen, [31] the ACS of ubiquitin in acidic aqueous solution increased when the spray current was low, this shift was mainly due to the increasing of a higher charge state series of

unfolded ubiquitin. Notably, the charge state distribution of ubiquitin remained constant within the 60-400 nanoampere range throughout the study. This finding supported our conclusion that the charge state distribution of proteins was unaltered by variations in spray current in the nanoampere range.

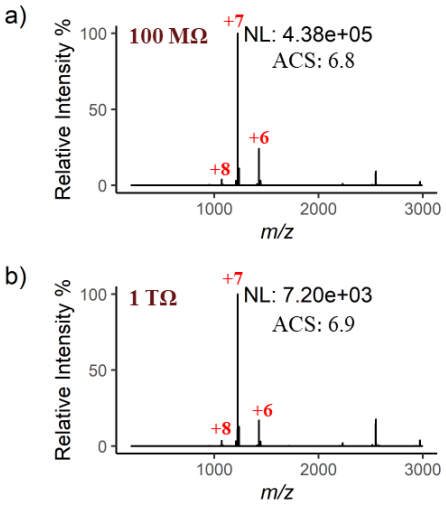

Figure 7-3. Mass spectra of 10 µM aqueous ubiquitin solution containing 0.22% (v/v) formic acid a) a 100-MΩ resister; b) a 1 TΩ resistors was connected into the ESI circuit in order to limit the spray currents. The mass spectra are an average of 10 scans.

7.3.4 Acidification in ESI

The size of the emitter tip represents a crucial physical parameter that can impact the charge state distribution. Yuill et al. demonstrated that a higher and narrower charge state distribution was observed in nanometer emitters compared to micrometer emitters, owing to the higher charge densities on the small initial droplets.[9,32] On the other hand, Mortensen and Williams proposed that the columbic interaction between the glass surface and the charged protein may lead to the unfolding of proteins, resulting in a higher charge state shift. [24] Nonetheless, in our study, the influence of tip size was eliminated as we utilized the same micrometer emitter tip throughout each comparison.

After minimizing the influence of physical parameters, we redirected our focus towards the chemical environment changes that occur during the ESI process. In previous studies investigating the charge state distribution of proteins, pH and buffer type were found to be critical determinants of the fine pattern of charge state distributions. [5,29,31] Specifically, the charge state distribution shifted towards higher values at lower pH, while the use of ammonium acetate buffer led to a lower ACS relative to pure water. Thus, it can be inferred that femtoampere mode is less acidic than nanoampere mode due to its lower ACS. Additional evidence supporting this inference was the extensive sodium adductions of ubiquitin observed in pure water (pH = 5.4) in femtoampere mode (**Figure 7-1 F**), which was comparable to the mass spectrum of ubiquitin obtained from a pH = 8 buffer solution in the study by Pan et al. [16] It is well-established that the pH changes during the ESI process can be attributed to two main factors: electrooxidation at the electrode/solution interface [16,33] and the droplet shrinkage on the fly. [17,34] Therefore, if the ACS shifts of proteins are caused by a greater degree of acidification in nanoampere mode than in femtoampere mode, we would expect to obtain the same charge state distributions in femtoampere mode as those in nanoampere mode by adding acids into the solutions.

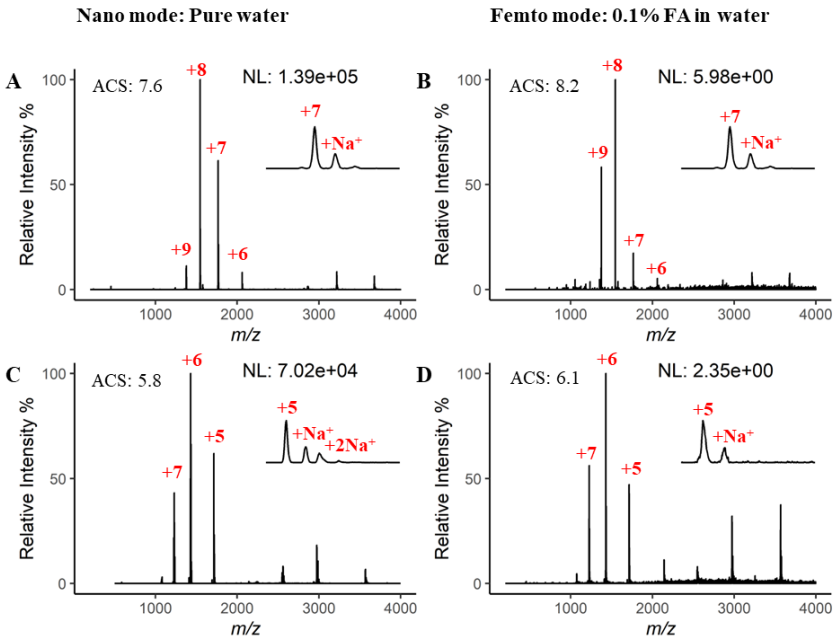

Figure 7-4. Comparison of mass spectra acquired in nanoampere mode A and C:10 µM cytochrome and ubiquitin in pure water, respectively and in femtoampere mode B and D:10 µM cytochrome and ubiquitin in water containing 0.1% FA. Each mass spectrum was an average of 10 scans.

As we expected, upon the addition of formic acid up to 0.1% to the pure water, the ACS of cytochrome c in femtoampere mode increased to 8.2, **Figure 7-4 A and B**. This value was comparable to the ACS value obtained in nanoampere mode with cytochrome c dissolved in pure water. The same trend was observed for ubiquitin. Furthermore, the sodium adductions in femtoampere mode became similar to those in nanoampere mode (Inserted **Figure 7-4 C and D**). Additionally, Allen et al. demonstrated that the charge state distribution of cytochrome c in pure water was similar to the charge state distribution in nanoampere mode but acquired in a 200 mM ammonium acetate buffer solution, providing evidence for less acidification in femtoampere ESI mode. Since Feng et al. showed the weak acid anions at 5 mM had litter impact on the charge state of proteins,[35] the H^+ concentration change was the only factor affecting the charge state. The pH of pure water and 0.1% formic acid were measured to be 5.4 and 2.7, respectively. If femtoampere

exerts less pH changes during the ESI process, we can infer that the nanoESI process causes proteins to experience a 2.7 pH unit more acidic environment.

7.3.5 Cytochrome c unfolding behavior in femtoampere mode.

Both nanoampere mode and femtoampere mode mass spectra of cytochrome c were acquired by electrospraying aqueous solutions across a range of pH values (from 2.0 to 3.2) at which cytochrome c is known to undergo conformational changes. The resulting spectra are depicted in **Figure 7-5**. In nanoampere mode, two distinct charge state distributions were observed: one centered at +8, corresponding to the globular protein, and the other centered at +14 and +15, corresponding to the unfolded cytochrome c. The results support a highly cooperative unfolding process which behaves in a "all or none" way with non-existence of partial folded states.[36,37]. The midpoint was acquired by fitting the % folded protein against pH to a Sigmoid function (**Figure 7-6**) and was estimated to be 2.45, which is consistent with Konermann's study. [36]. The maximum charge state of unfolded cytochrome c (+15 here vs. 16+) was about 1 charge unit off. It might be due to the differences in experimental conditions such as flow rate (140 nl/min here vs. 5 µL/min) and solvents (pure water here vs. 3% methanol in water).

In addition to the peaks centering at +8 and +9, which correspond to the folded conformer. the femtoampere mode mass spectra revealed a new charge state distribution consisting of distinct peaks centered at +11 and 12+ (**Figure 7-6 e and j**) This distribution emerged as the solution became more acidic, suggesting that it corresponds to a partially-folded intermediate state, as Grandori has previously reported that cytochrome c intermediates have charge distributions between those of the unfolded and folded states[38]. However, at pH = 2.0, where the unfolded state is expected to be dominant, this new distribution remained the major one, with no corresponding observed for the unfolded one. Based on Goto et al.'s study, who estimated the accumulation of

the folding intermediate to be around 25% by titration.[39] We infer that the new charge state distribution observed in femtoampere mode corresponds to the unfolded cytochrome c, and the overall shift towards lower charge state is likely due to the limited available charge on the droplet surface through a chain ejection pathway[7]. So, if the intensities of the peaks +6 through +9 arise from folded cytochrome c, while the others represent the unfolded cytochrome c, the estimated % folded protein agrees with that obtained in the nanoampere mode. The fitting results showed that the mid-point was 2.34 (**Figure 7-6**), with a deviation of ~0.2 units that may be attributed to the simplifying assumption that the +9 ions represent folded cytochrome c, while there may be an overlap between the folded protein envelope and the unfolded protein envelope.

Consequently, the unfolding behavior of cytochrome c in femtoampere mode was comparable to that in nanoampere mode, albeit producing a lower charge state distribution for the unfolded form. However, the folded forms of cytochrome c displayed a distribution centered at +8 ion in both femtoampere and nanoampere modes when the concentrations of formic acid were 0.1% and 0.2%, (**Figure 7-5 c,d,e,f**).

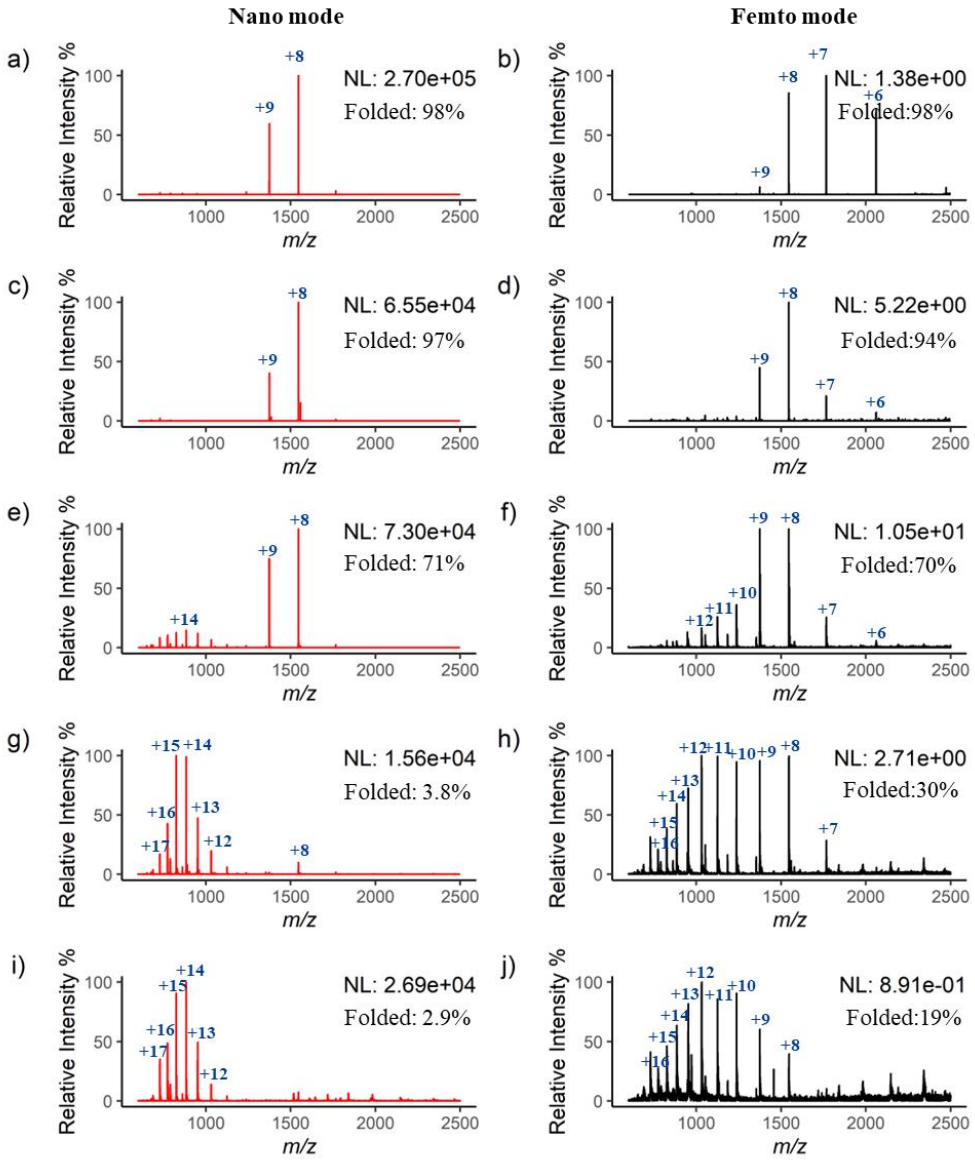

Figure 7-5. Comparison of pH-dependent unfolding of 10 µM cytochrome c between nanoampere mode and femtoampere mode: a) and b) pH=3.2 (0.011% formic acid) c) and d): pH=2.7(0.11% formic acid); e) and f) pH=2.5 (0.22% formic acid); g) and h) pH=2.1 (1.1% formic acid); i) and j) pH=2.0 (2.2% formic acid) in aqueous solutions. Each mass spectrum is an average of 10 scans. The folded proteins correspond to the sum of peak intensities of +6, +7, +8, and +9 charged ions.

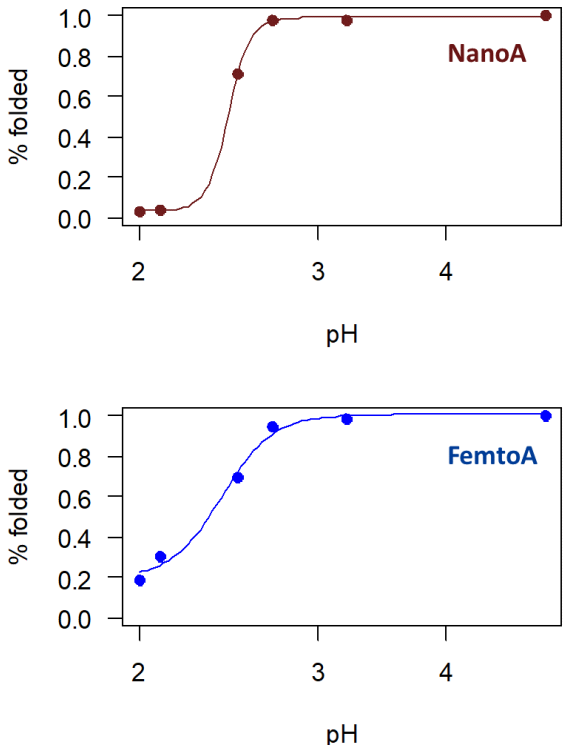

Figure 7-6. The fitting curves of % folded cytochrome c as a function of pH through a sigmodal distribution. The residual standard error values for nanoampere and femtoampere fitting were 0.012 and 0.053, respectively, suggesting that the sigmoid function is a suitable fit model for the data. Based on the sigmoid fitting curves, the pH values at which the folded cytochrome c fraction was 50% were determined to be 2.45 and 2.34 for nanoampere and femtoampere modes, respectively.

7.3.6 Underlying mechanisms of proteins experiencing a less acidic environment in femtoampere mode

Based on previous studies by Van Berkel et al. and Konermann et al. [15,16], we compared the maximum pH change (**Equation 7-3**) between nanoampere mode and femtoampere mode, utilizing the flow rates and currents obtained in our previous research. Our findings, presented in **Table 7-1**, indicate that the degree of pH change in femtoampere mode was lower compared to that observed in nanoampere mode. It is important to note that the **Equation 7-3** predicts the maximum pH change under the assumption that the electrolytic oxidation of water is the only charge-balancing reaction, and the actual pH change is smaller than that value. It seems plausible to observe a smaller pH change in femtoampere mode than that in the nanoampere mode. However, the folded forms of cytochrome c observed in aqueous solution (pH 5.4 and pH 3.2, **Figure 7-1C and Figure 7-5 a**) in both nanoampere mode and femtoampere mode does not support this explanation, at least not as the major reason. This observation is also consistent with Konermann's work, which suggests that the acidification resulted from the electrochemical oxidation occurs under specific conditions. [16]

$$\Delta pH = -\log 10 \left({}^{I_{spray}}\!/_{nFv} \right) - pH_{initial}$$

Equation 7-3

where n = 1, F = 96485 C/mole, and v is the flow rate of the solution

Table 7-1 The estimated pH changes in nanoampere mode and femtoampere mode. The measured pH of pure water is 5.4.

Spray Mode	Flow rate	Spray current	ΔpH
nanoampere	140 nanoL/min [40]	40 nA [21]	-1.7
femtoampere	7.7 picoL/min	0.22 pA [22]	-0.6

Moreover, the consistency of the pH-induced unfolding behavior of cytochrome c observed in both nanoampere mode and femtoampere mode rules out the electrolytic oxidation of water at the electrode/liquid interface, as this reaction would have a strong impact on the protein unfolding behavior. Instead, we propose that the acidification during droplet shrinkage and the consecutive fission events. According to Zhou et al's study,[17] the maximum proton changes from pre-sprayed solution to 2 mm distance from the emitter tip could be one pH unit. The preconcentration effect is believed to be more pronounced in smaller droplets. As the spray plume in femtoampere mode was not observable by our optical setup,[21,40] we made the assumption that the initial droplet radius in nanoampere mode and femtoampere mode were 2 µm and 200 nm, respectively. Using Kaberle and Tang's model, which assumes evaporation occurs at the surface limit [41], as shown in **Equation 7-4**, we found that if the flying time of droplets was 10 µs (with a droplet velocity of approximately 25 m/s and an emitter-inlet distance of 2 mm), the volume of the droplets decreases by 98% and 86% for the 2 us and 200 um radius droplets. Therefore, the lessened acidification observed in femtoampere mode, which is believed to have a smaller initial charged droplet size, cannot be primarily attributed to droplet shrinkage.

$$\frac{dR}{dt} = -\frac{\alpha v \rho^o \mathrm{M}}{4\rho R_g T}$$

$$R = R_0 - 9.8^{-5}t$$

where ρ^o is the vapor pressure of water (2.30e3 Pa), v is the average thermal velocity of water vapor molecules (5.85e2 m/s^2), α is the condensation coefficient and equals to 0.04. R_g and T are the gas constant and temperature in degree kelvin. T = 298 K. ρ is the water density and equals to 1.0e3 kg/m^3. M is water molar mass and equals to 0.018 kg/mole. R_0 is the initial droplet radius.

Equation 7-4

As such, we hypothesize the disintegration process of droplets after the shrinkage of initial droplets reaching to the Rayleigh limit radius, which may be associated with the preconcentration of proton inside the droplets, could be a contributing factor to the observed phenomenon. As the

child droplets are created by solvent evaporation and releasing of the surface charges through either ion evaporation or field emission pathways, resulting in the disintegration of parent droplets. Assuming that each fission event results in a loss of 30% of the charge and 2% of the mass of the large droplet,[42-43] the volume loss would be 51% ($1-0.7^2$), as shown in **Equation 7-5**. As a result, the concentration of acids within droplets increases by an order of magnitude (-1 pH unit) after 3-4 fission events (1.9^3~1.9^4, **Equation 7.6**). Since the lower charge state distribution of unfolded cytochrome c observed in the femtoampere mode suggests the presence of small, initially charged droplets with less available excess charge on the droplet surface compared to nanoampere mode. Thus, the observed pH resistance in the femtoampere mode may be contributed to the fewer fission events. However, it is difficult to estimate the exact number of fission events in the femtoampere mode accurately since the charge and mass loss may not be constant. The kinetics of cytochrome c unfolding may explain why the relative intensities of two charge state distributions did not change in the fission events. This is because acid-induced cytochrome c unfolding occurs within the droplet, which takes microseconds, [24 44] as opposed to the loss of water molecules covering the protein, which occurs within nanoseconds. [45]

$$q = 8\pi\sqrt{\epsilon\gamma R^3}$$

$$q^2 \propto V$$

Equation 7-5

Where q is Rayleigh charge, ϵ is permittivity of vacuum, γ is the surface tension of the solution, and R is the Rayleigh radius. V is the corresponding volume when the droplet is at Rayleigh limit radius.

$$\frac{C_{n+1}}{C_n} = \frac{\frac{m_{n+1}}{V_{n+1}}}{\frac{m_n}{V_n}} = \frac{\frac{m_{n+1}}{m_n}}{\frac{V_{n+1}}{V_n}} = \frac{0.98}{0.51} = 1.9$$

Equation 7-6

Concentration changes after each fission event, where n+1 represents one additional fission event compared to n.

7.4 Conclusions

The signal intensities of proteins (lysozyme, cytochrome c, and ubiquitin) were observed to be 4 orders of magnitude lower in femtoampere mode compared to nanoampere mode. Meanwhile, the average charge state (ACS) of proteins in femtoampere mode was about 1-2 charge state less than that in the nano mode when otherwise constant conditions. Interestingly, the addition of 0.1% formic acid into solution in femtoampere mode could increase the ACS of proteins to the same level as that in nanoampere mode, indicating proteins experience a pH 2.7 units less acidic environment relative to the nanoampere mode in the ESI process. To investigate the underlying mechanism, cytochrome c was monitored in both nanoampere mode and femtoampere mode, since it is known to undergo unfolding behavior in different pH solutions. The unfolded cytochrome c showed a charge state distribution centered at +12, which was lower (+15) than that obtained in nanoampere mode. In contrast, the folding cytochrome c showed the same charge state distribution as that in nanoampere mode with formic acid over 0.1%, suggesting different pathways of ion formation in the electrospray process.

To elucidate the underlying mechanism of femtoampere mode's resistance to pH change, three factors were taken into consideration: electrooxidation at the electrode/solution interface, droplet shrinkage on the fly, and fission events. A careful examination of the three factors implies that less fission event in the femtoampere mode may contribute to the low charge state distribution of proteins in pure water compared to that of the nanoampere mode.

7.5 References

(1) Dobo, A.; Kaltashov, I. A. Detection of Multiple Protein Conformational Ensembles in Solution via Deconvolution of Charge-State Distributions in ESI MS. *Anal. Chem.* **2001**, *73* (20), 4763–4773. https://doi.org/10.1021/ac010713f.

(2) Kuprowski, M. C.; Konermann, L. Signal Response of Coexisting Protein Conformers in Electrospray Mass Spectrometry. *Anal. Chem.* **2007**, *79* (6), 2499–2506. https://doi.org/10.1021/ac0620056.

(3) Smith, D. P.; Giles, K.; Bateman, R. H.; Radford, S. E.; Ashcroft, A. E. Monitoring Copopulated Conformational States during Protein Folding Events Using Electrospray Ionization-Ion Mobility Spectrometry-Mass Spectrometry. *J. Am. Soc. Mass Spectrom.* **2007**, *18* (12), 2180–2190. https://doi.org/10.1016/j.jasms.2007.09.017.

(4) Purves, R. W.; Barnett, D. A.; Guevremont, R. Separation of Protein Conformers Using Electrospray-High Field Asymmetric Waveform Ion Mobility Spectrometry-Mass Spectrometry. *International Journal of Mass Spectrometry* **2000**, *197* (1), 163–177. https://doi.org/10.1016/S1387-3806(99)00240-7.

(5) Susa, A. C.; Xia, Z.; Tang, H. Y. H.; Tainer, J. A.; Williams, E. R. Charging of Proteins in Native Mass Spectrometry. *J. Am. Soc. Mass Spectrom.* **2017**, *28* (2), 332–340. https://doi.org/10.1007/s13361-016-1517-7.

(6) Chowdhury, S. K.; Katta, V.; Chait, B. T. Probing Conformational Changes in Proteins by Mass Spectrometry. *J. Am. Chem. Soc.* **1990**, *112* (24), 9012–9013. https://doi.org/10.1021/ja00180a074.

(7) Konermann, L.; Ahadi, E.; Rodriguez, A. D.; Vahidi, S. Unraveling the Mechanism of Electrospray Ionization. *Anal. Chem.* **2013**, *85* (1), 2–9. https://doi.org/10.1021/ac302789c.

(8) Hall, Z.; Robinson, C. V. Do Charge State Signatures Guarantee Protein Conformations? *J. Am. Soc. Mass Spectrom.* **2012**, *23* (7), 1161–1168. https://doi.org/10.1007/s13361-012-0393-z.

(9) Li, Y.; Cole, R. B. Shifts in Peptide and Protein Charge State Distributions with Varying Spray Tip Orifice Diameter in Nanoelectrospray Fourier Transform Ion Cyclotron Resonance Mass Spectrometry. *Anal Chem* **2003**, *75* (21), 5739–5746. https://doi.org/10.1021/ac0301402.

(10) Xia, Z.; Williams, E. R. Effect of Droplet Lifetime on Where Ions Are Formed in Electrospray Ionization. *Analyst* **2018**, *144* (1), 237–248. https://doi.org/10.1039/C8AN01824C.

(11) Prabhu, G. R. D.; Ponnusamy, V. K.; Witek, H. A.; Urban, P. L. Sample Flow Rate Scan in Electrospray Ionization Mass Spectrometry Reveals Alterations in Protein Charge State Distribution. *Analytical Chemistry* **2020**. https://doi.org/10.1021/acs.analchem.0c01945.

(12) Iavarone, A. T.; Jurchen, J. C.; Williams, E. R. Effects of Solvent on the Maximum Charge State and Charge State Distribution of Protein Ions Produced by Electrospray Ionization. *J. Am. Soc. Spectrom.* **2000**, *11* (11), 976–985. https://doi.org/10.1016/S1044-0305(00)00169-0.

(13) Schmidt, A.; Bahr, U.; Karas, M. Influence of Pressure in the First Pumping Stage on Analyte Desolvation and Fragmentation in Nano-ESI MS. *Anal. Chem.* **2001**, *73* (24), 6040–6046. https://doi.org/10.1021/ac010451h.

(14) Šamalikova, M.; Matečko, I.; Müller, N.; Grandori, R. Interpreting Conformational Effects in Protein Nano-ESI-MS Spectra. *Anal Bioanal Chem* **2004**, *378* (4), 1112–1123. https://doi.org/10.1007/s00216-003-2339-6.

(15) Van Berkel, G. J.; Zhou, F.; Aronson, J. T. Changes in Bulk Solution PH Caused by the Inherent Controlled-Current Electrolytic Process of an Electrospray Ion Source. *International Journal of Mass Spectrometry and Ion Processes* **1997**, *162* (1), 55–67. https://doi.org/10.1016/S0168-1176(96)04476-X.

(16) Konermann, L.; Silva, E. A.; Sogbein, O. F. Electrochemically Induced PH Changes Resulting in Protein Unfolding in the Ion Source of an Electrospray Mass Spectrometer. *Anal. Chem.* **2001**, *73* (20), 4836–4844. https://doi.org/10.1021/ac010545r.

(17) Zhou, S.; Prebyl, B. S.; Cook, K. D. Profiling PH Changes in the Electrospray Plume. *Anal. Chem.* **2002**, *74* (19), 4885–4888. https://doi.org/10.1021/ac025960d.

(18) Iavarone, A. T.; Williams, E. R. Mechanism of Charging and Supercharging Molecules in Electrospray Ionization. *J Am Chem Soc* **2003**, *125* (8), 2319–2327. https://doi.org/10.1021/ja021202t.

(19) Krusemark, C. J.; Frey, B. L.; Belshaw, P. J.; Smith, L. M. Modifying the Charge State Distribution of Proteins in Electrospray Ionization Mass Spectrometry by Chemical Derivatization. *J. Am. Soc. Mass Spectrom.* **2009**, *20* (9), 1617–1625. https://doi.org/10.1016/j.jasms.2009.04.017.

(20) Verkerk, U. H.; Peschke, M.; Kebarle, P. Effect of Buffer Cations and of H3O+ on the Charge States of Native Proteins. Significance to Determinations of Stability Constants of Protein

Complexes. *Journal of Mass Spectrometry* **2003**, *38* (6), 618–631. https://doi.org/10.1002/jms.475.

(21) Allen, N. R.; Li, H.; Cheung, A.; Xu, G.; Zi, Y.; Li, A. Femtoamp and Picoamp Modes of Electrospray and Paper Spray Ionization. *International Journal of Mass Spectrometry* **2021**, *469*, 116696. https://doi.org/10.1016/j.ijms.2021.116696.

(22) Li, H.; Allen, N.; Li, M.; Li, A. Conducting and Characterizing Femto Flow Electrospray Ionization. *Analyst* **2022**, *147* (6), 1071–1075. https://doi.org/10.1039/D1AN02190G.

(23) Kockmann, T.; Panse, C. The Rawrr R Package: Direct Access to Orbitrap Data and Beyond. *J. Proteome Res.* **2021**, *20* (4), 2028–2034. https://doi.org/10.1021/acs.jproteome.0c00866.

(24) Mortensen, D. N.; Williams, E. R. Investigating Protein Folding and Unfolding in Electrospray Nanodrops Upon Rapid Mixing Using Theta-Glass Emitters. *Anal. Chem.* **2015**, *87* (2), 1281–1287. https://doi.org/10.1021/ac503981c.

(25) Luan, M.; Hou, Z.; Huang, G. Suppression of Protein Structural Perturbations in Native Electrospray Ionization during the Final Evaporation Stages Revealed by Molecular Dynamics Simulations. *J. Phys. Chem. B* **2022**, *126* (1), 144–150. https://doi.org/10.1021/acs.jpcb.1c09130.

(26) Winkler, R. ESIprot: A Universal Tool for Charge State Determination and Molecular Weight Calculation of Proteins from Electrospray Ionization Mass Spectrometry Data. *Rapid Communications in Mass Spectrometry* **2010**, *24* (3), 285–294. https://doi.org/10.1002/rcm.4384.

(27) Dugan, L. D.; Bier, M. E. Mechanospray Ionization MS of Proteins Including in the Folded State and Polymers. *J. Am. Soc. Mass Spectrom.* **2022**, *33* (5), 772–782. https://doi.org/10.1021/jasms.1c00344.

(28) Aliyari, E.; Konermann, L. Atomistic Insights into the Formation of Nonspecific Protein Complexes during Electrospray Ionization. *Anal. Chem.* **2021**, *93* (37), 12748–12757. https://doi.org/10.1021/acs.analchem.1c02836.

(29) Pan, P.; Gunawardena, H. P.; Xia, Y.; McLuckey, S. A. Nanoelectrospray Ionization of Protein Mixtures: Solution PH and Protein PI. *Anal. Chem.* **2004**, *76* (4), 1165–1174. https://doi.org/10.1021/ac035209k.

(30) Peng, Y.; Zhang, S.; Gong, X.; Ma, X.; Yang, C.; Zhang, X. Controlling Charge States of Peptides through Inductive Electrospray Ionization Mass Spectrometry. *Anal. Chem.* **2011**, *83* (23), 8863–8866. https://doi.org/10.1021/ac2024969.

(31) Han, Z.; Chen, L. C. High-Pressure NanoESI of Highly Conductive Volatile and Non-Volatile Buffer Solutions from a Large Taylor Cone: Effect of Spray Current on Charge State Distribution. *International Journal of Mass Spectrometry* **2022**, *476*, 116845. https://doi.org/10.1016/j.ijms.2022.116845.

(32) Yuill, E. M.; Sa, N.; Ray, S. J.; Hieftje, G. M.; Baker, L. A. Electrospray Ionization from Nanopipette Emitters with Tip Diameters of Less than 100 Nm. *Anal. Chem.* **2013**, *85* (18), 8498–8502. https://doi.org/10.1021/ac402214g.

(33) Van Berkel, G. J.; Asano, K. G.; Schnier, P. D. Electrochemical Processes in a Wire-in-a-Capillary Bulk-Loaded, Nano-Electrospray Emitter. *J. Am. Soc. Mass Spectrom.* **2001**, *12* (7), 853–862. https://doi.org/10.1016/S1044-0305(01)00264-1.

(34) Girod, M.; Dagany, X.; Antoine, R.; Dugourd, P. Relation between Charge State Distributions of Peptide Anions and PH Changes in the Electrospray Plume. A Mass Spectrometry and Optical Spectroscopy Investigation. *International Journal of Mass Spectrometry* **2011**, *308* (1), 41–48. https://doi.org/10.1016/j.ijms.2011.07.020.

(35) Feng, L.; Gong, X.; Song, J.; Zhai, R.; Huang, Z.; Jiang, Y.; Fang, X.; Dai, X. Strong Acid Anions Significantly Increasing the Charge State of Proteins during Electrospray Ionization. *Anal. Chem.* **2020**, *92* (2), 1770–1779. https://doi.org/10.1021/acs.analchem.9b03416.

(36) Konermann, L.; Douglas, D. J. Equilibrium Unfolding of Proteins Monitored by Electrospray Ionization Mass Spectrometry: Distinguishing Two-State from Multi-State Transitions. *Rapid Communications in Mass Spectrometry* **1998**, *12* (8), 435–442. https://doi.org/10.1002/(SICI)1097-0231(19980430)12:8<435::AID-RCM181>3.0.CO;2-F.

(37) Šamalikova, M.; Grandori, R. Role of Opposite Charges in Protein Electrospray Ionization Mass Spectrometry. *Journal of Mass Spectrometry* **2003**, *38* (9), 941–947. https://doi.org/10.1002/jms.507.

(38) Grandori, R. Detecting Equilibrium Cytochrome c Folding Intermediates by Electrospray Ionisation Mass Spectrometry: Two Partially Folded Forms Populate the Molten-Globule State. *Protein Science* **2002**, *11* (3), 453–458. https://doi.org/10.1110/ps.45102.

(39) Goto, Y.; Hagihara, Y.; Hamada, D.; Hoshino, M.; Nishii, I. Acid-Induced Unfolding and Refolding Transitions of Cytochrome c: A Three-State Mechanism in Water and Deuterium Oxide. *Biochemistry* **1993**, *32* (44), 11878–11885. https://doi.org/10.1021/bi00095a017.

(40) Li, M.; Li, H.; Allen, N. R.; Wang, T.; Li, L.; Schwartz, J.; Li, A. Nested-Channel for on-Demand Alternation between Electrospray Ionization Regimes. *Chem. Sci.* **2021**, *12* (5), 1907–1914. https://doi.org/10.1039/D0SC06221A.

(41) Tang, Liang.; Kebarle, Paul. Dependence of Ion Intensity in Electrospray Mass Spectrometry on the Concentration of the Analytes in the Electrosprayed Solution. *Anal. Chem.* **1993**, *65* (24), 3654–3668. https://doi.org/10.1021/ac00072a020.

(42) Gomez, A.; Tang, K. Charge and Fission of Droplets in Electrostatic Sprays. *Physics of Fluids* **1994**, *6* (1), 404–414. https://doi.org/10.1063/1.868037.

(43) Smith, J. N.; Flagan, R. C.; Beauchamp, J. L. Droplet Evaporation and Discharge Dynamics in Electrospray Ionization. *J. Phys. Chem. A* **2002**, *106* (42), 9957–9967. https://doi.org/10.1021/jp025723e.

(44) Mortensen, D. N.; Williams, E. R. Ultrafast (1 Ms) Mixing and Fast Protein Folding in Nanodrops Monitored by Mass Spectrometry. *J. Am. Chem. Soc.* **2016**, *138* (10), 3453–3460. https://doi.org/10.1021/jacs.5b13081.

(45) Breuker, K.; McLafferty, F. W. Stepwise Evolution of Protein Native Structure with Electrospray into the Gas Phase, 10−12 to 102 s. *Proceedings of the National Academy of Sciences* **2008**, *105* (47), 18145–18152. https://doi.org/10.1073/pnas.0807005105.

(46) Liu, X.; Inbar, Y.; Dorrestein, P. C.; Wynne, C.; Edwards, N.; Souda, P.; Whitelegge, J. P.; Bafna, V.; Pevzner, P. A. Deconvolution and Database Search of Complex Tandem Mass Spectra of Intact Proteins*. *Molecular & Cellular Proteomics* **2010**, *9* (12), 2772–2782. https://doi.org/10.1074/mcp.M110.002766.

7.6 Supporting information

7.6.1 Possible multiple spraying modes in femtoampere mode

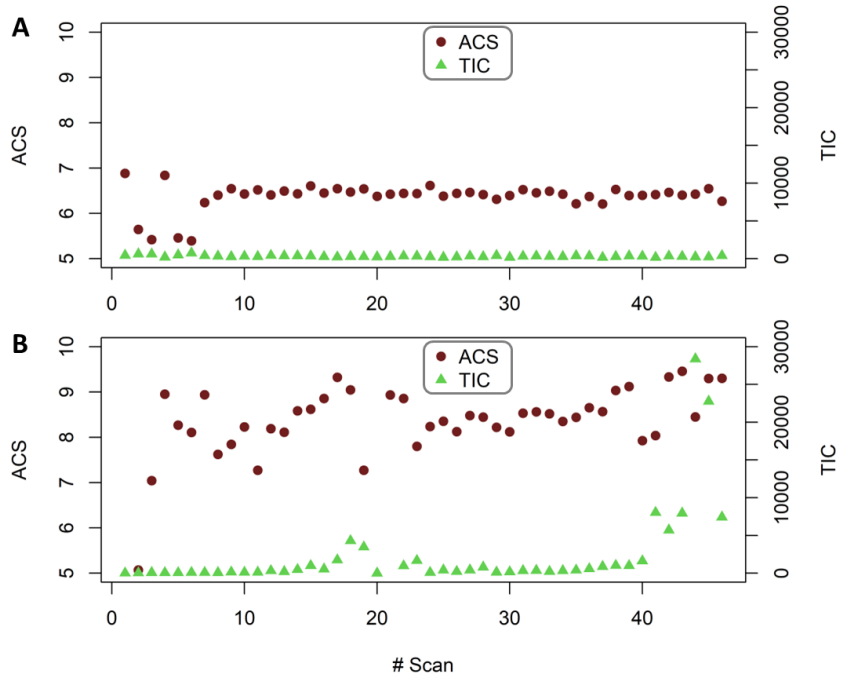

Figure S 7-1. Representative ACS of cytochrome c was monitored along with the TIC at each scan. The detection of TIC at E4 level suggests the possibility of another spray mode, as reported in Allen et al.'s study on femtoampere ionization. To prevent any interference from other spraying modes, the mass spectra of femtoampere mode obtained in this study were filtered using TIC (NL <100).

7.6.2 Effect of the in-source fragmentation energy

The effect of in-source fragmentation energy on the mass spectra of cytochrome c was investigated by recording the mass spectra of the same sample against a variety of source fragmentation energies from 0 V to 100 V. Figure S 7-2 showed that the signal intensities of the dimeric ion decreased gradually and until it was no longer detectable at an in-source fragmentation energy of 100 V.

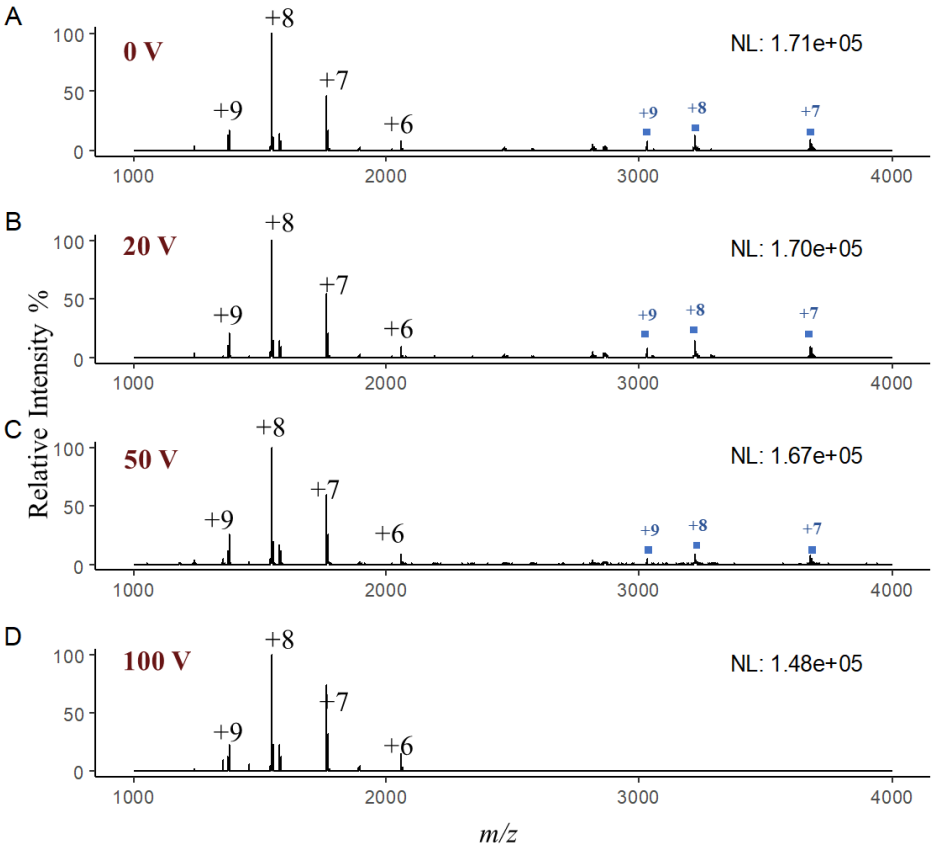

Figure S 7-2. Effect of in-source fragmentation energy on the dimeric species. A) 0 V; B) 20 V, C) 50 V, D) 100 V. The mass spectrum was an average of 8-10 scans. The square represents the dimeric species of cytochrome c. The sample being analyzed was 10 µM cytochrome c in pure water.

7.6.3 Extracting *m/z* values and related intensities for a specified scan using R codes

```
library(rawrr)
mass.spec.scan <- function(raw,scan.vec=1:2)
  mass.spec = rawrr::readSpectrum(raw, scan = scan.vec)
  df <- data.frame("m/z" = mass.spec[[1]]$mZ)
  intensity <- list()
  for (i in 1:length(scan.vec)) {
    intensity$i <-mass.spec[[i]]$intensity
    df <- cbind(df,intensity$i)
    colnames(df)[which(names(df) == "intensity$i")] <- paste0('Intensity.scan',i)
  }
  return(df)
}
```

7.6.4 Calculate the ACS using R codes

```
ACS <- function(raw,scan,MW,charge_min,charge_max,amu){
  Adduct=1
  mass.spec = rawrr::readSpectrum(raw, scan = scan) # install package rawrr
  df <- data.frame("m/z" = mass.spec[[1]]$mZ)
  intensity <- list()
  for (i in 1:length(scan)) {
    intensity$i <-mass.spec[[i]]$intensity
    df <- cbind(df,intensity$i)
    colnames(df)[which(names(df) == "intensity$i")] <- paste0('Intensity.scan',i)
  }
  if (length(scan)>1) {
    df_2 = data.frame(df[,1],rowMeans(df[,-1]))
    mzC = data.frame('charge'=charge_min:charge_max)
    mz <- c()
    in_mz <- c()
    charge_v = charge_min:charge_max
    for (i in 1:length(charge_v)) {
      mz[i]=(MW+Adduct*charge_v[i])/charge_v[i]
      in_mz[i] = max(df_2[df[,1]>(mz[i]-amu)&df[,1]<(mz[i]+amu),2])
    }
    mzC = cbind(mzC,mz,in_mz)
    bool=mzC[,3]>median(df[,2])
    output=sum(mzC[bool,3]*mzC[bool,1])/(sum(mzC[bool,3]))
  } else {
    mzC = data.frame('charge'=charge_min:charge_max)
    mz <- c()
    in_mz <- c()
    charge_v = charge_min:charge_max
    for (i in 1:length(charge_v)) {
      mz[i]=(MW+Adduct*charge_v[i])/charge_v[i]
      in_mz[i] = max(df[df[,1]>(mz[i]-amu)&df[,1]<(mz[i]+amu),2])
    }
    mzC = cbind(mzC,mz,in_mz)
    bool=mzC[,3]>median(df[,2])
    output=sum(mzC[bool,3]*mzC[bool,1])/(sum(mzC[bool,3]))
  }
  return(output)
}
```

7.6.5 Fitting Sigmoid function using R codes

```
library(drc)
pH = c(5,3.2,2.7,2.5,2.1,2.0)
fraction_nano = c(1,0.978,0.974,0.708,0.038,0.029)
fraction_femto = c(1,0.986,0.943,0.697,0.305,0.187)
ph_fraction_curve <- drm(fraction_nano~pH,fct = LL.4())
summary(ph_fraction_curve)
plot(ph_fraction_curve,col='#711D1D',pch=19, xlab = 'pH',ylab = '% folded',ylim = c(0,1))
ph_fraction_curve_2 <- drm(fraction_femto~pH,fct = LL.4())
summary(ph_fraction_curve_2)
plot(ph_fraction_curve_2,col='blue',pch=19, xlab = 'pH',ylab = '% folded',ylim = c(0,1))
```

7.6.6 Fragments of cytochrome c detected in ESI-MS

To elucidate the peak at *m/z* 971 on the mass spectrum of cytochrome c, a high-resolution mass spectrometer LTQ velos Orbitrap (Thermo Scientific, San Jose, CA) was used to acquire the mass spectra of a 10 μM cytochrome c standard sample. The parameters were set as follows: spray voltage 1.5 kV, capillary temp 150 °C, and S-lens RF 70%. In the mass spectra of 10 μM cytochrome c in pure water, **Figure S 7-3**, several peaks, such as *m/z* 971.27 and *m/z* 1052.71 did not match the calculated values for cytochrome c. Further deconvolution analysis performed on MASH Native developed by Ge Ying group [46] revealed that the ions at *m/z* 971 had a molecular weight of 2909.8 Da. Other unknown ions at *m/z* 1052.7, *m/z* 1183.55 and *m/z* 1352.47 were attributed to an unknown species with a molecular weight of 9460.3 Da. Notably, the sum of the two unknown species (2909.8 Da + 9460.3 Da = 12370.1 Da) was just 18 Da larger than the molecular weight (12352 Da) of cytochrome C. This coincidence strongly implied that the two unknown species might come from a hydrolysis of cytochrome c. Based on the assumption that every amide bond in cytochrome c can undergo hydrolysis, we calculated the corresponding molecular masses of the resulting peptides using the R package "peptides". We found that out of all possible peptides, only one with a molar mass of 2909 Da was identified, which corresponds to the proposed peptide 'MIFAGIKKKTEREDLIAYLKKATNE' with cleavage site Met80. This

peptide does not bind to the heme group, which makes it a plausible explanation for the unknown species observed in this study (**Figure S7-4**). As a result, this peptide was labeled as a fragment in our analysis.

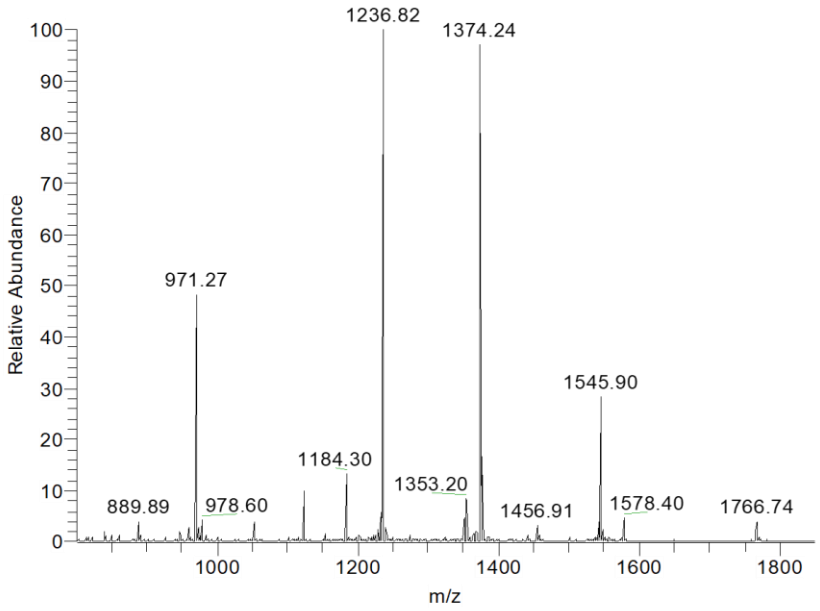

Figure S 7-3. Mass spectrum of 10 µM cytochrome c in water. The mass spectrum was an average of 20 scans

1-10 GDVEKGKKIF 11-20 VQKCAQCHTV 21-30 EKGGKHKTGP

31-40 NLHGLFGRKT 41-50 GQAPGFTYTD 51-60 ANKNKGITWK

61-70 EETLMEYLEN 71-80 PKKYIPGTKM 81-90 IFAGIKKKTE

91-100 REDLIAYLKK 101-104 ATNE

Figure S 7-4. The amino acid sequence of cytochrome c from equine heart (Sigma Aldrich). The red motif (CAQCH) is responsible for binding the heme group via covalent thioether bonds to two cysteine side chains. The blue highlighted amino acid sequence was proposed to correspond to the fragment at *m/z* 971.27.

7.6.7 The dimeric species in the ESI-MS analysis

Table S 7-1. The molar mass of dimeric species calculated using ESIprot tool developed by Robert Winkler. [26]

Protein	1st *m/z*	2nd m/z 2	MW of dimer	MW of monomer
Lysozyme	2980.6	3311.5	29795±0.7	14307
Cytochrome c	3218.7	3678.6	25742±0.8	12362
Ubiquitin	2550.3	2974.2	17842±3	8568

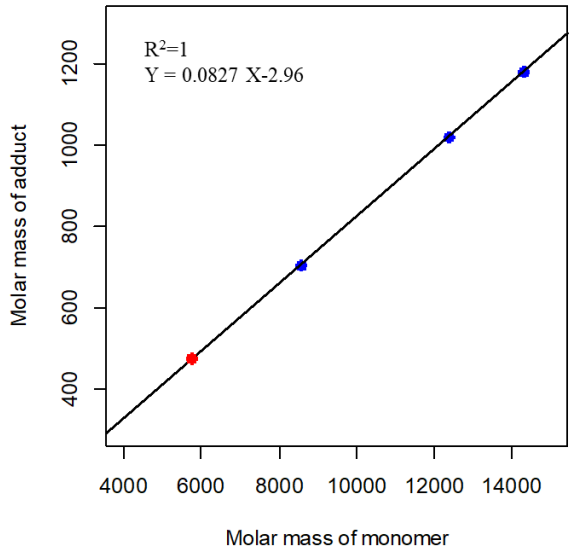

Figure S 7-5. A linear fitting curve was used to model the relationship between the molar mass of the protein monomer and the mass of the adduct, which was obtained by subtracting twice the monomer mass from the calculated mass. The red circle on the plot represented the data point from another research group.